Graduate Theses and Dissertations   Graduate School

September 2014

RTEMIS: Real-Time Tumoroid and Environment Monitoring Using Impedance Spectroscopy and pH Sensing

Frank Alexander
University of South Florida, faalexan@mail.usf.edu

Follow this and additional works at: http://scholarcommons.usf.edu/etd

Part of the Engineering Commons

RTEMIS: Real-time Tumoroid and Environment Monitoring Using Impedance

Spectroscopy and pH Sensing

by

Frank A. Alexander Jr.

A dissertation submitted in partial fulfillment
of the requirements for the degree of
Doctor of Philosophy
Department of Electrical Engineering
College of Engineering
University of South Florida

Co-Major Professor: Shekhar Bhansali, Ph.D.
Co-Major Professor: Andrew Hoff, Ph.D.
Nathan Gallant, Ph.D.
Meera Nanjundan, Ph.D.
Alberto Sagues, Ph.D.

Date of Approval:
June 9, 2014

Keywords: tumor spheroids, microelectrode, cancer cells, microfluidics, lab-on-a-chip

Dedication

This work is dedicated to my mother and father, Frank and Gladys Alexander and my sisters Kimberly and Jalexia Alexander. Thank you for your love and support over the past five years. I'd also like to dedicate this dissertation to the memory of my late grandmother Climmie Rodell Young, who helped to show me the meaning of perserverance.

Acknowledgments

I would like to start by giving thanks to my Lord and savior Jesus Christ who has guided me throughout this journey to the PhD. He has truly opened doors for me and helped me to travel to places far beyond my imagination. Thank you to my mother and father, who instilled in me early on that learning is a lifetime endeavor, and gave me the foundation necessary to give me a head start to success. A special thank you goes to the Timbuktu Academy and my LS-LAMP mentor Dr. Diola Bagayoko, who taught me the effectiveness of the Power Law of Human Performance and the dedication it takes to make an expert of one self.

In addition, I would like to thank the entire staff at the Nanotechnology Research and Education Center (NREC) for their patience and kindness over the years and help with repairing tools and determining process parameters. I am extremely thankful for Mr. Leigh West for all of his help with developing cell culture protocols and teaching proper cell culturing technique at the Florida Center of Excellence for Drug Discovery and Innovation (CDDI). I would also like to thank the National Science Foundation Graduate Research Fellowship Program (GRFP) and the Mcknight Foundation for funding my PhD and travel, allowing me to focus solely on producing stellar research.

Next, I would like to my friends and family for their support, without which I may have given up prior to making it to the end of the journey. Thank you to Ms. Yeoman's and Ms. Frances for their support and Sunday dinners that helped sustain me when I felt like running home. In conclusion, I would like to thank my advisors Dr. Shekhar

Bhansali and Dr. Andrew Hoff for mentoring me and helping to pull me through the process. Also, I'd like to say a very special thank you to Mr. Bernard Batson and the entire Bridge to the Doctorate family for their encouragement, friendship and companionship. Finally, to my friends, mentors, and fellow alum from Southern University (Dr. Brandon Richard, Dr. Justin Boone and Dr. Eric Huey), WE MADE IT!

Table of Contents

List of Tables

List of Figures

Abstract

This research utilizes Electrical Impedance Spectroscopy, a technique classically used for electrochemical analysis and material characterization, as the basis for a non-destructive, label-free assay platform for three dimensional (3D) cellular spheroids. In this work, a linear array of microelectrodes is optimized to rapidly respond to changes located within a 3D multicellular model. In addition, this technique is coupled with an on chip micro-pH sensor for monitoring the environment around the cells. Finally, the responses of both impedance and pH are correlated with physical changes within the cellular model. The impedance analysis system realized through this work provides a foundation for the development of high-throughput drug screening systems that utilize multiple parallel sensing modalities including pH and impedance sensing in order to quickly assess the efficacy of specific drug candidates.

The slow development of new drugs is mainly attributed to poor predictability of current chemosensitivity and resistivity assays, as well as genetic differences between the animal models used for tests and humans. In addition, monolayer cultures used in early experimentation are fundamentally different from the complex structure of organs *in vivo*. This requires the study of smaller 3D models (spheroids) that more efficiently replicate the conditions within the body.

The main objective of this research was to develop a microfluidic system on a chip that is capable of deducing viability and morphology of 3D tumor spheroids by monitoring both the impedance of the cellular model and the pH of their local

environment. This would provide a fast and reliable method for screening pharmaceutical compounds in a high-throughput system.

Chapter 1: Introduction

The focus of this research is to optimize impedance-based techniques and couple them with parallel micro-pH sensors to monitor morphological and environmental changes within a 3-dimensional tumor cell model using multiple electrode sensors. Impedance-based techniques not only supply real-time, label-free measurements, but can also give insight into pathological processes occurring within cell cultures. This work presents a method that optimizes a microelectrode design primarily used for planar cellular cultures for measuring impedance of 3D tumor models at several spatial locations. In addition, a feasibility study is performed for the fabrication of an on-chip micro-pH sensor to measure extracellular pH simultaneously. The outcome of this work is a design for a biosensor capable of correlating morphological changes with environmental pH changes in physiologically significant drug models; thus creating a system on a chip scalable for high-throughput drug screening.

1.1   Motivation

Screening candidate drugs for potential cancer therapeutics is a long and arduous process. After initial discovery of a potential compound, its development into a drug begin with in vitro testing often done on 2D culture models. While adequate for initial tests of drug compatibility/cytotoxicity, these models fail to be effective predictors of clinical success. This shortcoming is due to a lack of cell-cell and cell-matrix contacts in 2D culture that are essential for cellular development and proper gene expression. This results in fundamental behavioral differences between traditional monolayer (2D)

cell cultures and the in vivo tumor. Furthermore, chemical markers often used in 2D testing interfere with cellular metabolic pathways, altering and even impairing the natural functions of proteins. As a result, three dimensional tissue models and label free tests are quickly gaining ground as an intermediate and alternative step for cancer therapy screening. Despite their drawbacks, measurement of the response of various human cellular/tumor monolayer cultures exposed to new drug therapies remains a chief benchmark for determining drug efficacy and safety.

As a result of this, the development of new therapeutics is delayed due to current assays for chemosensitiviy being unsuccessful for predicting clinical effectiveness. Additionally, it has become apparent that newer drug models should encompass both the tumor and its surrounding environment [1]. Although mouse and other small animal models are used currently to aid in development, they do a poor job predicting the clinical efficiency because of species-level differences. For this reason standard adherent cell models display a vastly simplistic array of phenotypic morphologies and fail to maintain clinically relevant attributes including resistance to uptake.

1.2   Problem Definition

Primarily organ tissue is comprised of individual cells positioned in precise 3D patterns in close proximity. This defined structure provides an ease of communication with surrounding matrix proteins allowing reproduction of organ-level behavior in model systems outside the body. Researchers have found cellular models containing 3D spherical models have properties that drastically mirror performance in vivo [2, 3]. Nevertheless, major issues must be resolved to reliably use 3D models for diagnosis or drug development. In contrast with macroscale laboratory approaches, microfluidic

devices offer the potential for more controlled formation of 3D cell cultures and are also particularly suitable for high-throughput screening on small sample sizes, such as biopsies [1].

Three dimensional tissue models provide a means to more accurately study cell-cell and cell-matrix interactions and more importantly the effect of pharmaceutical agents on these interactions [4]. Techniques optimized for monolayer and suspension cultures are now being converted and optimized for 3D spheroid cultures. One label-free technique currently being translated for 3-dimensional culture analysis is Electrical Impedance Spectroscopy (EIS). EIS applies a constant AC current through a range of frequencies to a sample and measures the resulting current and then calculates the impedance of the sample. In the past, EIS has been utilized for assays of monolayer cultures including cytotoxicity, cell proliferation, and cellular kinetics/movement assays. Spheroid EIS systems have been used to monitor responses to chemotherapeutics [5], differentiation of osteogenic cells [6] and Alzheimer's disease-like neurodegeneration of neuroblastoma spheroids [7]. An inherent flaw in these systems is a lack of spatial resolution, inhibiting location specific analysis as well as investigation of drug penetration and diffusion. Furthermore, the mechanisms leading to cell death and morphology changes are difficult to discover based on impedance measurements alone. For this reason, this work seeks to develop electrodes capable of probing multiple areas of a single spheroid to increase spatial resolution and implement environmental pH sensors to assign physiological significance to the measured impedances.

1.3   Research Objectives

The objective of this research is to develop a multi-parameter system on a chip that is capable of deducing viability and morphology of 3D tumor spheroids by enabling monitoring of impedance and environmental pH. Specific objectives include:

1) Optimize impedance measurements of 3D tumor spheroids using planar electrode array design

2) Design and integrate an on chip micro-pH electrode for simultaneous environmental monitoring

3) Correlate impedance and pH data with biological events

1.4   Dissertation Structure

Chapter 2 of the dissertation introduces the justification for replacing common planar culture methods with 3D cellular models, the importance of label-free assay systems, currently available label-free assays, and the fundamentals of electrochemical impedance spectroscopy (EIS).

Chapter 3 reviews the state of the art of impedance-based assay systems used for monitoring cellular cultures. Commercial assays for 2D cellular models are reviewed in depth and developing assay systems for 3D cellular models are introduced.

In Chapter 4, the design, fabrication and testing of improved multi-spatial microelectrode array designs for impedance measurements of monolayer cellular cultures are discussed. An automated impedance monitoring system was developed to measure impedance of cellular monolayers in real-time. Experimental results are presented which illustrate the benefits of higher spatial resolution for bioimpedance spectroscopy

Chapter 5 describes the design and optimization of multi-spatial microelectrodes in a microfluidic channel for tumor spheroid impedance monitoring in real-time. Tumor cells of both planar and spheroidal morphologies are described. For spheroidal cultures, comparisons are made between simulation results and measured data.

Chapter 6 introduces a feasibility study between two candidate thin films for the addition of an on-chip microfluidic pH sensor. This micro-pH electrode is then incorporated into the bioimpedance chip and tested for stability.

Chapter 2: Background

New pharmaceutical compounds enabling new drugs and treatments for various diseases have been the corner stone for advances in human health over the past century. Unfortunately, the majority of drug candidates fail at various stages of the drug discovery process with only 1 in 10,000 making it to the market [8]. Today, cellular culture provides the first platform for evaluating the efficacy of new compounds as a treatment for a disease. Prior to clinical trials, testing begins with in vitro tests of monolayer cell cultures for preclinical testing including basic absorption, distribution, metabolism, excretion and toxicology (ADME/Tox) testing [9]. These are then followed by animal models, where the specific ailment has to be introduced or surgically implanted prior to testing.

Due to physiological differences between species and the existence of species specific pathogens, these models often fail to be effective predictors of clinical success [10]. To address these issues, drug companies perform numerous studies in parallel to maximize predictive capability. As monolayer cultures alone are inadequate for proving the efficacy of a new drug due to a lack of cell-cell and cell-matrix interactions, there are fundamental behavioral differences between traditional monolayer (2D) cultures and *in vivo* responses [1]. Thus compounds that look promising here are used in animal models, where the impact of cell-cell and cell-matrix interactions can be studied. This approach is both expensive and ethically questionable. This lack of ability of monolayer cultures to quantitatively include the effect of cell-cell and cell-matrix interactions is

made more apparent when phenotypes of monolayer cultures are compared to findings using 3D multicellular spheroids (MCS) [11].

In addition to the shortcomings of in vitro testing, the use of chemical labels in 2D and 3D assays creates significant potential of interference with cellular metabolic pathways; potentially altering and even impairing the natural functions of proteins [12]. This has led to the development of multiple label-free assays as an alternative for screening potential drug therapies. One such promising, label-free assay is Electrical Impedance Spectroscopy (EIS). This noninvasive technique has been utilized for analyzing single cells, cellular suspensions and cellular monolayers. With the increased attention on 3D tissue models for drug studies, it is quickly being expanded for assays on 3D cellular models, specifically MCS. This review will examine past EIS analysis of single cells and 2D cultures; highlight recently developed EIS systems for analyzing 3D cell cultures, including MCS; and discuss future applications of 3D culture impedance monitoring systems.

2.1   2D vs. 3D Tissue Models

2.1.1 Rationale for Using 3D Cellular Cultures

Monolayer cultures have been used for decades to analyze the function of cells and organisms. Unfortunately, this culturing technique fails to preserve the tissue-specific function and morphology of the cells or to culture cells specifically so that they phenotypically represent their in vivo counterparts [7]." While monolayer cultures may proliferate well, de-differentiation occurs and cells become increasingly different from the organs they were originally extracted from [8]. For example, primary hepatocytes lose liver-specific functions and de-differentiate within the first few passages [9, 10].

This is a widespread theme within most monolayer cultures. In 3D spheroid cultures, heterogeneity is expressed through increased cell differentiation and self organization as compared to mostly homogeneous monolayer cultures. Sutherland et al. found that human colon adenocarcinoma spheroids produced gland-like organizations similar to in vivo tumors [11].

In addition to a lack of heterogeneity, it is also apparent that monolayer cultures lack the three dimensional structure of tissue *in vivo*. Because of this lack of 3D organization, cells within monolayer cultures are exposed to equal amounts of oxygen and other nutrients, ignoring gradients formed *in* the body. Gradients are naturally formed in 3D tissues because of the orientation of cells and differences of exposure between cells residing in the exterior and the interior of the cell mass. Oxygen diffuses equally throughout two dimensional cultures; however, it is limited in certain regions of 3D cultures causing hypoxia or low oxygen supply. Hypoxia, a common trait in solid tumors, can cause a decrease in new blood vessel formation in normal tissue. Tumor resistance to different radio and chemotherapy's has been associated with tumor resistance to hypoxia [12]. This resistance is regulated by HIF-1 (hypoxia-inducible factor), which amplifies genes for metabolism and blood vessel formation in tumor cells improving cell survival. HIF-1 inhibition has been explored as an avenue of treatment, but it has been shown that greater concentrations of HIF-1 inhibitory drugs are required in traditional planar cell cultures [13]. By not reproducing this key environmental parameter, drug uptake and diffusion kinetics are distorted, altering the optimal dosage and further complicating the procedure to determine the optimum dosage. Furthermore, significant reductions in cell to cell adhesion and communication also inhibit the

8

secretion of many extracellular matrix proteins, producing fundamental biochemical differences between the in vitro and in vivo micromilieu.

2.1.2 Importance of Label-Free Testing

Traditional assays done on both 2D and 3D cellular cultures involve attaching a label, typically a fluorophore, to biomolecules to visually inspect and identify mechanisms at work. Labels are either detected using visible light microscopy or fluorescent microscopy, a technique in which the attached label is excited via a specific wavelength. The attached fluorophore then emits light at a higher wavelength/quenching emission which is filtered through a lens so it can be seen by the investigator. The emission/quenching intensity of the fluorophore provides a quantitative measure of the mechanism hypothesized. Limitations with this technique begin with the attachment of the fluorophore to different molecules on the cell [13]. Attaching a fluorescent molecule onto specific proteins can affect the natural shape and movement of these biological structures within the organism. This in turn interferes with the biological processes of the cultured cells, resulting in false positives or even sample toxicity [14].

Protein function is a prime example of interference in cellular metabolic pathways resulting from chemical markers often used in 2D and 3D testing [12]. Because protein function is highly related to the conformation of the protein any small change to the shape of the molecule can alter its function [12]. Although advances have been made to minimize the size of organic dyes, they are still subject to steric disturbances when too much dye is present, which will impair natural function.

In addition to changes in normal protein function, the use of labels is time-consuming and involves choosing an appropriate molecule that minimally impacts the cells and their microenvironment [13]. Users must calculate an adequate amount of label to use in order to prevent adverse effects. Furthermore, fluorescent tags do not allow for real-time analysis. Optical measurements must be made using spectral equipment for quantitative measurements of the fluorescent light being emitted or viewed under a fluorescent microscope, both expensive pieces of equipment. Fluorescent labeling is therefore implemented as an endpoint assay, not feasible for extended drug studies. In order for testing to truly mimic the *in vivo* situation, non essential molecules such as fluorescent dyes and proteins should be withheld from the microenvironment. Label-free methods have the potential to prevent conformational changes to proteins and preserve the natural function of protein interaction within the cellular model.

2.1.3 Current Label-Free Techniques and EIS

As explained above, to mimic the *in vivo* environment, attention has been placed on developing an assortment of new and sophisticated label-free techniques for cellular analysis. Many label-free techniques focus on detection of proteins and small molecules through the use of small reporter molecules attached to a transduction element. For example in quartz crystal microbalance (QCM), an acoustic technique, these reporter molecules are attached to a quartz crystal which resonates at a given frequency. The resonating frequency changes as molecules or proteins of interest bind to receptors on the quartz crystal [15].

Other small molecule detection techniques have used different transduction elements such as cantilevers [14, 16, 17] to monitor changes in a particular molecule's concentration or electrical techniques to monitor concentrations of target molecules such as field effect transistors (FETs) [18] and impedance [19]. Nanowires [19] and magnetic microbeads [20] have also been investigated for increasing sensitivity and potentially multiplexing the number of target molecules detected, increasing the knowledge of the mechanisms at play in an experiment. While small molecule detection can provide insight into specific mechanisms of physiological effects of different compounds, these techniques, optimized for traditional monolayer cultures, do little to highlight real-time changes in cellular morphology, mobility, and communication in 3D tissue models.

Another class of label-free biosensors have been developed that focuses on morphological changes from a cellular system-based approach [21]. It has been known that changes to the cellular microenvironment can cause changes in cellular structure, behavior and viability [22]. Therefore, sensors that monitor changes to cellular morphology can be used to assess cellular responses to stimuli. For example, QCM has been used for quantifying morphological changes in cellular mass when exposed to a potential toxicant [23]. Xi et al. reviewed currently available label-free whole cell detection [24].

For this reason label-free whole cell detection mechanisms are currently being developed for studies of 3D cellular models. As the effect of pharmaceutical agents on the cell-cell, cell-matrix interactions are significantly closer to tumor/organ response in 3D tissue models; they provide a means to study cell-cell and cell-matrix interactions

more accurately. One technique currently being developed as a label-free technique for 3-dimensional culture analysis is electrical impedance spectroscopy (EIS).

Easily automated and simple to implement, EIS has been used for a variety of applications to date including: monitoring corrosion [25] and characterizing chemical sensors [26]. It has also been used to inspect cellular membranes [27]. More recently, it is increasingly being utilized for biological applications in order to characterize biological tissue and monitor changes induced by therapeutics as well as toxins. With the development of commercial equipment such as impedance analyzers and their ease of automation, EIS has been recognized as a powerful tool with clinical potential as a real-time diagnostic technique.

2.2 Introduction to EIS

Electrical impedance spectroscopy, known synonymously as Electrochemical Impedance Spectroscopy, has a long history of usage for determining the mechanisms of reactions taking place at electrode/electrolyte interfaces [28]. These studies have culminated in groundbreaking discoveries including: description of the capacitive double layer [29]; actively monitoring corrosion mechanisms [30]; characterization of conductive polymers [31]; the development of DNA, enzyme, and antibody-based label-free biosensors [32]; as well as monitoring cellular morphology [5, 33, 34].

Since Oliver Heaviside's initial definition of the operational impedance [29], many variations to classic impedance measuring techniques have been explored. Chang et al. reviewed improvements in impedance based monitoring, encompassing the past 25 years that have increased measurement speed by using Fourier transforms to measure

multiple frequencies simultaneously. However, the majority of commercially available impedance analyzers utilize single voltage sweeps of multiple frequencies [35].

The electrical impedance of a material is defined as the opposition to the flow of alternating current (AC). The standard EIS method applies a small AC voltage,

$$v(t) = V_0 \sin \omega t,$$

to the material under test, for a wide span of frequencies, where V_0 and ω represent the voltage amplitude and the angular frequency, respectively. The resulting current,

$$i(t) = I_0 \sin \omega t + \theta,$$

where I_0 is the current amplitude, is then measured. In order to remain in the linear response region, a small voltage, typically under 25mV is used. Electrical impedance is defined as the complex ratio between the voltage and current.

$$Z(\omega) = \frac{v(t)}{i(t)}$$

Thus, the magnitude,

$$|Z(\omega)| = \frac{V_0}{I_0}, \text{ and phase, } \theta = tan^{-1}\left(\frac{v(t)}{i(t)}\right),$$

can be calculated. In order to evaluate a system using EIS, one must use a modeling method to explain the behavior of the system. This is approached in one of two ways: using an empirical formula that explicitly describes the system or, more commonly, using an equivalent circuit model which ascribes passive circuit elements to different components of the system.

As real systems rarely exhibit ideal (frequency independent) capacitances, ideal capacitive elements within equivalent circuit models are replaced by constant phase elements (CPE). The formula for a constant phase element is

$$Z_{cpe} = \frac{1}{Y^0 j\omega^\alpha} ,$$

where α is a factor between 0 and 1 and Y^0 is the CPE value, which is equal to the ideal capacitance (C) when α equals 1.

2.2.1   Bioimpedance Measurements

When these experimental procedures are applied to biological systems including whole cells and cellular models, it is termed electrical bioimpedance. Microelectrodes have been developed for analysis of single cells and cellular cultures. In these cellular assays, a low signal voltage is applied to the microelectrodes. The low signal voltage, in addition to preserving linearity, also ensures that the electric field intensity remains small. This is critical for maintaining the viability of cells within the culture and minimizing the impact on the culture medium, making bioimpedance analysis a nondestructive technique for cellular analysis. A classic bioimpedance experiment consists of monitoring the adherence of cells in culture medium with planar microelectrodes (Figure 2-1a). Cells adhere to both the surface of the substrate and the electrodes blocking current exchange through the culture medium. R_{cell} and CPE_{cell} represent the cumulative resistive and capacitive impedances of the monolayer while R_S and CPE_{dl} are the resistance of the solution and the the interfacial (double layer) capacitance caused by the ionic layers formed at the electrode-electrolyte interface. EIS and bioimpedance measurements are typically visualized using Bode plots (Figure 2-1b). The Bode plot depicts the frequency response of the magnitude and phase of the impedance, giving insight into the frequency-dependent mechanisms occurring within the system.

14

When exposed to certain stimulants (environmental or chemical) biomaterials can physiologically respond in various ways such as: morphological changes, increased or decreased adhesion, as well as increased or decreased metabolic output. These physiological changes within the material yield changes to the impedance that vary with frequency. Monitoring these impedance changes over a wide range of different frequencies can provide insight to the viability of the cells. Thus, impedance monitoring can be implemented as a simple and label-free method to observe the status of a cellular culture/model. To date, impedance techniques have regularly been applied to single cells [27, 36-45], cellular monolayers [5, 6, 33, 34, 46-57], and more recently multicellular spheroids (MCS) [1, 4, 6, 58-61].
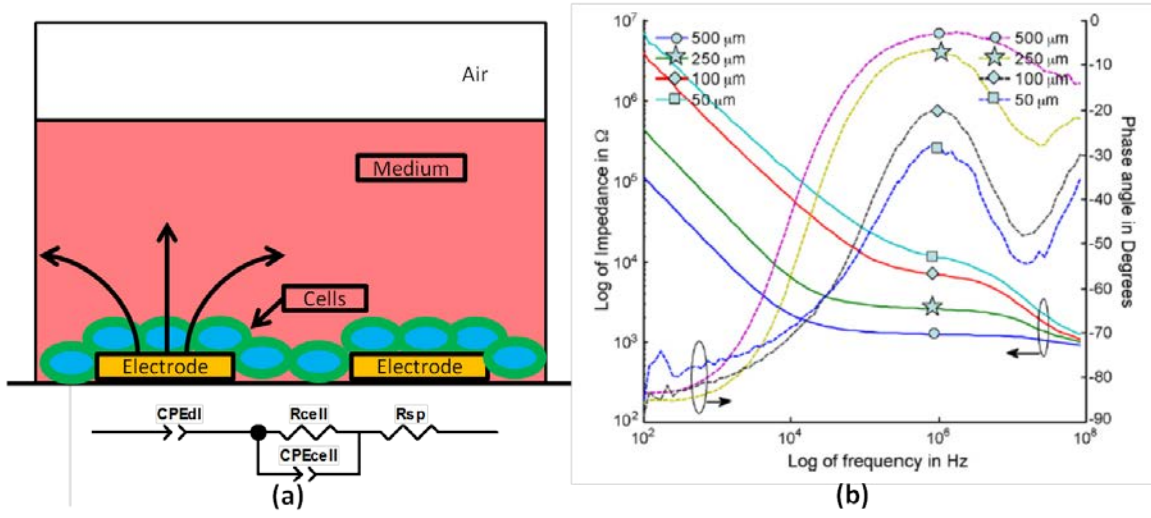
Figure 2-1 (a) An equivalent circuit model for parameter extraction and (b) experimental data (bode plots) for modeling HUVEC monolayers [135].

Chapter 3: Bioimpedance State of the Art

3.1   Impedance-based 2-D Culture Devices

The morphology of a cell *in vitro* is highly dependent on the cell line as well as culture conditions. Different types of cell cultures require specialized culturing methods making various approaches to impedance monitoring necessary. So-called anchorage dependent cells, such as fibroblasts, require a hard surface to adhere to in order to survive and proliferate. Nonadherent cell lines do not require a rigid surface and can be cultured in suspension. Cells cultured in suspension have the advantage that they remain viable independently and do not require trypsinization to separate cells, enabling monitoring of individual cells. This advantage makes cell suspensions well-suited for impedance measurements of individual cells.

3.1.1 Single Cell Culture Monitoring

Separating heterogeneous cell suspensions, such as blood, into single cell constituents has played a major role in point of care diagnostics as well as the study of disease pathology by enabling the detection of abnormal cells such as circulating tumor cells [62]. Devices utilizing impedance cytometry [63] have been used successfully to distinguish between white blood cell types including T-lymphocytes, monocytes and neutrophils within prepared whole blood samples. Cells were distinguished according to cell size via a low frequency (503 kHz) impedance measurement.   Membrane characteristics were extracted via a theoretical opacity measurement defined as the magnitude of impedance measured at a high frequency (1.707 MHz) divided by the

magnitude of impedance at 503 kHz. A lack of sampling resolution hampers its ability to discriminate cell types, requiring a saponin treatment prior to evaluation to destroy red blood cells in the sample so that white blood cells can be counted and differentiated.

Measuring a broader spectrum of frequencies through full impedance spectroscopy, could alleviate the need for pretreatment of the blood[64]. However, commercial impedance analyzers (Agilent 4294A) require a minimum of 5ms to perform a measurement at a single frequency while the cells in the above system move at 60mm/sec, clearing the electrodes in 1ms. Broadspectrum impedance analysis within impedance cytometry devices have been explored using a maximum length sequence approach (MLS) and have produced systems capable of simultaneous measurements of 512 frequencies per millisecond [65]. Despite this advantage over discreet frequency impedance measurements, MLS suffers from its assumption of a static electric field for measurements. In addition, within impedance cytometry experiments, the material under test undergoes particle flow, leading to a loss in signal to noise ratio (SNR). Digital signal processing techniques are being investigated to increase SNR [66].

In addition to cell sorting applications, impedance-based measurements have been utilized for a variety of fundamental cellular studies. Han's micro-EIS system utilized impedance measurements to measure ionic channel activity in single cells and differentiated cells in various stages of cancer [27, 40]. In early stages of some cancers, circulating tumor cells (CTCs), are shed into the bloodstream. Capturing and measuring the number of CTCs and their morphology can potentially be used as a predictor for patient prognosis. Han's micro-EIS system traps single cells precisely between measurement electrodes for characterizing single cells.   Impedance

measurements are made over a spectrum of 100 Hz to 3 MHz and, normal human breast tissue cell line MCF-10A, early-stage breast cancer cell line MCF-7, invasive human breast cancer cell line MDA-MB-231, and metastasized human breast cancer cell line MDA-MB-435 were compared to show dielectric differences between early and late stages of cancer. Averages of 7 to 10 tested cells showed a decrease in impedance magnitude for each cell line, thus distinguishing the different cell lines.

These results show that EIS can be used to distinguish cancer cell lines from a normal cell line and also distinguish cancer cell lines from different pathologic states [27]. Cellular viability stains are not able to provide data in real-time, thus EIS has been used to monitor the response of single cell viability and membrane integrity to chemical exposure. Huang et al. used microaperture devices mounted on a transparent substrate to perform electrochemical viability assays on DU-145 cells and simultaneously monitor them with traditional techniques [41]. Dead cells that had taken up YOYO-1 dye showed chip resistances significantly lower than viable cells with intact membranes [41]. This system was capable of measuring real-time responses of live cells to Triton-X100, a known membrane permeabilizer. An improved microhole chip was developed by Kurz et al in order to monitor nonlethal membrane variations in response to implantation with polymer-DNA complexes [36]. These tests showed that changes in the cellular membrane could be effectively monitored in real-time with high resolution. However, although these systems allow more information to be probed about a single cell, it cannot provide important information about the environment around the cell making it inadequate for tissue culturing monitoring, drug screening, and cytotoxicity testing.

3.1.2 Traditional Monolayer Cultures

Monolayer cultures are composed of anchorage dependent cells grown to form a monolayer at the bottom of a culture dish made of a hard, inert substrate such as glass or polystyrene. Because many cell types must be attached to a surface before they can grow and divide, the cells are attached to a protein layer that has adsorbed to the surface of the electrode from the culture medium. Once the cells have attached, they begin to spread from their initial spherical shapes and flatten against the surface and eventually grow and divide, if conditions are favorable. In normal tissue culture, when the cells reach confluence, (surface becomes filled), cells are then harvested using an enzyme or chelating agent, but in order to monitor cells via EIS, cells remain attached to the surface electrodes.

Researchers have exploited this need for cellular adhesion to make impedance measurements of entire cell populations cultured over electrodes. By fabricating microelectrodes on hard and often transparent substrates, impedance has been used to monitor a multitude of cellular parameters including cellular kinetics [33, 48, 53], drug screening [25], cellular adhesion [26], and cellular differentiation [5, 27, 28]. Perhaps one of the most well-know techniques used to monitor these changes is the Electric Cell-Substrate Impedance Sensing (ECIS) system. Within the ECIS system, cells monolayers are grown directly on gold microelectrodes immersed in tissue culture medium. The capacitive cellular membrane constricts the current paths at lower frequencies forcing current through the tight junctions between the cells and between the cell-substratum gaps.

This technique can be optimized to yield specific data about cellular behavior and may have the potential to be adapted to identify specific cell lines [27]. As a result of the increased interest in EIS-based monitoring, other ECIS-based systems have been used to perform more specific studies. xCELLigence, another commercial impedance monitoring system, demonstrated the capability to monitor the effects of antibodies on voltage gated calcium channels in rat insulinoma cells. Anti-VGCC antibodies isolated from diabetic patients were shown to have a negative impact on adherence of Rin A12 cells, reaffirming whole organ assays that suggest that antibodies that function against VGCC may contribute to neurodegeneration [67]. A major challenge of ECIS-based cellular monitoring is a lack of spatial resolution and the collection of statistically-significant data from single culture wells. A solution to this problem is via incorporation of independent electrodes within a cell culture to enhance the spatial resolution and statistical analyses of impedance measurements.

Few designs have implemented multiple independent electrode measurements within a cell culture. Wegener et al. [68], for example, designed a device with a row of 4 independent working (sensing) electrodes (2 mm-diameter) to conduct trans-epithelial and trans-endothelial electrical resistance (TER) measurements of cell cultures. Their multi-electrode design allows one to measure local inhomogeneities within the cell culture [68]. Similarly, Arndt et al. [46], developed a device with 3-independent electrodes (4 mm-diameter) on a microscope slide. In both studies, quantitative analyses and comparisons of the individual electrodes were not demonstrated. Additionally, the large working electrodes result in a greater averaging effect than if microelectrodes were used. A variety of electrode designs are offered through the

commercial ECIS system vendors, including single electrode devices, interdigitated electrodes (IDEs), and a device with 2 independent working electrodes (250 μm) within a cell culture chamber.

Our approach has been to enhance the spatial resolution by increasing the number of independent working electrodes to obtain redundant impedance datasets within the same cell culture chamber. The improved electrode design (Figure 3-1a) has eight independent sensing electrodes to improve statistical significance of measured data and obtain position-dependent data across the cell culture. The system was evaluated by investigating the effects of a cytotoxic agent, arsenic trioxide (As_2O_3), on the well-established ovarian carcinoma cell line.

3.2   Impedance-based 3-D Culture Devices

3.2.1 3D Cellular Models

As traditional planar cultures are often insufficient for more complex studies, including drug interaction and cellular differentiation, 3D cellular models are desirable due to their proximity to the actual phenotype expressed *in vivo*. Cell-cell and cell-extracellular matrix communication are the primary appeal of using 3D cellular models. Many (if not all) of these interactions are lost in 2D monolayer cultures making them less similar to physiology found in cells *in vivo*, which makes them unreliable for predicting effects of drugs [69]. Several types of 3D cellular models have been developed for studying drug effects *in vitro*. Organotypic explants are one example [2], consisting of a small fragment of tissue that is isolated from a subject. By keeping explant slices at a thickness of less than .3mm, they can be preserved outside of the original subject. However, due to their relatively large size tissue explants are difficult to

obtain and maintain. Their large size also does not adequately support mass transport of nutrients to interior cells resulting in a loss of viability of the sample [70].

MCS, known as tumoroids or multicellular tumor spheroids (MCTS) when referring to cancerous cells or embryoid bodies when referring to stem cell agglomerations, are a simple 3D tissue model that is composed exclusively of cells closely aggregated to one another in a semispherical shape [71]. MCTS size is limited to a maximum of 100 μm without oxygen limitation (due to limited oxygen diffusion length), enabling easy diffusion of oxygen and other nutrients throughout the culture [72, 73]. Spheroid diameters greater than 100 μm introduce hypoxia which can affect drug resistance [10]. Other 3D tumor models have been developed to more closely replicate the tumor microenvironment. 3D scaffolds composed of both synthetic and biomaterials have also been used to aid in forming *in vitro* 3D models of cell types. The mulitcellular layer (MCL) model employs a porous Teflon® membrane coated with collagen [74, 75]. Cells are seeded onto the permeable membrane immersed into medium and allowed to form multiple layers of cells. Flux and diffusion analysis of different drugs can then be directly assessed by suspending the culture insert into a permeable holder that is immersed in a larger container of medium. The test agent can then be introduced to the first container and diffuse through the MCL and into the second container.   High performance liquid chromatography (HPLC) can then be used to detect the target agent.

Another scaffold-based model, the hollow fiber model, utilizes unfilled polyvinylidine fluoride threads (450-500μm diameter). The biocompatible fibers are seeded with high concentration cellular suspensions and allowed to incubate in medium. Cells then adhere to the interior of the fiber and can then be used for

chemotherapeutic testing [75]. However, because cells are constrained within the scaffold the proliferation of the cells is limited to the size within the fiber. The fiber also acts as a barricade to the natural diffusion of macromolecules, preventing studies using nanoparticles such as silica nanowires [76-78] or quantum dots [79, 80].

MCS models are advantageous over existing models because of their simple morphology and are increasingly being cultured in high quantities, making them highly amenable for high-throughput drug screening. In addition, most MCTS models form necrotic cores similar to the pathophysiology of avascular tumor nodules when cultured to sizes greater than 500 microns [81]. This is typically caused by limited diffusion of positive and negative regulators causing a lack of oxygen and nutrients as well as an accumulation of waste. For this reason, spheroid models are typically maintained at sizes below 500 μm. Many standard tumor cell lines have been isolated that readily form spheroids. A list of spheroid forming tumor cell lines can be found in [82].

3.2.2 MCS Formation and Morphology Monitoring

MCS form in a process that consists of three stages. First, there is an aggregation period where cells in close proximity bind to each other via extracellular matrix (ECM) fibers. After initial aggregation, there is a delay. During this delay, cadherin expression increases, and cadherin levels increase within the aggregation. Finally, as the cadherin accumulates, the spheroid is compacted due to the strong adhesion of cadherin-cadherin bonding. The amount of ECM fiber and cadherin varies from cell to cell [83, 84]. Within the spheroid, different gradients exist (oxygen, nutrients and waste) that govern the composition of the spheroid. A layer structure is the result, forming a zone of proliferating cells on the surface of spheroids 500 μm and above. The

center is then comprised of decaying and dying cells (necrotic) at the core and viable non proliferating cells in between the two.

To date, multiple methods for culturing cellular spheroids have been described in literature. These techniques include culture using nonadhesive surfaces [82, 85], large rotary flasks and roller bottles [86, 87], hanging drop cultures, micropatterning of adhesion proteins [1], synthetic and biomaterial scaffolds [3, 83, 88, 89], external stimuli [90], and cellular molds [91, 92]. An in-depth review of these techniques can be found in [1, 84] . Unfortunately, specialized equipment and plates required for rotary cultures, cell printing, external stimuli, and scaffolds; slow growth time and tedious protocols within hanging drop cultures; and the non-uniform growth for cultures on nonadhesive surfaces prevent these techniques from being converted for high-throughput assay systems. In contrast, cellular molds are highly amenable to conversion to high-throughput systems due to their simplicity and use of inexpensive, widely-available reagents. Commercial plates have been developed (STEMCELL Technologies) containing adhesion-blocked PDMS microcavities capable of molding a variety of stem cells into embryoid bodies (EBs). In practice, cells are first seeded within suspension onto the pretreated surfaces and then evenly distributed using centrifugation, forcing the cells into the micromolds to form spheroidal cell models.

Spheroids are applicable for a wide range of studies, including use as avascular tumor models and as building blocks for organ reconstruction [84]. To date, several techniques have been investigated for monitoring changes in the morphology of 3D MCS. Table 3-1 summarizes currently available label-free techniques for monitoring spheroidal morphology. Many methods of existing biological assays coupled with phase

contrast microscopy can be easily converted for use in spheroidal cultures [93]; however, the majority of traditional techniques include the use of chemical labels.

Label-free techniques have also been used to monitor spheroids. Spheroid growth has been tracked by calculating the volume with radial measurements taken from images recorded using phase contrast microscopy [94]. Nevertheless, basic optical microscopy techniques are only capable of imaging the outer surfaces of spheroids without the need for freezing and sectioning, making real-time analysis impossible. More recently, new imaging techniques like confocal and light sheet microscopy [95] have enabled three dimensional imaging of tumor spheroids allowing researchers to monitor spheroidal uptake of fluorescent nanoparticles [96]. Despite these advances, scanning microscopy suffers from poor image resolution at higher penetration depth required for larger spheroids (>300m) [95]. Magnetic resonance imaging (MRI) circumvents this issue by using magnetic radiation to image cellular proliferation noninvasively and has been utilized for not only imaging spheroidal morphology [97, 98] but also for monitoring intracellular pH [99]. Unfortunately, MRI utilizes highly expensive equipment and requires special expertise to operate, making it difficult to implement in high throughput systems. Impedance monitoring overcome this limitation by being inexpensive, readily automated.

3.2.3 EIS-based 3-D Culture Monitoring

In the past, techniques such as ECIS and micro-EIS have been employed to measure the bioimpedance of cellular monolayers from pairs of fixed planar electrodes. Planar electrodes are suitable for measuring cellular monolayers because the cells are grown directly over the sensing electrodes isolating them from the culture medium upon

reaching confluence. Sufficient contact between the measured cells and the active electrodes is required to produce a detectable signal. When suspension cultured MCS are being assessed, systems that require cellular attachment to planar electrodes in order to monitor cell-substrate interactions are insufficient. In order to circumvent this problem, researchers have employed an array of techniques including microfluidic channels [42], microcavity traps [62, 63], and multilayered cultures [105, 106].

One technique that has been developed, utilizes an array of planar electrode pairs with increasing widths in order to probe multiple depths within a culture of human keratinocytes. In keratinocytes, after confluence is reached cells begin to accumulate into aggregates that [106] termed "domes" that extend heights of up to 120 µm above the sensor surface. Impedance spectroscopy reveals the "apparent resistivity profile" which allows the user to assess the resistivity of the culture at different depths. This gives the advantage of monitoring the keratinocyte evolution from traditional monolayer into 3D cellular agglomerations with heights of up to 120 µm in real-time.

Other researchers have employed planar microelectrodes fabricated onto microcavities to measure the impedance response of cellular spheroids to different stimuli as an avenue for high-throughput screening. A system was devised employing micro-cavities arrays (MCA) of varying widths (200, 300, and 400 µm) etched into silicon. Metal electrode contacts sputtered on all four sides of the cavities record two independent bipolar electrical measurements using EIS. Alterations in normalized spheroid impedance were monitored at 133 kHz after spheroids were exposed to the drug Camptothecin (CPT) for various time intervals to induce apoptosis. Comparisons between treated and untreated spheroids revealed that normalized impedance

increased according to exposure time in a dose dependent fashion. After assessing caspase-3 activity, slight increases in the impedance were attributed to the small increases in apoptosis occurring in the spheroid. This contrasts previous studies which show decreasing impedance values in response to cell death [65]. This was attributed to low levels of apoptosis and a more proliferative nature of melanoma cells in comparison to breast cancer cells, causing the spheroid to remain intact. In addition to measuring the electrical characteristics of melanoma spheroids, the MCA electrode device was used to monitor electrically active cardiomyocytes. By cycling between multiple electrode pairs, an impedance map was produced, allowing for the position of the spheroid within the cavity to be deduced [63].

The signal to noise ratio of this design was enhanced by Krinke to observe neuroblastoma spheroids a miniature model for Alzheimer's disease (AD) [107]. Neuroblastoma spheroids exposed to okadaic acid (OA) form hyperphosphorylated tau protein similar to the processes believed to cause AD-associated neurodegeneration. In order to assess pathological neurdegeneration, SH-SY5Y cell lines were genetically altered to express either wildtype normal tau (0N4R) or mutant misfolded tau (P301L) protein. The misfolded tau aggregates faster accelerating neurodegeneration. Five day old SH-SY5Y wildtype and mutant spheroids were inoculated with concentrations of OA of 0, 1, 5, 25, 50 and 100nM.

An average between horizontal and vertical electrode pairs (Figure 3-2a) was used to reduce variation due to spheroid shape, and relative impedance was calculated based on baseline measurements (no cells), normalized (to controls) and recorded at the frequency where there was a maximum ΔZ. It was found that both cell lines, once

exposed to OA, saw a dose dependent decrease in relative impedance based on the concentration of OA exposed to the spheroid. A more pronounced decrease in the transformed cell line indicated increased neurodegeneration as a result of increased aggregation of the hyperphosphorylated mutant tau protein as evidenced by western blot analysis.

Although the MCA-based device presented successfully captures the impedance of several 3D cellular models, it suffers from measurement variations induced by placement and size of the sample. For high throughput systems this could lead to a problem in automation, because variations of sample size will impede exact placement of the sample causing changes in the measured impedance. In addition, studies performed on this system lack temporal resolution because they are performed at a specific time-point and do not take advantage of the EIS potential as a monitor of real-time and dynamic impedance changes. The MCA chamber is not conditioned for long-term viability and measurements of the tissue models. Potentially valuable data on the pathology is lost by making measurements at single, punctuated timepoints. In this system, spheroids are removed from the potential toxicant (CPT and OA) as well as the culture medium, potentially inducing changes that may affect the overall impedance. It is of note that although impedance over a large frequency was investigated only a single frequency was used for analysis. By analyzing data over a larger frequency range it may be possible to assess more information on the processes underwent within the culture.

Groups have also investigated systems that utilize microfluidic traps to capture and gauge the impedance of samples, similar to what has been done with single cells.

A system utilizing an hourglass shaped glass microcapillary filled with culture medium containing four electrodes (300 µm platinum wires) integrated at the openings has been produced for monitoring bioimpedance (Figure 3-1b). Spheroids that are smaller than the 300-400 µm glass passageways are hydrodynamically trapped within the passageway by a precision pump [108]. In an investigation of the effect of genetic modification on apoptosis, cells were transfected with antisense-5' butylrylcholinesterase (BchE) cDNA to inhibit the production of BchE a known embryonic proliferation marker. Impedance measurements revealed lower impedance values for tumor spheroids transfected with antisense-5' butylrylcholinesterase (BchE) cDNA compared to control spheroids. DAPI staining confirmed that transfected spheroids underwent an increase in apoptosis and necrosis caused by inhibition of the (BchE) gene. Using impedance it was shown that increases in the apoptosis of MCS post-transfection could be detected using impedance, demonstrating EIS as an effective means of monitoring spheroidal response to factors other than external stimuli [109].

Other gene modification studies have been done utilizing the same microcapillary system. Aggressive breast cancer cell spheroids were created by transfecting T-47D clone 11 cells with vectors to either decrease production of caspase-3, a known apoptosis precursor, or promote overexpression of the apoptosis suppressor protein, Bcl-xl. Control spheroids were transfected with pEGFP. 3D tissue models of these cells were treated with the anticancer drug methotrexate (MTX). Impedance results mirrored activity found through traditional biochemical assays including the tunnel assay and Western blot. A decrease in caspase-3 activity (verified by Western blot) was detected as an increase in extracellular resistance for transfected cells. After exposure

to MTX, a decrease in total impedance was detected. Decreased apoptosis (verified by Tunnel assay and DAPI staining) in transfected cell lines after MTX exposure resulted in higher impedances for the two transfected cell lines [61].

In another study, differentiation of human mesenchymal stem cells (hMSCs) was compared between 2D cell layers and 3D aggregations after chemically inducing osteogenic differentiation. Cells were cultured as spheroids on gyratory shakers and as monolayers across planar electrodes and incubated with dexamethasome, l-ascorbic acid and β-glycerophosphate to induce osteogenic differentiation. Impedance of cellular monolayers was fit to a simple equivalent circuit of a resistor (R_{cl}) and capacitor (C_{cl}) in parallel, representing the parameters of the cell layer. A rapid increase in Rcl occurred during the first 2 days of measurements followed by stabilization. After treatment with the osteogenic medium a large increase in Rcl was observed in comparison to the control. In addition to control and osteogenically differentiated embryoid bodies (stem cell spheroids), necrosis was induced by incubating with Mikrozid liquid. EBs tested at frequencies between 100 Hz to 100 MHz demonstrated that at lower frequencies there was a significant increase in the impedance of differentiated EBs when compared to control and necrotic EBs. In contrast, necrotic cells showed a decrease in impedance magnitude for frequencies up to 10 kHz, indicating a decrease in cell density due to necrosis. It is shown that hMSCs undergoing osteogenic differentiation exhibited similar impedance behavior both in monolayers and 3D embryoid body cultures [54].

Tetrapolar (4-electrode) measurements used in this system have the advantage of removing the interfacial components of the impedance due to electrode polarization and the capacitive double layer. This allows one to observe changes at the lower

frequency, also known as the α-dispersion, which can be attributed to changes in ionic diffusion and the membrane structure of cells on the exterior of the spheroid [110, 111]. This is reflected in the data as a decrease in the impedance due to apoptosis. Although this system has the ability to observe low frequency impedance changes, it has not been proven capable for making impedance measurements in real-time.

Without real-time measurement capabilities, it is not possible to track the progression of the effect of a potential therapy. In addition, impedance alone is not yet sufficient to assess the effects of a potential therapy on a tissue model. The inclusion of parallel environmental and metabolic sensors can greatly increase the predictive power of impedance based systems for high-throughput drug screening.

Table 3-1 Summary of spheroid morphology monitoring techniques.

Techniques	Advantages	Disadvantages	Examples
Electrical Impedance	High temporal resolution Quantitative measure Noninvasive Label-Free Easily automated Does not require dissociation of spheroids	Lacks spatial resolution Lack of specificity w/o additional sensors May not reveal cellular mechanisms behind response	[4, 58-61]
Phase Contrast/Fluorescence Microscopy	Noninvasive Easily automated High temporal resolution	Labeling stains Dissociation of spheroids Only sensitive to surface cells	[100, 101]
Confocal/Light Sheet Microscopy	Capable of 3D imaging of large spheroids(light sheet) Noninvasive High temporal resolution	Only sensitive at low penetration depths w/o fluorescent labels (confocal) Require specially engineered cells (light sheet) Not scalable to high throughput	[95, 96, 102, 103]

Table 3-2 Summary of EIS bioimpedance monitoring techniques.

Culture Type	Advantages	Disadvantages
Single Cell Impedance	Useful for cell sorting Cells-based sensors High resolution (can detect ion activity)	No cell-cell or cell-matrix interactions Pathologically insignificant No evironmental monitoring
Monolayer Impedance	Utilizes standard cultures Simple equivalent circuit modeling Well established for cellular adhesion, kinetics and cytotoxicity	Lack cell-specific function/*in vivo* similarity Little spatial resolution No cell-cell cell-matrix interactions
Spheroidal Impedance	High *in vivo* similarity High Potential for Cellular Differentiation monitoring Drug screening Spheroidal Cell Model Monitoring	Difficult equivalent circuit modelling Insufficient alone for pathological assessment Little spatial resolution No environmental monitoring

(a)

(b)
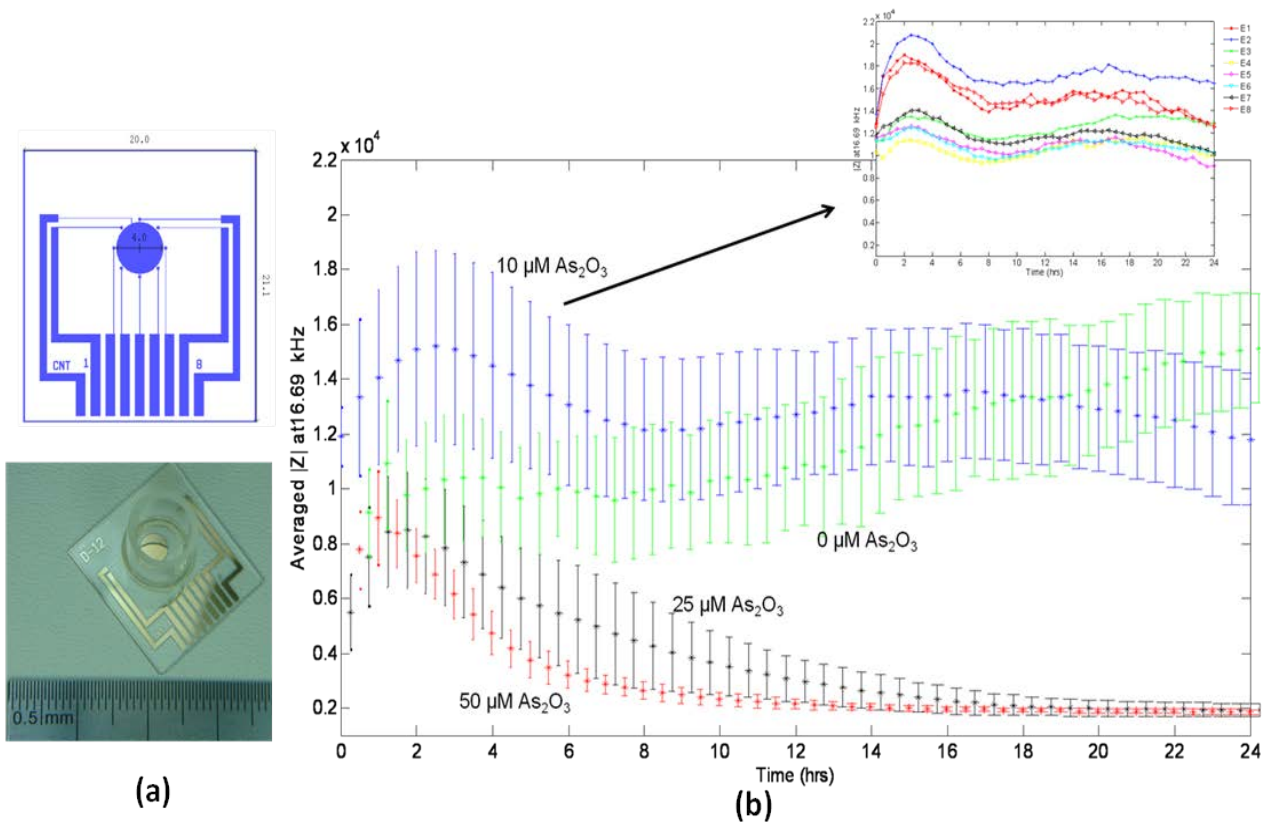
Figure 3-1 (a) Schematic and image of one 8-electrode array device. (b) Averaged |Z| vs. time at 16.69 kHz of HEY cells introduced to 0, 10, 25, and 50 µM As_2O_3
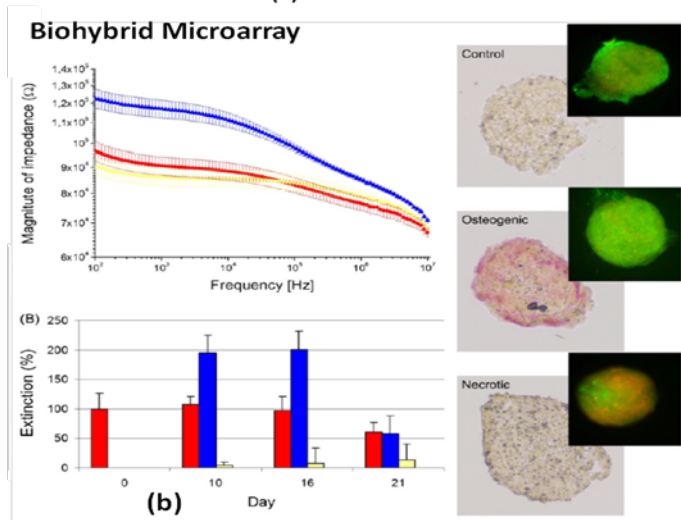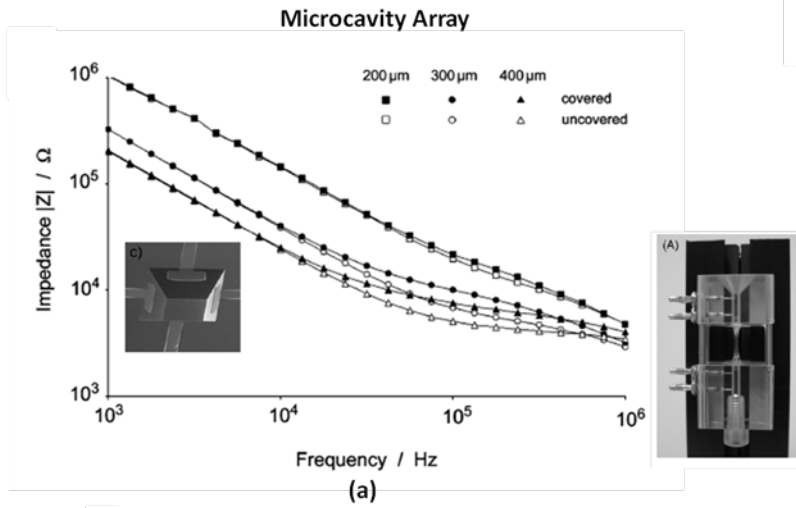
Figure 3-2 Examples of EIS analysis of MCS: (a) biohybrid microarray system [6] and (b) microcavity array device [59].

Chapter 4: Electrochemical Impedance Analysis of Cells: Improving the ECIS Technique[1]

4.1 Introduction

To date, an increase in the demand for quick and reliable medical diagnostics has sparked trends in the development of MEMS devices for biosensing. MEMS devices and sensors are ideal for future medical diagnostics. Their ability to manipulate and analyze very small volumes will lower the sample size required from patients, resulting in less invasive procedures. In addition, their small form factor, enables them to be implanted within a patient, provided it is composed of biocompatible materials. In the future, biosensors will be incorporated into both portable lab-on-a-chip and in vivo devices for quickly running diagnostics on tissue samples and continuous monitoring of patients.

However, the chief barrier preventing implantation of sensors within the human body is the foreign body response of the immune system and the native toxicity of sensor materials. When foreign materials, like silica nanowires, are implanted, the inflammatory response may differ depending on the characteristics and sensitivity of cells in the implant region [104]. For this reason, ECIS-based techniques can be used as a fast and real-time assessment for the toxicity of nanoparticles and biomaterials.

---

[1] Chapter 4 adapted from Ref. 174 with permission from The Royal Society of Chemistry.

4.1.1 Motivation for Nanowire Studies

As cellular uptake of nanowires can lead to cellular necrosis, maintaining tuneable properties such as diameter length and chemical composition play a key role in avoiding cytotoxicity [105]. Silica nanowires, specifically, offer a solution to this problem due to their biocompatibility with human cellular material and current use in the field of biological sensing. In addition, silica nanowires can be grown directly on sensor surfaces fabricated on silicon substrates [78]. Creating a simple approach to biosensor fabrication that can be readily translated to high volume fabrication.

For these reasons, silica nanowires have been investigated in several types of biosensors used in nanowire-enabled sensors for biomarker detection [106, 107]. Efforts are now underway to use these nanowires for *in-vivo* sensing. However, prior to implementing nanowires into active biosensors that interact with tumor cell models, the toxic effects of nanowires on the cells, if any, due to prolonged exposure must be assessed. Thus, Hs 578T epithelial breast cancer cells were chosen to explore the cytotoxicity of Pd catalyzed silica nanowires. Historically wire drug interactions have been studied with endpoint assays and a real-time measurement system has always been desired. In this work, we report on the cytotoxic effects of Silica nanowires on epithelial breast cancer cells using real-time electrical impedance spectroscopy (EIS) measurements.

EIS has been used for decades for studying cellular interactions in real time [35, 108]. These techniques improve on currently available assays that require chemical tags and a lengthy time for processing. By applying a small voltage to a biological sample and measuring the resulting current over a range of frequencies, changes in the

electrical impedance of cell culture models [48], multicellular spheroid (MCS) [59], or antibody binding [16] can be monitored. For example, impedance work has been performed to examine carrier density's in Zinc nanowires [109]. However, few impedance studies have been found in literature that examines the effect of nanowires on cells.

4.1.2 Need for Improvement

The commercial ECIS system and the xCELLigence system from ACEA Biosciences Inc. are currently the premier systems for performing impedance-based analysis for cellular cultures. However, as stated in earlier sections, these systems currently suffer from several key drawbacks that prevent them from being suitable for evaluating cellular response to nanoparticles. A lack of spatial resolution in measurements decreases the statistical significance of experiments and averages the cellular response of a large working area, erasing any area-specific impedance changes. For this reason, a new multi-electrode array design was designed and tested to assess the effect of silica nanowires on epithelial breast cancer cells. The work in this chapter demonstrates the ability of the newly designed 8-electrode array to monitor cell-nanowire interactions in real-time in a spatially specific manner, by studying the effect of varying concentrations of nanowires on breast cancer cells.

4.2 Experimental

4.2.1 Nanowire Synthesis

Silica nanowires (NW's) were grown using the vapor liquid solid method [110, 111] on 4" silicon wafers. Initially, the Si substrates were cleaned with buffered oxide etchant to remove any native oxide formed on the surface and a 5 nm thin palladium

was deposited via e-beam evaporation as growth catalyst. An open-tube furnace was used for growing the nanowires, which was heated to 1050°C and purged with Argon during the entire process. Argon served as a carrier gas for vapor phase silicon and to remove contaminating species from furnace tube. The Pd-sputtered Si substrate was placed on a bare Si wafer and placed onto a quartz boat, which was loaded into the open-tube furnace. The sample was annealed for 60 minutes at 1050° C, to yield a dense formation of wires that would be suitable for characterization and cell testing. Figure 4-1a shows an SEM image of the nanowires grown with this process. Scanning Electron Microscopy (SEM) revealed the nanowires to have diameters on average of 100-200nm in width and EDS verified wire elemental composition to be silicon and oxygen with Palladium growth catalyst dispersed along the length of the wire.

4.2.2 Microelectrode Device Fabrication and Preparation

Microelectrode arrays were fabricated in order to monitor monolayers of Hs578T epithelial breast cancer cells (ATCC: HTB-126). The electrode geometry, shown in figure 4-1b, contains a circular array of 8 working microelectrodes (diameter = 250μm) with a single counter electrode (diameter = 4mm) in the center. The counter electrode is made much larger than the surrounding working electrodes in order to ensure that the impedance of the cellular monolayer dominates the measured impedance as opposed to impedance of the electrodes. Electrodes were designed in order to increase the spatial resolution over currently available electrode designs. By incorporating a circular array of working electrodes, multiple areas of a single culture are monitored during a single experiment. In addition to increased spatial resolution, this incorporates measurement redundancy, an essential requirement for generating statistically

significant results. The microelectrode arrays were patterned on a 4" glass wafer using conventional lithography technique followed by thin film deposition of Cr (15nm) and Au (60nm) to define the microelectrodes and contact pads. Later, the electrode tracks were insulated using SU-8 and cloning cylinders were attached to the devices using SU-8 to hold the culture medium and cells covering the electrodes. The cloning cylinders were reinforced and leak-proofed using high vacuum grease. The fabricated devices were cleaned with isopropanol, deionized water, and then sterilized by dry heat sterilization for 90 minutes in an oven at 170°C.

4.2.3 Cell Culture and Inoculation

Hs 578T epithelial breast cancer cells (ATCC: HTB-126) were cultured in Dulbecco's Modified Eagle Medium (DMEM) supplemented with 10% Fetal Bovine Serum (FBS), 0.01 mg/ml bovine insulin and 1 mg/ml penicillin streptomyacin antibiotics (all amounts indicated are final concentration). During culture and experiments, cells were kept in a humidified atmosphere (incubator) at 37°C and 5% CO_2. Cells were grown to 90% confluence and then harvested using a 25% trypsin/EDTA solution. Viable cells were then removed to a separate flask and counted using a hemocytometer and the tryphan blue exclusionary technique. Prior to cell seeding microelectrode surfaces were pre-treated with 0.1% Type B bovine gelatin solution (Sigma). Microelectrode arrays were incubated with gelatin solution for 30 minutes and then rinsed with complete culture medium prior to cell seeding. This surface treatment improved cellular attachment to electrodes for experimental impedance monitoring. Cells were then seeded onto impedance devices at a density of ~$2x10^4$ cells/device.

Microelectrodes were connected to the switching circuit located inside an incubator and monitored for 24 hours or until baseline measurements stabilized.

4.2.4 Nanowire Preparation and Inoculation

Pd-catalyzed NWs were scraped from the growth substrate and weighed to be approximately 200 µg. In order to avoid contamination, NWs were then sterilized in an oven at 170°C for 90 minutes. Sterilized NW's were then added to 1mL of sterile growth medium (DMEM) and dispersed using ultrasonic agitation for 1 minute. A stock solution of NW/DMEM of 200 µg/mL was refrigerated at 4°C until needed for further dilution and cell inoculation.   Cells were inoculated with nanowire-medium solution with final concentrations of 1 µg/mL, 50 µg/mL, and 100 µg/mL.

4.2.5 Impedance Measurements

An Agilent 4294A Impedance Analyzer was used to make impedance measurements. Measurements were recorded using a 10 mV peak to peak voltage over a frequency range of 100 Hz to 1 MHz and were kept in an incubation chamber at a temperature of 37.1°C and an atmosphere consisting of 5% CO_2 to stabilize the environment for continuous cell growth. Impedance measurements were controlled remotely using an HP Desktop computer with Labview software and an in-house switching circuit capable of monitoring 4 devices in parallel. In order to provide electrode functionality, baseline measurements were recorded using DMEM growth medium prior to cell seeding.   Damaged electrode connections, due to residual photoresist or scratched electrode contacts, were discarded at the end of the baseline experiment.

Next, cells were seeded onto devices, and cellular impedance was monitored for 24 hours prior to inoculation with nanowires. Once cells reached 100% confluence and

cellular impedance stabilized, cells were removed from the incubation chamber and varying concentrations of nanowire solutions (0 µg/mL, 1 µg/mL, 50 µg/mL, and 100 µg/mL) were then prepared and seeded into the devices as described in the previous section. Finally, cells were immediately returned to the incubation chamber and the impedance of each device was then recorded once per hour for a minimum of 24 hours for real-time monitoring of cellular impedance.

Experiments were performed in order to extrapolate the effect of the gelatin coating on measured impedances. Briefly, devices were incubated with DMEM for 2 hours at 37° C and impedance measurements were recorded every 30 minutes. Upon conclusion of recording the medium impedance, DMEM was removed and devices were rinsed with PBS solution and DI water and dried via nitrogen gas. Next, gelatin coating was deposited over electrodes as described in section 4.2.3 and 500µL of DMEM culture medium was pipetted over the electrodes. Baseline measurements were recorded in 30 minute intervals for a period of 2 hours.

4.2.6 Equivalent Circuit Modeling

Internally designed Matlab programs and Excel (Microsoft) spreadsheets were used to calculate impedance magnitude and phase data recorded by the impedance analyzer. Initially, Bode plots were used to visualize magnitude and phase data calculated for each measurement on a specific device. In order to assess changes in the culture, a time plot was then created; monitoring the average |Z| calculated at 96.49 kHz. This frequency is significant because it lies within the "beta dispersion" where the capacitive impedance contributed by the cellular membrane is highest [112, 113]making it a good indicator of cellular activity. Equivalent circuit modelling via Matlab was used to extract parameters for baseline measurements. Two different equivalent circuit

43

models were used to fit data using the complex nonlinear least squares (CNLS) method. Initially, all data was fit to (Figure 4-2a) denoting lack of cellular presence. CPE_{dl} represents the double layer capacitance at the electrode interface and R_s represents the solution resistance. Data was next fit to (Figure 4-2b) to detect cell presence. Fit accuracy was evaluated by sum of squared error (SSE); where, parameters extracted with the smallest SSE value were taken to represent the system.

4.3   Results and Discussion

4.3.1 Effect of Gelatin Coating on Medium Baselines

Equivalent circuit parameters including R_s, n, and CPE_{dl} were extracted for all 8 electrodes over each measurement. Figure 4-2(a) indicates that Rs values extracted from the impedance data are nearly identical after an hour of stabilization. This is because the solution resistance of the DMEM remains unchanged with the addition of the gelatin coating. Figure 4-2(b) and X(c) display the CPE parameters CPE_{dl} and n. It can be seen that the standard deviations on all figures overlap indicating an insignificant difference between coated and uncoated electrodes. It can also be seen that the calculated CPE values are much higher than the estimated capacitance values of 10-20 µF/cm2. This is due to the non-ideal behavior of the CPE parameter and the existence of the n-value.

4.3.2 Baseline Characteristics of Cellular Monolayer

In order to prove device functionality baseline measurements were first recorded for devices using only culture medium. This ensured electrode connectivity and provided a reference to compare with measurements of confluent cellular monolayers. The extracted parameters for the baseline (Figure 4-3a) indicate that no cellular

presence is detected within the culture and the impedance of the system is best approximated as a solution resistance in combination with the double layer capacitance. Baseline impedance values at 96.49 kHz measured for each functional electrode (non-functional electrodes not reported) were recorded and used as normalizing factors for all future time plots of monitoring impedance changes. Values close to one indicate baseline characteristics and a very small change in impedance.

A time plot of data collected from the six independent working electrodes located on one device is shown in Figure 4-3c, as an example of the increased spatial resolution made possible with this electrode design. It can be seen that at time zero, impedance measurements are very close to unity, indicating that while cells are present in the culture area, they have yet to spread over the electrodes and contribute to the impedance. Over the next 6 hours the impedance begins to increase rapidly due to cellular attachment to the substrate, eventually settling between an impedance increase of a factor of 1.5 and 2. It is important to note that the rate of increase varies over different electrodes, indicating differences in cellular coverage within the chamber. The measured impedance responses for electrodes D1-D6 on the electrode map correspond directly to specific spatial locations within the culture (see section C.2). From this data it can be inferred that the majority of cells initially attached to the area surrounding electrodes D4-D6. Cellular migration and division cause the impedance measured by other electrodes to rise when cells spread across them as time progressed.

After 6 hours, dedicated increases in impedance begin to taper off and measured impedance begins to fluctuate for each electrode indicating cellular confluence. The small fluctuations over time correspond to the micromotion of cells across the surface of

the electrodes, as seen previously in prior studies [48]. Equivalent circuit parameters extracted 24 hours after cellular seeding (Figure 4-3b) confirm cellular presence. The equivalent circuit model representing cell presence was chosen because SSE values were smaller than SSE values obtained with the alternate equivalent circuit model.

4.3.3 Cellular Impedance Response to Nanowire Inoculation

After 24 hours of incubation, devices were then seeded with concentrations of nanowires including: 0μg/ml 1μg/ml, 50μg/ml, or 100μg/ml. Figure 4-4 shows the impedance response of the cancer cells to various concentrations of nanowires. A small increase after the first hour can be attributed to an initial decrease in impedance caused by being removed from the incubation chamber and restabilizing once returned to standard growth conditions. Over time, only controls and cells seeded with 1μg/mL of nanowires remained attached and spread onto the electrodes. Cells that remained viable on the electrodes exhibited a stable impedance magnitude that continued to fluctuate in a small range due to cellular micromotion and activity.

Cells inoculated with concentrations higher than 1ug/ml, in contrast, showed dedicated reductions in impedance magnitude immediately after initial seeding. After approximately 30 hours, cells exposed to the highest concentration of nanowires (100ug/ml) reached near baseline characteristics. This indicates that all cells had completely detached from the surface, resulting in cell death.

In this study, real-time impedance responses were used to monitor cellular bioimpedance of the epithelial breast cancer cell line Hs578T in response to palladium catalyzed silica nanowires. Online cellular impedance measurements verified the results of previous studies indicating that a high concentration SiNW negatively impacts

the viability of a confluent cellular monolayer [114, 115]. Julien et al. examined the mechanisms of cell death induced by exposing 3T3-L1, HeLa and Panc10.05 cellular cultures to silica nanowires and examining the effects at multiple time points. Cell counts taken using the tryphan blue exclusionary technique indicated that cells exposed to silica nanowires continued proliferative activity at the control concentration of 37µg/ml, compared to cells exposed to the apoptosis inducer cycloheximide (CHX) which resulted in cell death. Further inspection showed relatively low caspase 3 and 7 activity indicating that minimal apoptosis is induced upon exposure to silica nanowires alone. This suggests that cell death due to nanowire inoculation occurs mostly because of necrotic processes, induced by physical displacement from the surface as opposed to apoptotic processes induced by cytotoxic effects of the nanowires. Our data revealed similar trends, showing an inert response to silica nanowires at 1µg/ml concentrations for periods up to 48 hours (data not shown) with no negative effects on cellular proliferation monitored via the cellular impedance. Higher NW concentrations resulted in decreases in the cellular impedance (Figure 4-4) representing weaker tight junctions and cell adherence to the electrodes, eventually leading to total cell death within the first 24 hours of exposure. Our impedance based system was capable of real-time monitoring via multiple measurements of a single culture improving the temporal resolution available to procedures using standard assays, reducing the need for redundant samples.

In addition, the inertness of silica nanowires is further supported by the apparent spatial dependent response to nanowire inoculation at 50µg/ml. Figure 4-5a shows that decreases in cellular impedance did not occur in concert.   A sharp reduction in

impedance is first seen at electrode D1after six hours post NW-seeding. At 18 and 20 hours, the impedance at electrodes D2 and D3 drop significantly. Finally, at approximately 36 hours the impedance drops at the remaining electrodes indicating total cell death. The staggered effect on the impedance can be attributed to the random distribution of nanowires within suspension. Qi et al. examined the effect of high concentrations of nanowires on cellular adhesion by incubating HepG2 cells with 100ug/ml of silica nanowires immediately after cellular seeding. 62.5% of cells were found to be adherent after 18 hours of incubation when compared with cells incubated alone. Scanning electron microscopy (SEM) and energy dispersive X-ray spectroscopy (EDS) found that rounded and poorly adherent cells had high levels of silicon surrounding them. Additionally, reverse transcriptase polymerase chain reaction (RT-PCR) found a down regulation in expression of adhesion specific proteins integrin, FAK, and Col I.

Our recorded impedance data confirms that areas exposed to larger amounts of NW died off faster than those in areas with lower amounts.   After impedance measurements were complete, devices were imaged using SEM (Figure 4-5b). It can be seen that areas surrounding electrodes contain a higher concentration of NWs which impeded cellular adhesion to the surface causing cell death. Furthermore, it was seen that cells can also be mechanically punctured by the NW. Finally, these results demonstrate a unique approach to studying the interactions between biomaterials and nanomaterials. By integrating a new electrode design, multi-spatial monitoring of a single cellular culture was realized.

4.4 Conclusion

A new multi-spatial electrode design and real-time impedance monitoring system were used to demonstrate a potential application of monitoring the bio impedance of biological systems. Quantitative impedance measurements were used to verify prior experiments that found that lower concentrations of silica nanowires are inert when exposed to cellular cultures, evidenced by stable fluctuations in the measured impedance overtime. At concentrations of 50 and 100ug/ml nanowires have fatal interactions due to mechanical disturbances that prevent proper adhesion to the surface. Due to the capability of this system to work in real-time, it improves upon the design of traditional experimental assays because it allows a higher number of time-points to be assessed without the need for increasing the number of experimental samples. Also, the use of an 8-electrode array enables multiple measurements of the same sample, adding spatial resolution and statistical value through measurement redundancy. By offering quantitative, real-time, and non-destructive measurements of nanowire-cell interactions, this system is a viable complement to standard endpoint assays.
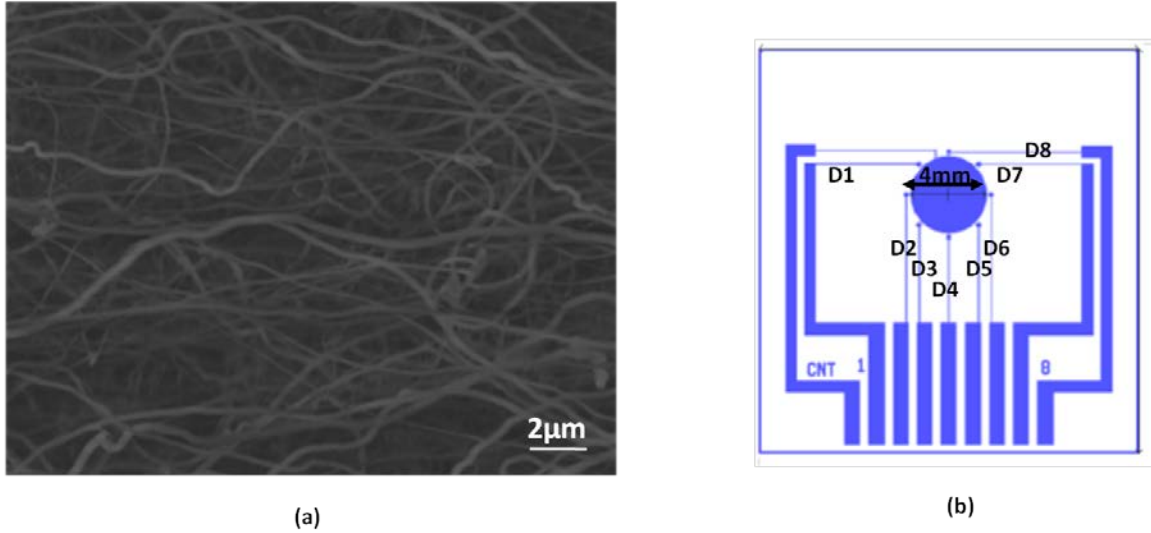
Figure 4-1 (a) SEM image of silica nanowires (SNW) annealed for 60 minutes at 1050°C. (b) Map of 8-electrode array surrounding large counter electrode.
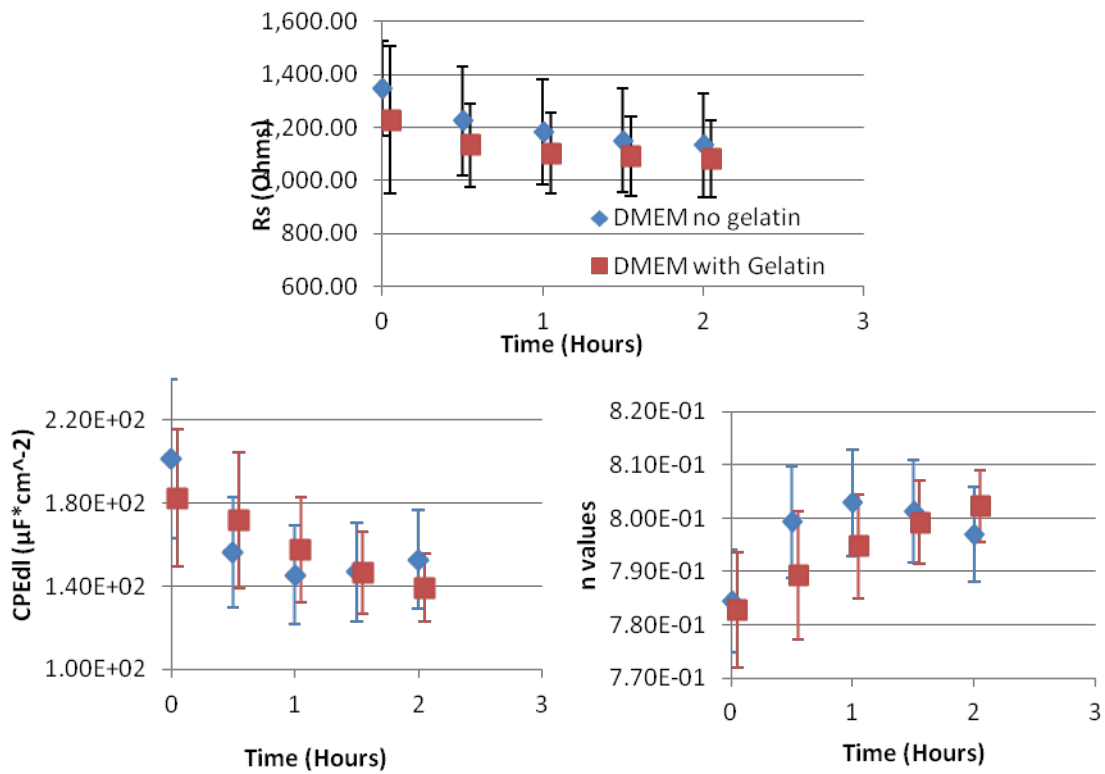

Figure 4-2 Comparison of extracted (a) resistance (b) CPE and (c) n values of DMEM culture medium taken from coated (red) and uncoated (blue) electrodes.

(D07)	Rs	CPEdl-T	CPEdl-P	Sum-Sqr
D1	2.62E+03	1.97E-08	8.16E-01	2.89E-01
D2	2.39E+03	2.01E-08	7.99E-01	1.74E-01
D3	2.45E+03	9.97E-09	8.45E-01	1.49E-01
D4	2.20E+03	1.13E-08	8.17E-01	1.13E-01
D5	2.21E+03	6.91E-09	8.62E-01	1.44E-01
D6	2.27E+03	7.07E-09	8.60E-01	1.34E-01

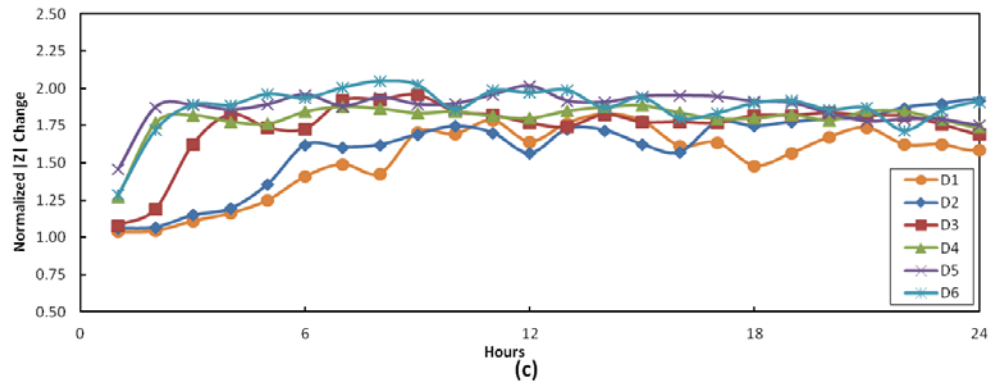| (D07)	Rs	CPEdl-T	CPEdl-P	Rcell	CPEcell-T	CPEcell-P	Sum-Sqr
D1	2.07E+03	2.40E-08	8.16E-01	6.07E+03	8.33E-08	5.96E-01	1.20E-02
D2	2.05E+03	1.91E-08	8.25E-01	5.94E+03	4.79E-09	7.84E-01	1.21E-02
D3	1.60E+03	6.34E-09	9.19E-01	7.52E+03	1.25E-07	5.50E-01	7.62E-03
D4	1.64E+03	8.01E-09	8.77E-01	4.97E+03	6.17E-08	5.92E-01	7.62E-03
D5	1.60E+03	6.33E-09	8.96E-01	4.91E+03	4.16E-08	6.26E-01	9.13E-03
D6	1.67E+03	7.14E-09	8.94E-01	6.73E+03	3.65E-08	6.33E-01	1.33E-02

(a)

(b)

(c)

Figure 4-3 Results for equivalent circuit fitting of impedance data. (a) Baseline equivalent circuit model without cellular presence and (b) with cellular presence; (c) |Z| at 96.49 kHz normalized to baseline measurements over 24 hours after initial cell seeding (Device D07)

Figure 4-4 Average normalized |Z| values for concentrations of 0µg/ml, 1µg/ml, 50µg/ml and 100µg/ml after SNW inoculation.

Figure 4-5 (a) Single device showing spatial response of cells after nanowire exposure. (b) SEM micrograph showing cell in high concentration on SNW.

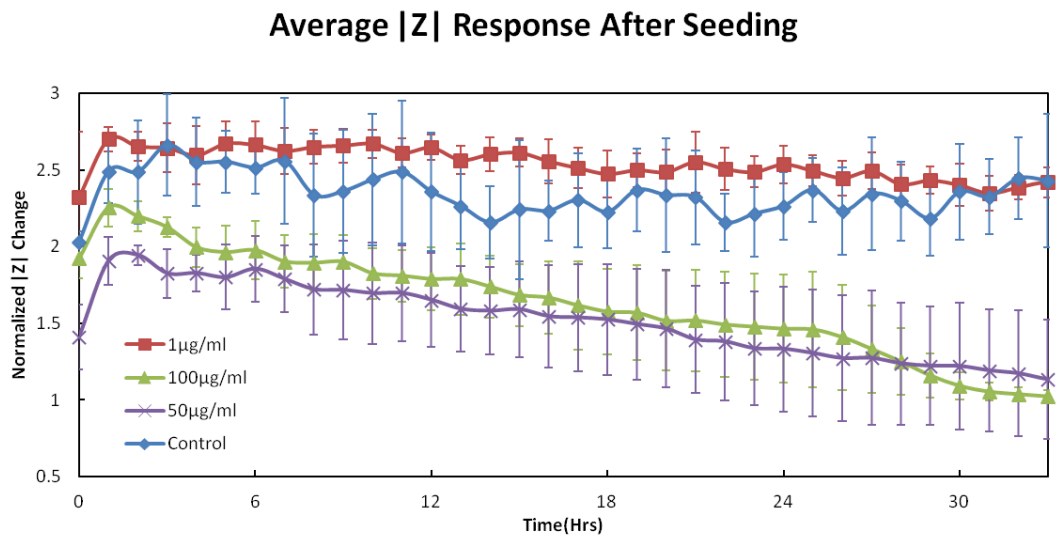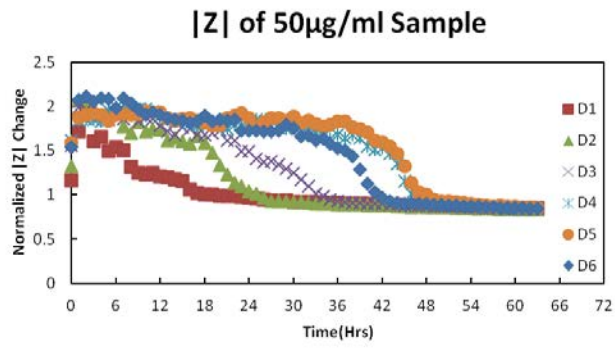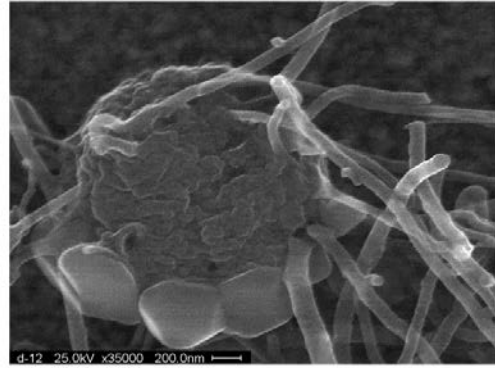## Chapter 5: Simulation, Design, and Testing of Electrodes for Impedance Characterization of Tumor Spheroids

5.1   Introduction

Increased spatial resolution is an essential improvement to move impedance-based assays into the arena of high-throughput drug screening. The proposed method to address this needed increase in spatial resolution is to utilize microelectrode geometries, which are capable of probing multiple depths into cellular tumoroids. To accurately define the area being interrogated, thorough consideration must be placed upon the electrode design. For this reason, it is necessary to carefully design the electrodes to understand the relationship between electrode spacing and the penetration depth of the electric field.

An additional consideration for impedance monitoring of 3D cellular models is minimizing the contribution of the culture medium (R_s). Adherent cell lines that attach directly to electrodes in ECIS-based systems create a barrier between R_s as they reach confluence (as seen in Figure 5-1). This forces the current to flow between tiny intracellular spaces or through the cellular membrane prior to coming in contact with the culture medium. In contrast, when 3D cellular models are used, cells attach to each other and do not actively adhere to the measuring electrodes. This allows the culture medium to come into direct contact with the measuring electrodes, causing R_s to shunt the cellular parameters. In order to mitigate this shunt resistance, the electrode design should maximize electrode contact with the cellular sample and minimize contact with

the culture medium. Microneedle electrodes achieve this by positioning the measuring electrodes directly inside the cellular sample, isolated from the culture medium. In this work, passivated microneedle and planar electrodes were designed simulated and compared for impedance measurements of tumor spheroids.

Microneedle electrodes were fabricated using a combination of photolithography, dry etching, and electroplating techniques and two etching techniques were evaluated for optimal needle formation. Planar electrodes were fabricated using MEMS fabrication techniques and evaluated for impedance experiments.   The effect of electrode passivation on measurement sensitivity was characterized for planar electrodes and unpassivated electrode behavior was characterized using KCL and Dulbecco's Modified Eagle Medium Solution (DMEM).   Finally, unpassivated electrodes were used to characterize the effect of electrode spacing on impedance measurements of tumor spheroids.

5.2   Design of Microneedle Electrodes for Tumor Spheroid Impedance Monitoring

5.2.1 COMSOL Simulations

In order to characterize the shape and penetration depth of the electric field of these microelectrodes, FEA simulations were performed to visualize the magnitude and direction of the electric field lines using the electrostatic solver. Comsol calculates these parameters by solving for Ohm's Law:

$$J = (\sigma + j\omega\epsilon_0\epsilon)E + J_e$$

where E is the electric field, ρ is the space charge density and ε is the relative permittivity and ε_0 is the permittivity of free space.

Initially, conical microneedle tips were approximated in 2D as isosceles triangles with base widths of 50 microns and heights of 43.263 microns. Simulations were enclosed in a boundary area of 200µm x 400µm (80,000µm^2). The simulation area was given an electrical conductivity of 1.47S/m and relative permittivity of 75.97 to approximate Dulbecco's Modified Eagle Medium (DMEM) [116]. The boundaries of the triangles were simulated as gold with an electrical conductivity of 45.6e6 S/m. Electrical current simulations were performed giving terminal characteristics to both of the triangles. Terminal 1 (the first triangle) was given a voltage of 100mV and terminal 2 was given a voltage of 0V as seen in figure 5-2. Electrode tips were spaced in increments of 25µm from 25µm-250µm from base to base.

Figure 5-3 shows a two dimensional surface plot of the distribution of the electric field emanating from the two electrodes in the simulation space. Because electric potentials are applied directly on terminal 1 and terminal 2, the strength of the electric field is strongest at the innermost tips of the electrode surface. Furthermore, it can be seen that much of the electric field is concentrated directly between the needle tips as expected. The maximum electric field measured at the electrode tips is approximately 4178 V/m. In order to assess signal distribution above the electrodes, a reference line was drawn along the midpoint between the terminals to calculate the magnitude of the e-field.

From figure 5-3, it can be seen that midway between the two terminals, the magnitude of the E-field reaches a minimum. One can see, at this point a measured

sample will experience minimum exposure to the applied electric field. For this reason this midpoint is used to find the effective penetration depth of the electric field into the sample. Above the points of the electrodes, the field decreases to 1000V/m 4µm above the electrodes and further decreases to 500V/m 50µm above the tips. This indicates that in pure medium the majority of the current will be passed directly between the electrodes but maintains intensities greater than 500V/m as far as 50 microns above the electrodes.

Further analysis revealed that increasing the electrode spacing causes a significant decrease in the maximum magnitude of the electric field (field located at electrode tips). Increasing the electrode spacing from 50 µm to 75 µm corresponded with a 26.8% decrease in the maximum electric field (4178V/m to 3058V/m). This can be attributed to a spreading of the electric field created by a larger distance between the electrodes.

However, in addition to the decrease in total electric field magnitude there is a noticeable change in the distribution of the electric field. Figure 5-4 shows a plot of the percentage of the total electric field as a function of the height above the electrodes along the midpoint between the electrodes. As electrode spacing increases, the distribution of the electric field extends further above the electrodes.

For a microneedle electrode design with 25 micron spacing, approximately 75% of the electric field is constrained between the electrodes, leaving only 25% of the electric field extending beyond the tips of the electrodes. As the spacing of the electrodes increases, the penetration of the field into the space above the electrodes also increases until reaching saturation at spacing greater than 225 µm. Upon reaching

225 μm a saturation point is reached due to the finite current applied to the system and the penetration depth starts to slowly decrease as the distance the charge fills becomes larger. This saturation spacing is likely dependent on the initial level of current applied to the electrodes.

5.2.2 Design Considerations

One chief design consideration for microneedle electrodes was the size of tumor spheroids to be measured. Tumor spheroid radii are normally limited by the diffusion length of oxygen to 100μm. However, because hypoxia is a trademark of tumors in vivo, tumor spheroids with larger sizes can be useful for recreating these in vivo characteristics. For this reason, electrodes and microfluidics were designed to support tumor spheroids of a maximum size of 250μm.

Figure 5-5 presents the electrode spacing vs. the depth at which 70% of the total electric field is reached. A logarithmic trend can be used to fit the data, further confirming the saturation spacing for a given voltage. According to simulation results microneedle electrode spacings of 50, 150 and 250 μm 70% of the electric field will extend approximately 27, 60, and 82 μm above the microneedles and into the tumor spheroid.

5.2.3 Fabrication

Gold microneedle electrode arrays were designed with electrode widths of 30, 40, and 50μm. In addition, electrodes were configured in 1 x 4 arrays with progressive spacings of 30, 90, and 150 μm for 30 μm electrodes; 40, 120, and 200 μm for 40 μm electrodes; and 50, 150, and 250 μm for 50 μm electrodes. Microneedle electrodes

were fabricated on 2 inch silicon substrates using standard UV lithography, deep reactive ion etching, and gold electroplating techniques.

Figure 5-6(a)-(f) outlines the process flow for fabricating the microneedle electrodes. Two-inch silicon wafers were first solvent cleaned with acetone, methanol and isopropyl alcohol and then dried using nitrogen gas. A dehydration bake was performed at 150°C to remove all traces of water. An AZ4620 photoresist mask was patterned on silicon wafers to selectively etch the silicon into microneedle geometries. First, hexamethyldisilazane (HMDS) was spun at 3500rpm for 30 seconds to improve adhesion of the photoresist. Next, a layer of AZ4620 was spun at 1500rpm for 1 minute. The thickness of AZ4620 was either 7 μm or 4 μm depending on the etching technique to be performed in subsequent steps. The wafer was then soft-baked in an oven at 90°C for 1 hour. The wafer was then left to rehydrate for 24 hours prior to UV exposure.

Wafers were then exposed using a Karl Suss mask aligner at 25 watts for 55 seconds. Features were then developed using a 1:4 dilution of AZ400K for 5 minutes. Samples were rinsed in DI water and dried with nitrogen gas. The resulting photoresist mask was then hardbaked in a 100°C oven to improve the physical resistance to the subsequent plasma etch. Two dry etching processes using deep reactive ion etching (DRIE) were investigated to produce the microneedle geometry (1) a continuous isotropic etch and (2) a two step isotropic/anisotropic silicon etch. These procedures created sharpened silicon microneedles with various needle tips.

5.2.3.1 Method 1: Continuous Anisotropic Etch

An Alcatel DRIE was used to define microneedle electrodes in a one step high aspect ratio (HAR) etch process.   The Bosch process is used to etch silicon anisotropically by alternating between an etch of octafluorocyclobutane (C_4F_8 @ 200 sccm) and oxygen (O_2 @ 20 sccm) for 1.4 seconds followed by an etch with SF_6 gas (300 sccm) for 3 seconds.   During the etch process, the photoresist mask is etched uniformly from the top in addition to the large amounts of silicon consumed during the Bosch process.   Once the photoresist is etched to less than 1.5 µm, etching begins to occur on the sidewalls, shrinking the size of the photoresist mask and increasing the effective etch area.   For a circular mask, this leads to a conical structure being formed as shown in figure 5-7. By characterizing the etch rate of the photoresist it is possible to etch sharpened microneedles in one continuous step.

Khanna et al. first demonstrated a method of fabricating hollow microneedles with sharpened sidewalls without reducing the total diameter of the microneedle beam. This technique takes advantage of the photoresist depletion to gradually sharpen needles while simultaneously etching the microneedle shaft [117].   In this work they reported an etch rate of AZ4620 of .16-.20 µm/minute [118].   An iterative etching experiment was performed to verify the rate of photoresist consumption and develop a procedure for etching solid microneedles.   Briefly, silicon wafers coated with a 6 µm AZ4620 photomask and were etched iteratively in the DRIE for times of10, 8, 9, and 5 minutes for a total of 32 minutes. After each etching step, the height of the photoresist was measured using a Dektak 3030 Profilometer.

5.2.3.2 Method 2: Two Step Isotropic/Anisotropic Etch

The same Alcatel DRIE was used to perform a two step etch including: (1) a timed isotropic etch to form the sharpened microneedle tips and (2) a 10 minute HAR etch to define the heights of the needles. Isotropic etching of silicon was achieved by etching with a pure sulfur hexafluoride (SF_6) plasma with gas flowed at a rate of 300 sccm. By definition, isotropic etches remove material in all orientations at the same rate. This causes silicon beneath the photoresist mask to be undercut as illustrated in figure 5-8. During the following HAR etch, the exposed silicon is also etched producing a conical tip. The effective etch rate of the isotropic and HAR etches are 5.5 µm and 10 µm, respectively.   Needle tip radii can be estimated by subtracting the calculated undercut from the proposed needle radii as seen in formula (1).

$$r_{needletip} = r_{needle} - etch\ rate * t_{etch\ time}\ (1)$$

Because 30, 40 and 50 µm needle diameters are included on a single wafer, it is important to specify the time of the isotropic needle forming etch. For maximum needle sharpness, microneedle tips should be etched to micron-submicron diameters.   The variation between microneedle sizes prevents all needles (30, 40 and 50 µm from being etched to maximum sharpness on the same wafer. For example, if 50 µm needles are sharpened to sub-micron sharpness 40 and 30 µm needles will be overetched resulting in a complete undercut of the photoresist. For this reason it is necessary to perform multiple runs on different wafers. After defining the needle tips, the Bosch process was used to define the height of the microneedles with a nominal etch rate of 8 µm/min.

5.2.3.3 Metallization of Microneedles

After etching, samples were prepped for electroplating by removing the photoresist mask with acetone and rinsing with methanol and isopropyl alcohol. In order to electroplate gold onto the needles, a seed layer of nickel was first sputtered onto the wafer. Due to surface roughness from micromasking during the DRIE process, microneedles with sharpened tips were not able to be seeded with nickel. Microneedles with unsharpened tips were substituted for proof of concept. RF Sputtering was chosen over other physical vapor deposition (PVD) techniques because the nickel ions are distributed in an omni-directional manner, leading to a conformal coating on 3D surfaces [119]. Next, 3000PY photoresist was spun at 3000rpm for 30 seconds and soft baked at 150°C for 1 minute to form a metallization mask. The mask was then patterned by UV exposure for 23 seconds at 25 Watts. A post-exposure bake was performed at 100°C for 1 minute and the wafer was then developed in RD-6 for 15 seconds. The samples were then rinsed in DI water and dried. TG-25E-RTU gold electroplating solution (Technic Inc.) was used to metalize silicon microneedles.

The procedure for electroplating was taken from Price et al [120]. Briefly, electroplating solution was warmed in a beaker to 55 °C. The solution was stirred constantly with a magnetic stirrer at 100 rpm. A small area of photoresist on the sample was removed with acetone to provide an area to make electrical contact with an alligator clip. The anode (negative terminal) was connected to the wafer and the cathode (positive terminal) was connected to a platinum mesh that acted as a counter electrode. The applied current density used by Price et al was 2 mA. Due to a large reduction of electrode area, the DC current was reduced to .5 mA to reduce the current

density and deposition rate. DC current was applied for 15 minutes to coat the microneedle electrodes in gold.

5.2.4 Results of Fabrication

5.2.4.1 Etch Method 1: Results

Surface profilometry was used to verify the height of microneedles. Because microneedles were formed in trenches, the trench height was taken as the microneedle height. A Dektak D-150 surface profilometer was used to measure trench height. Profiles from the iterative etching experiment are shown in Table 5-1. Because the etch rate of silicon is well characterized for the DRIE (4-10 μm/min), the effective etch rate can be calculated by subtracting the amount of etched silicon from the measured step height. From this, the effective etch rate of the photoresist was found to be .21 μm/min.

Figure 5-9 shows the microneedle mask patterned on a silicon wafer prior to etching and a close up of 30 μm needles immediately after the continuous etch process. Due to the nonuniform etch pattern of the thinned photoresist, needletips appear rough. It is important to note that the etch rate of the photoresist profile is not continuous and begins to slow after the photoresist thickness reaches less than 1.5 μm. This can be attributed to the inclusion of the sidewalls in the etch process effectively decreasing the etch rate of the photoresist profile. After 32 minutes of etching the tips of the 50 μm needles are found to have diameters of ~14 μm and heights of ~200nm.

Because the etch time and needle tip diameter are controlled by the initial photoresist thickness, a longer etch time is needed for thicker photoresists. This lengthy etch time introduced problems with removing the residual photoresist after etching due to the photoresist burning during the process. In addition, micromasking

became more prevalent at longer etch times. For this reason a spin speed of 8000 rpm was chosen for future processes to decrease the photoresist thickness to 3.7 µm and decrease the etch time. Furthermore, it was found that 2 minutes after reaching a height of 1.5 µm was sufficient to sharpen microneedles. In conclusion, to form needles with micron level diameters, the following formula was derived:

$$etch\ time = h * .21\frac{\mu m}{min} + 2\ (min.)$$

where h is the thickness of the photoresist in microns.

5.2.4.2 Etch Method 2: Results

This etch procedure utilized an isotropic silicon etch to first form microneedle tips during and an anisotropic etch to define the microneedle heights in the subsequent step. The isotropic etch removes silicon equally in all directions resulting in a conical tip profile that is slightly curved. The light microscopy images show the results of the isotropic etch. The undercut photoresist can be clearly seen as the microneedle tip is defined. Figure 5-10 shows an SEM of the final microneedle structures.

5.2.4.3 Comparison of Etch Techniques

Due to the dependence on poorly understood photoresist etching, etch method 2 is the preferred method to form microneedles. Etch Method 1 relies on precise timing of photoresist etching that can vary depending on the uniformity of film thickness, effective area to be etched, and health of the tool. Furthermore, the etch depth is limited by photoresist thickness which is limited to the spin speed of the PR Spinner. In addition, the depletion of the photoresist leads to micromasking issues that can prevent metallization processing in future steps. Using a photoresist with a thinner profile may circumvent these issues; however, the etch rate of the photoresist must first be

characterized. Etch method 2 is superior because the isotropic etch is standardized enabling easy control of the etch depth.

Unsharpened microneedles were used to test the electroplating process. Figure 5-11 is an image of the electroplated micro-pillars. Conformal coating of the structures was achieved; however, due to poor transfer of the electroplating photoresist mask, features are distorted. Because the microneedle structures are patterned in a trench, contact with the photomask is only made with the tips of the needles. This results in a proximity exposure method which increases the influence of diffranction, causing the photopattern transfer to increase in size. Future masks should be designed to address this gap.

5.3   Planar Electrodes for Tumor Spheroid Impedance Monitoring

Gold planar electrode arrays were designed with electrode widths of 30, 40, and 50 μm for sensitivity experiments. Electrodes were configured in a linear array of four electrodes and progressively spaced in iterations identical to the microneedle electrodes. Planar electrodes were used to investigate the influence on electrode spacing on measurement sensitivity and attempt to make multi-spacial measurements of tumor spheroids. Planar electrodes were fabricated on glass substrates using a standard lift-off procedure described in section 5.3.1.

5.3.1 Planar Electrode Fabrication

The procedure outlined in figure 5-12 (a)-(d) was used to fabricate the planar electrodes. Four-inch glass wafers or 1" x 3" microscope slides were first solvent cleaned with acetone, methanol and isopropyl alcohol and then dried using nitrogen gas. A dehydration bake was performed at 150°C to remove all traces of water.

3000PY photoresist was patterned onto samples. Photoresist was spun at 3000rpm for 30 seconds. The wafer was then soft-baked on a hotplate for 1 minute at 150°C. A Karl Suss mask aligner was used to expose wafers to UV light at 25 watts for 23 seconds. Samples were then baked on a hotplate for 1minute at 110ºC post-exposure. Features were then developed in RD6 (Futurrex) photoresist developer for 20 seconds. Samples were then rinsed in IPA and dried with nitrogen gas prior to metallization.

Thermal evaporation was used to form electrodes on the surface of glass samples. A 20 nm layer of chromium was first evaporated onto the surface of the glass to improve gold adhesion. Next, a 150 nm layer of gold was evaporated onto the surface. After being fully metalized, samples were placed in acetone to remove all photoresist. Cr/Au attached to the photoresist was removed, leaving patterned electrode arrays (seen in figure 5-12(e)).

5.3.2 Microfluidic Design and Fabrication

In order to position tumor samples onto the electrodes and measure the impedance of fluid samples, microfluidic channels were designed to be aligned and bonded directly over the electrodes. Figure 5-13 shows the dimensions of the microfluidic channel attached to the electrodes. A simple flow-through channel was designed with circular inlet and outlets measuring 2mm to interface with 23G Tygon tubing. The inlet channel width was 350 µm to easily accommodate the flow of tumor spheroids (250 µm). A simple barrier and dual bypass channels are located just beyond the electrodes to allow spheroids to be positioned directly on the electrodes. Bypass channels measure ~50 µm in width to allow the flow of medium and fluid samples but

restrict the flow of larger solid tumor masses. The outlet portion of the channel measures 500 μm.

Channel molds were fabricated using standard lithography techniques. First, 3 inch silicon wafers were solvent cleaned with acetone and IPA then dried with nitrogen gas. Wafers were dehydrated on a hotplate at 150ºC for 10 minutes. SU-8 2150 photoresist was first spun at 500rpm for 5 seconds then at 1750rpm for 30 seconds to achieve a thickness of 350 μm. A two step soft bake process was performed to purge all solvents from the photoresist. The wafer was baked at 65ºC for 8 minutes and then 95ºC for 80 minutes. UV exposure was performed using a Karl Suss MA-56 for 18 seconds at 25mW. Next, a post exposure bake was performed at 65ºC for 5 minutes and 95ºC for 25 minutes. Finally, the SU-8 mold was developed in SU-8 developer (Microchem) for 25 minutes and plasma cleaned using O_2 plasma.

Microchannels were molded from Poly-dimethyl-siloxane (PDMS) via soft lithography. A 1:10 mixture of PDMS hardener and prepolymer were mixed together with a stirring stick for 5 minutes and then degassed in a vacuum oven. Mixed PDMS was then poured over the SU-8 mold and allowed to cure overnight. After 24 hour PDMS channels were removed from the mold, diced, and irreversibly bonded to electrode chips via plasma bonding. SU-8 5 photoresist was applied via syringe to leakproof microchanels and hardbaked at 200ºC for 10 minutes. A 1.5mm biopsy punch was used to access channels and connected to 23G Tygon tubing. A syringe was used to flow in measurement samples. Figure 5-14 shows the completed microfluidic chip with PDMS microchannels bonded to numbered electrodes.

5.3.3 Impedance Measurement Set-up

50 μm microelectrode chips were used to analyze the effect of electrode spacing on impedance measurement sensitivity. Impedance measurements were recorded with a 4294A Impedance Analyzer. DCP-100 DC probes (Cascade Microtech) connected to micromanipulators were used to make contact with electrode contact pads. A 10mV signal was applied between two electrodes over a frequency range of 100Hz to 1MHz. 1X4 electrode arrays were used to investigate the effect of electrode distance on sensitivity. Impedance measurements were recorded over distances of 50 μm (1-2), 150 μm (1-3), and 250 μm (1-4). Initially, baseline measurements were recorded Dulbecco's Modified Eagle Medium (DMEM) at room temperature. The measured conductivity of DMEM was found to be 10mS/cm^2, which corresponded well with previously reported conductivity values [116]. To ensure electrode sensitivity to conductivity, the impedance of KCL standard conductivity solution at room temperature was also recorded. The conductivity of KCL solution was measured to be 100mS/cm^2.

5.3.4 Hs578T Spheroid Culture

Following initial characterization of the device, impedance measurements were performed on tumor spheroids. Hs578T epithelial breast cancer cells were cultured using standard protocol in Dulbecco's modified eagle medium (DMEM) with 10% Fetal Bovine Serum (FBS) and incubated at 37°C and 10% CO_2. Upon reaching 75% confluence, cells were subsequently subcultured at a ratio of 1:8 or harvested using a 25% trypsin/EDTA solution. Cells were then counted using a hemocytometer and reserved for spheroid formation. In order to form tumor spheroids of 250 μm, 9.6e5 cells suspended in DMEM were pipetted onto, Aggrewell plates, a PDMS cellular

micromold located on a 24-well plate (StemCell Technologies). Cells were then centrifuged at 100xg for 3 minutes to evenly distribute cells into 400 μm microcavities. Cells were then incubated for 24 hours to yield tumor spheroids.

5.3.5 Results and Discussion

5.3.5.1 Verification of Electrode Sensitivity

To verify electrode sensitivity, impedance measurements were recorded for standard potassium chloride solution and DMEM culture medium with conductivities of 100 and 10 mS/cm, respectively. Results of the measured impedances are shown in figure 5-15.

For an electrolyte solution in contact with a metal conductor, a basic R_s–C_{dl} circuit can be used to accurately describe the system. The double layer capacitance, C_{dl}, defines the high impedance at lower frequencies and the slope of the curve. This capacitance is well characterized for gold electrodes and is known to range from 10-20 μF/cm^2 (14.25 μF/cm^2 in [121]). By measuring the magnitude of the impedance, Z, at a known frequency, f, on that slope we can solve for the measured capacitance, c, using the following equation:

$$|Z| = \frac{1}{2\pi f c} \rightarrow c = \frac{1}{2\pi f |Z|} (\mu F)$$

We then can use this measured capacitance value to estimate the value of the double layer capacitance, C_{dl} by dividing the measured value by the area of the electrodes as follows:

$$C_{dl} = \frac{c}{Area} \left(\frac{\mu F}{cm^2} \right)$$

It can be seen that only small changes in the impedance at lower frequencies occur because only the conductivity of the solution is changed.

At higher frequencies (> 1e5Hz), the double layer capacitance no longer dominates the system for the medium because of the high impedance of the medium compared to the capacitive component. The conductivity of the solution can be used to calculate the solution resistance parameter in the system. Because the semi-circular electrode immersed in solution is similar to the rotating disk electrode, the solution resistance is easily calculated using the following equation:

$$R_s = 2\frac{\rho}{4r} = \frac{\rho}{2r},$$

which is taken from Newman's analysis on the spinning disk electrode [122]. Because there are two electrodes in the solution the resistance is increased by a factor of two. When calculating the theoretical resistance, the measured conductivities are first converted to the corresponding resistivity and then plugged into the resistance equation. The results of calculated resistance and capacitance values are shown in table 5-2(a) and measured values for each electrode configuration are shown in table 5-2(b). Measured solution resistance values correspond to the impedance value at frequencies = 9.55e6 Hz.

It can be seen that roughly an order of magnitude drop in Rs occurs when switching from KCl to DMEM, which corresponds well with the known conductivity change of the electrolyte. This shows that the impedance change is proportional to electrolyte conductivity as expected. However, it can also be seen that in KCl solution as the spacing of electrodes increases the solution resistance drops while the capacitance increases. This is thought to be due to the high conductivity of the

69

electrolytic solution and an increase of available charge carriers in the larger gap between electrodes. This is supported by the fact that the resistance increases and space increases in the DMEM solution.

5.3.5.2 Effect of Electrode Spacing

To assess the effect of electrode spacing on measurement sensitivity, the impedance change due to switching conductive solutions from KCl to DMEM was calculated for each electrode configuration. The results from these calculations can be seen in figure 5-16. At frequencies < 1e5 Hz, little to no change is seen for spacings of 50 and 150 µm. This is due to C_{dl} dominating the measured impedance. However, at higher frequencies it can be seen that the % change increases for every electrode spacing, most notably at the larger spacings. Furthermore, it can be seen that as electrode spacing increases, the % impedance change also increases. This is illustrated by the maximum impedance increase being seen at the 1-4 electrode configuration (250 µm).

Next, spheroidal impedance measurements were recorded. Bode plots illustrating the impedance of Hs578T spheroids are shown in figure 5-17a. From these images it can be seen that increasing the space between electrodes causes the measured impedance of the spheroid to increase. When the percent change is calculated according to recorded medium baselines (figure 5-15), the maximum calculated percent change is at 250 µm. A 60% increase in the impedance is seen in comparison to medium baselines.

From figure 5-17b, it can be seen that the greatest increase in impedance is seen at higher frequencies and reaches a plateau around 1e6 Hz. This reveals that the

mechanism causing the impedance change is the tumor spheroid physically displacing the conductive medium in the microfluidic chamber. Because the electrodes are not fully insulated from the medium, current flows through both the spheroid and medium. However, when compared to figure 5-16 (denoting the impedance change solely on medium conductivity) the impedance change begins to increase closer to 30 kHz. This indicates that the cause of the impedance change from 30 kHz to 1e6 Hz is in response to the presence of the tumor spheroid as expected from previous studies of the so-called 'beta' region where impedance of biological tissue is dominated by cellular membrane presence.

5.4   Conclusion

This work presents the simulation, design and attempt at fabricating 3D microneedle electrodes for multi-spatial impedance measurements of tumor spheroids. A simple two step anisotropic/isotropic etching procedure was developed for fabricating sharpened solid silicon microneedles with submicron tips that improved upon previously developed processes relying on photoresist depletion. Attempts were made to metalize unsharpened 'nanorods'. While conformal coating of the microneedle was achieved, resolution limitations distorted electrode tracks and contacts. In addition, adhesion problems persisted due to micromasking issues and equipment failures. Due to equipment malfunctions microneedle electrodes were not used in impedance analysis.

Microfluidic planar electrodes were designed to position and monitor the impedance of tumor spheroids in real-time. Microfluidic channels measured 350 μm in width and height and were capable of positioning tumor spheroids directly over electrodes via continuous fluid flow. Impedance measurements were first performed on

fabricated planar arrays of electrodes to assess the impact of electrode spacing on the measured impedance. The function of the fabricated electrodes was verified by comparing the measured impedance curve to theoretical capacitance and resistance values taken from the literature. Finally, impedance measurements of Hs578T were recorded and compared to baselines of pure culture medium. The resulting impedance changes were associated with both medium displacement (f > 1e 6Hz) and tumor spheroid impedance (30 kHz < f < 1e6 Hz). This work lays the foundation for a system that is capable of continuously perfusing a spheroid with culture medium and maintaining viability for an extended period of time while simultaneously monitoring the spheroidal impedance.

Furthermore, it was established that impedance measurements made with planar electrodes were adequate for monitoring the spheroidal impedance and the use of an electrode array can increase the spatial resolution of currently available tumor impedance monitoring systems [1, 4, 60]. The automation of this system will yield many important comparison studies between the behavior of monolayer cultures and spheroidal models when exposed to a multitude of stimulants including: nanoparticles, future drug candidates, and potentially toxic materials.

Table 5-1 Etch profiles for continuous etching of silicon and photoresist.

Etch Time	Trench Depth (μm)	Si Etched (μm)	PR Etched (μm)
0	6.51	0	0
10	84.7	82.6	2.1
18	145.5	141.72	3.78
27	161.6	155.93	5.67
32	*	-	-

Table 5-2 (a) Calculated and (b) measured values of resistance and capacitance of KCL and DMEM.

	C_{dl}	R_s
KCL (theory)	10-20	2k
DMEM (theory)	10-20	20k

	C_{dl}	R_s
KCL		
1-2	16.6	1.67k
1-3	21.5	780
1-4	57.5	540
DMEM		
1-2	16.8	7.64k
1-3	22.7	8.1k
1-4	24.5	10k
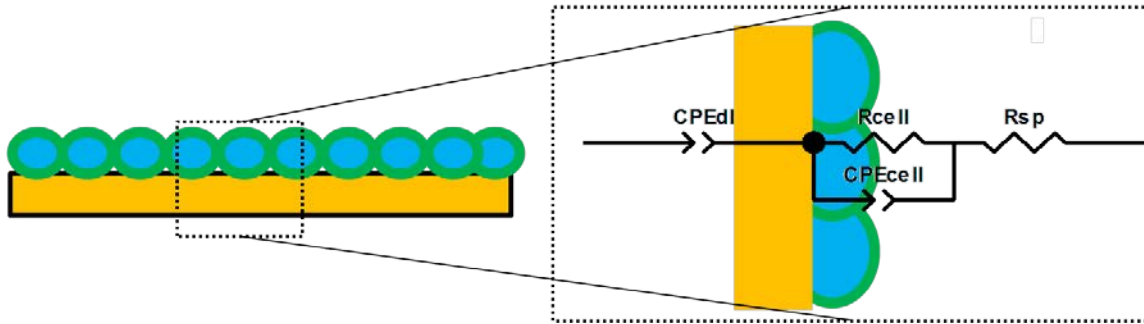
Figure 5-1 Equivalent circuit model for electrode covered with cells.
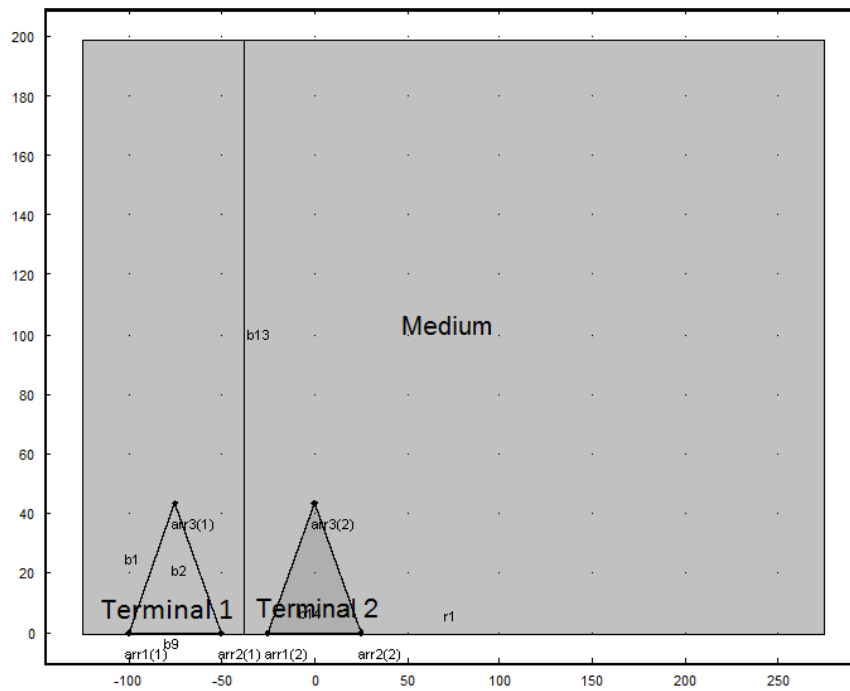
Figure 5-2 Comsol simulation setup for 50μm microneedle electrodes.
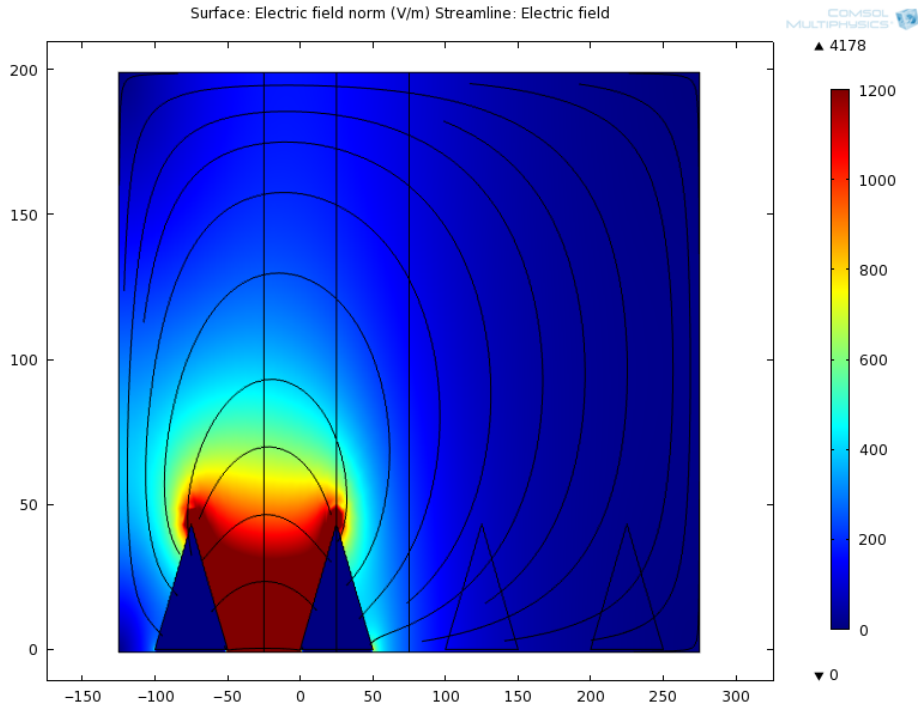
Figure 5-3 Normalized electric field of microneedle electrodes spaced 50 µm apart.
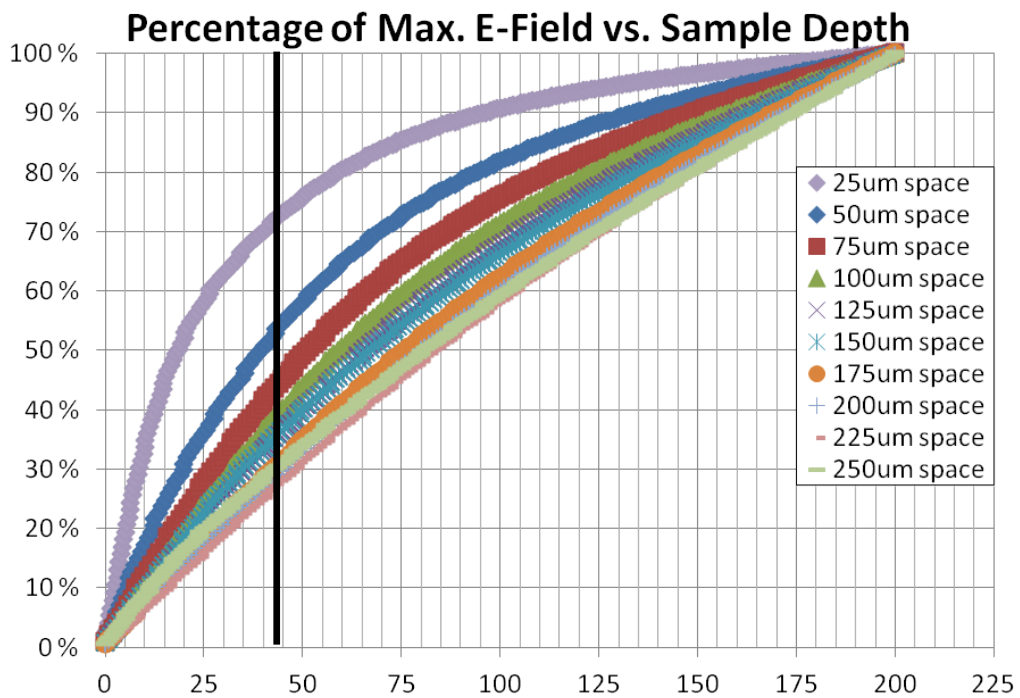
Figure 5-4 Calculated percentage of maximum electric field vs. penetration depth (distance from base of triangles).
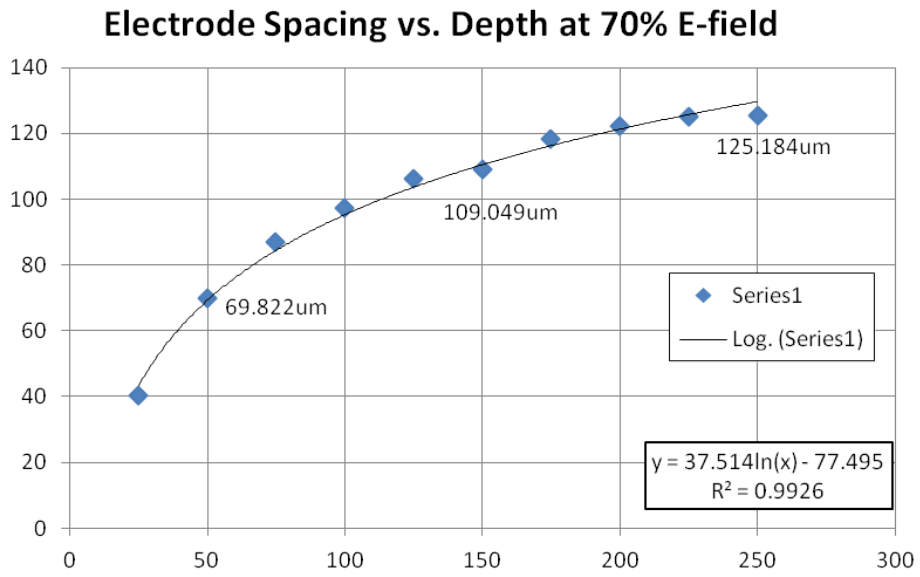
Electrode Spacing vs. Depth at 70% E-field

125.184um

109.049um

Series1

Log. (Series1)

69.822um

$y = 37.514\ln(x) - 77.495$
$R^2 = 0.9926$

Figure 5-5 Distance where electrode penetration reaches 70% of maximum vs. spacing between electrodes.
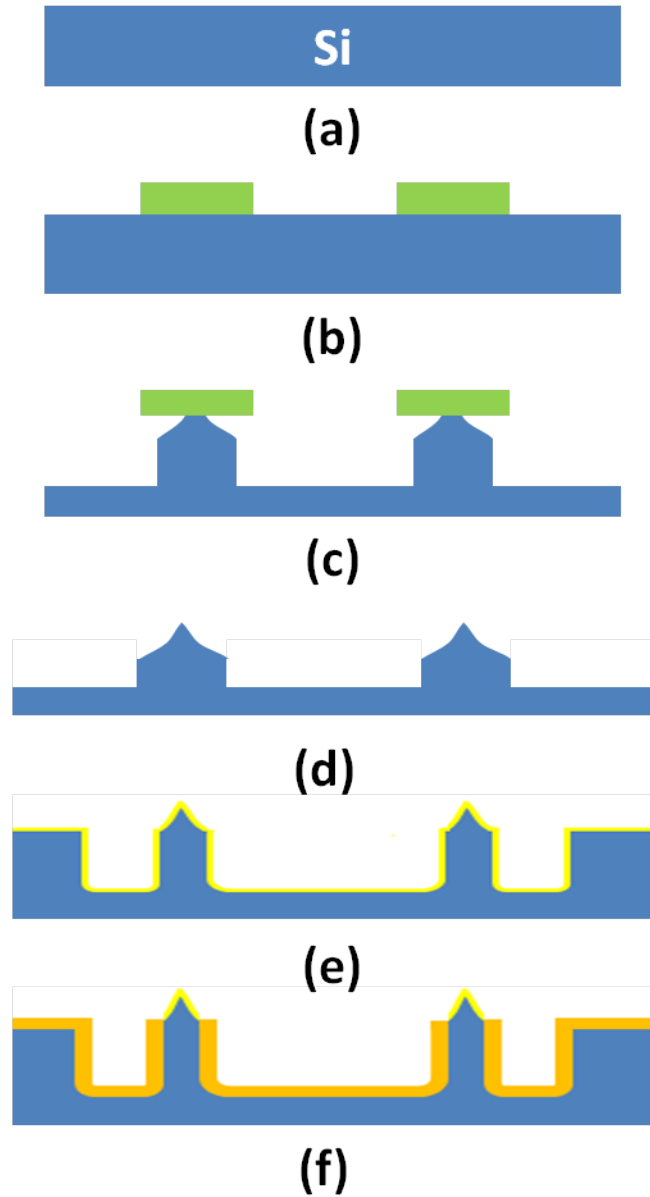
Figure 5-6 Microneedle process flow. (a) Standard silicon wafers solvent cleaned, (b) patterned with AZ4620 photoresist, (c) etched using deep reactive ion etching (DRIE); (d) photoresist removed and sputter coated with nickel; (e) gold deposited onto nickel layer; (f) gold passivated with SU-8 photoresist.
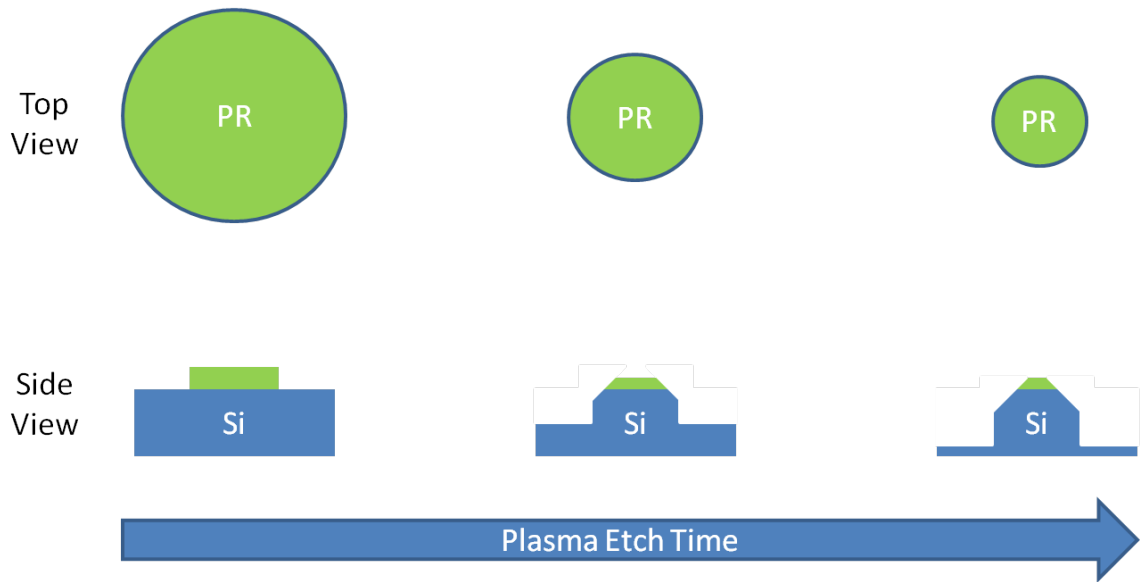
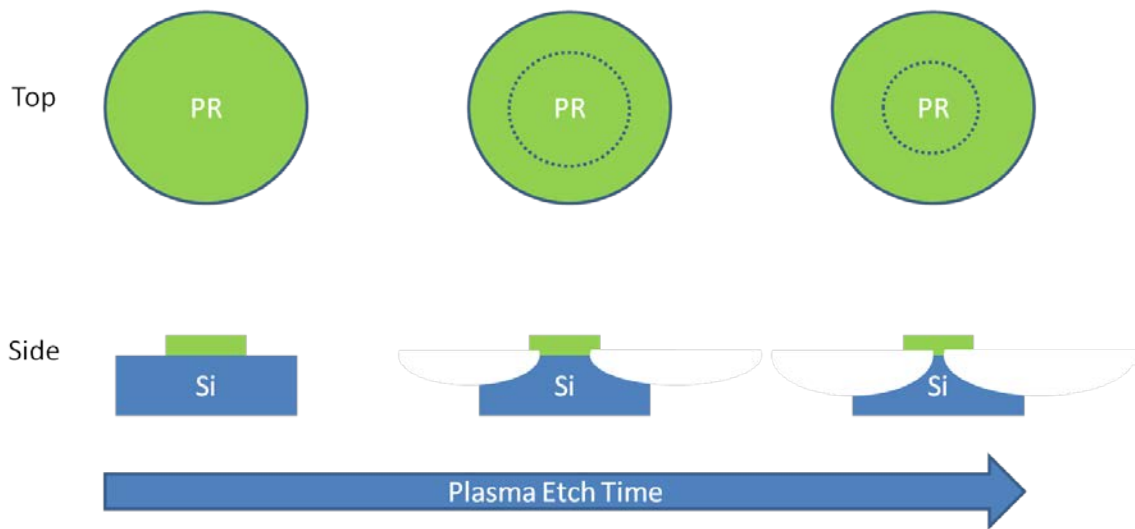Figure 5-7 DRIE etch method 1: continuous anisotropic etch.

Figure 5-8 DRIE etch method 2: two step isotropic/anisotropic etch.
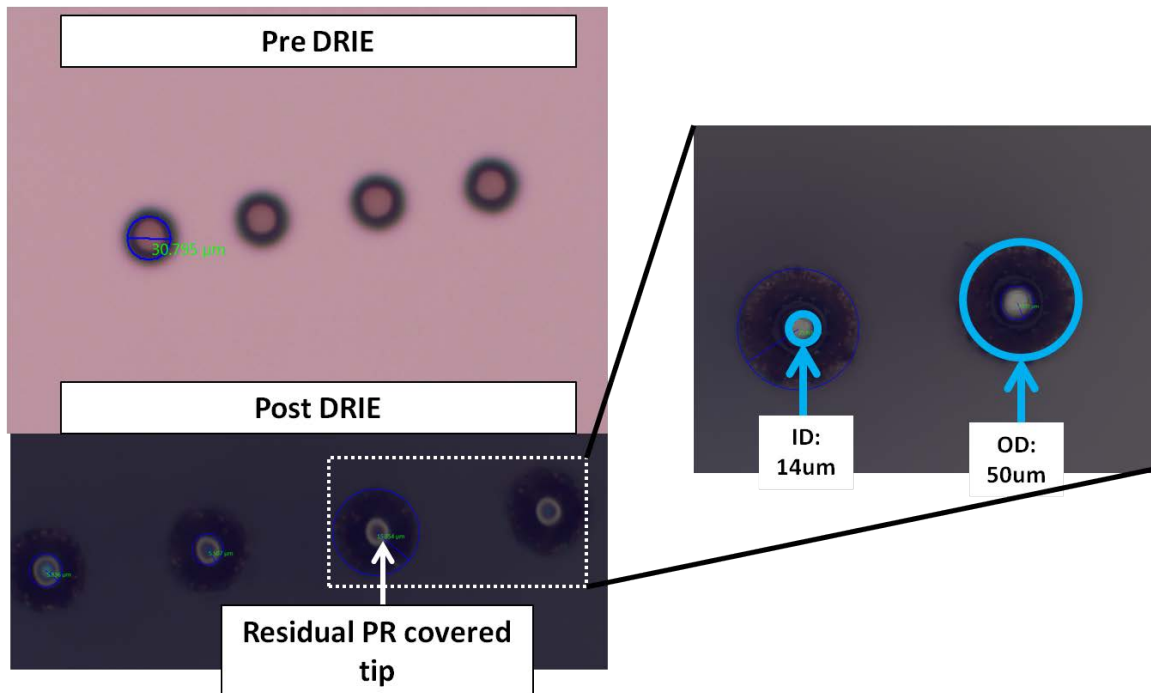
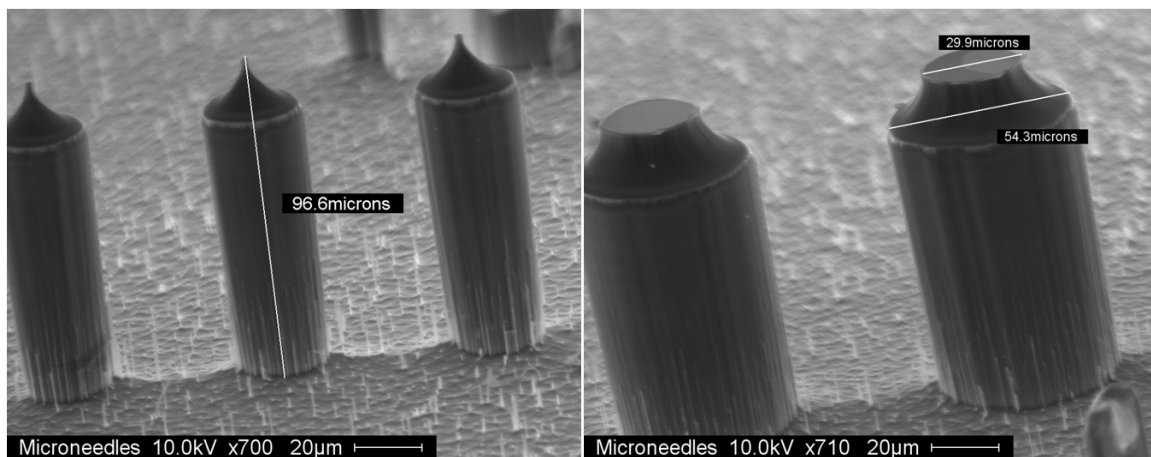Figure 5-9 Resultant silicon microneedles after continuous silicon etch.

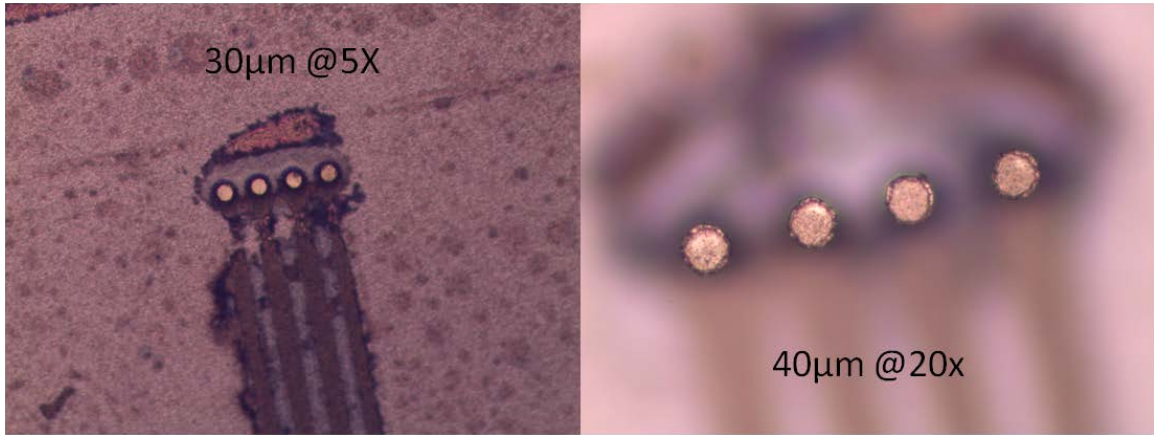Figure 5-10 SEM image of silicon microneedles after two step anisotropic/isotropic etch.

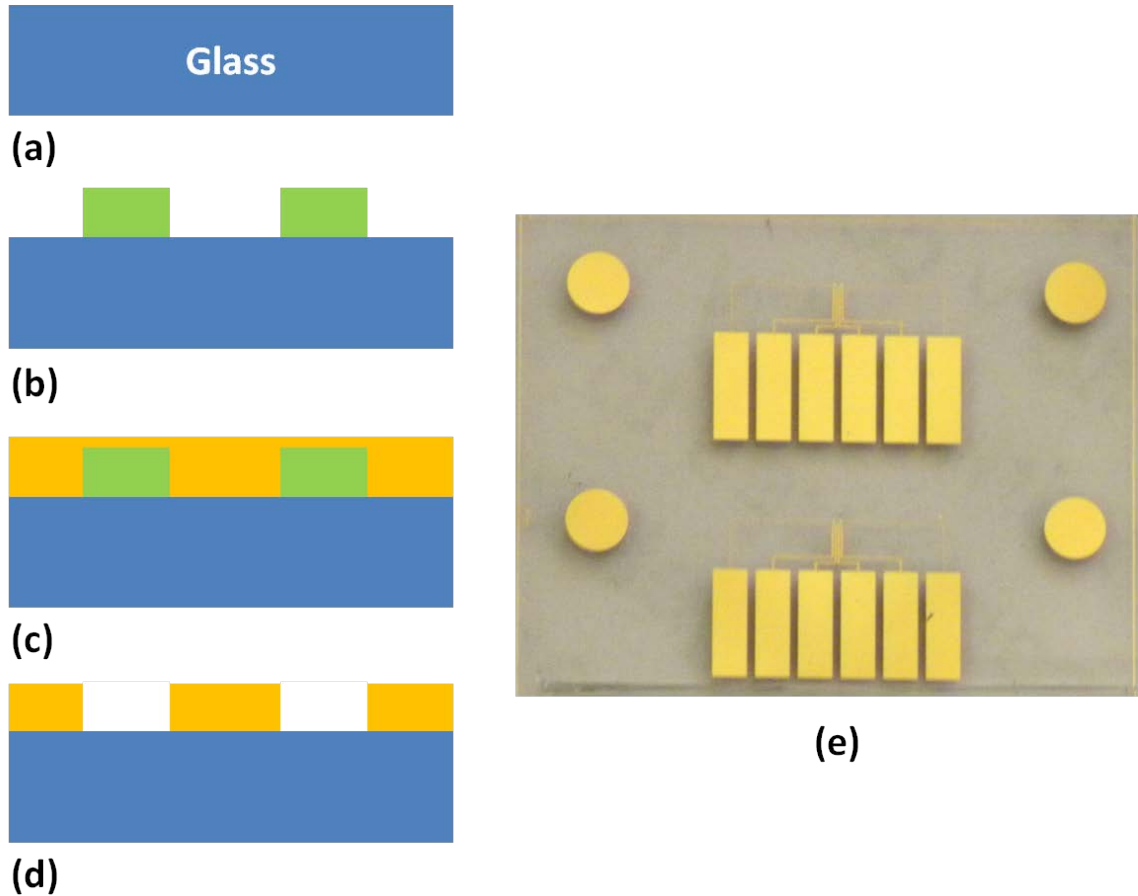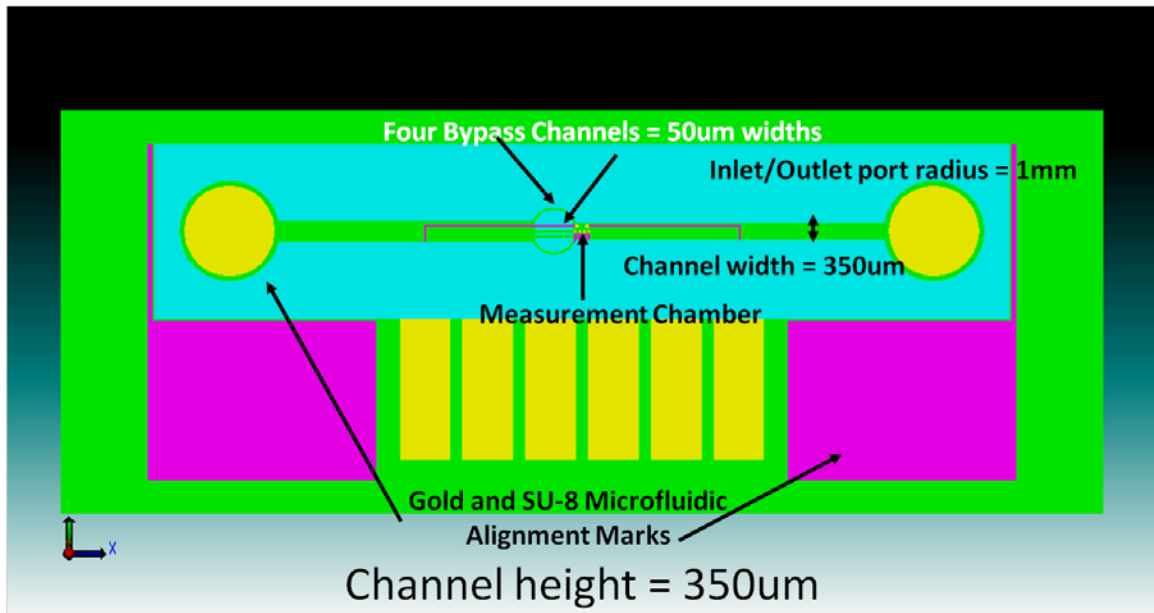Figure 5-11 Micropillars coated with nickel gold layer.

Figure 5-12 Process flow for planar electrodes. (a) 4" glass wafers solvent cleaned; (b) patterned with 3000PY photoresist; (c) coated with chrome and gold; (d) dipped in acetone for liftoff; (e) resulting gold electrodes.

Inlet volume = $\pi*(1000\ \mu m)^2*2*350\ \mu m = 2198000000\ \mu m^3$
$350um*350um*17000\ \mu m = 2082500000\ \mu m^3$
Total Volume ~= $4280500000\mu m^3 = 4280.05$ nanoliters = 4.28005 microliters

Figure 5-13 Microfluidic channel design shown on electrodes.
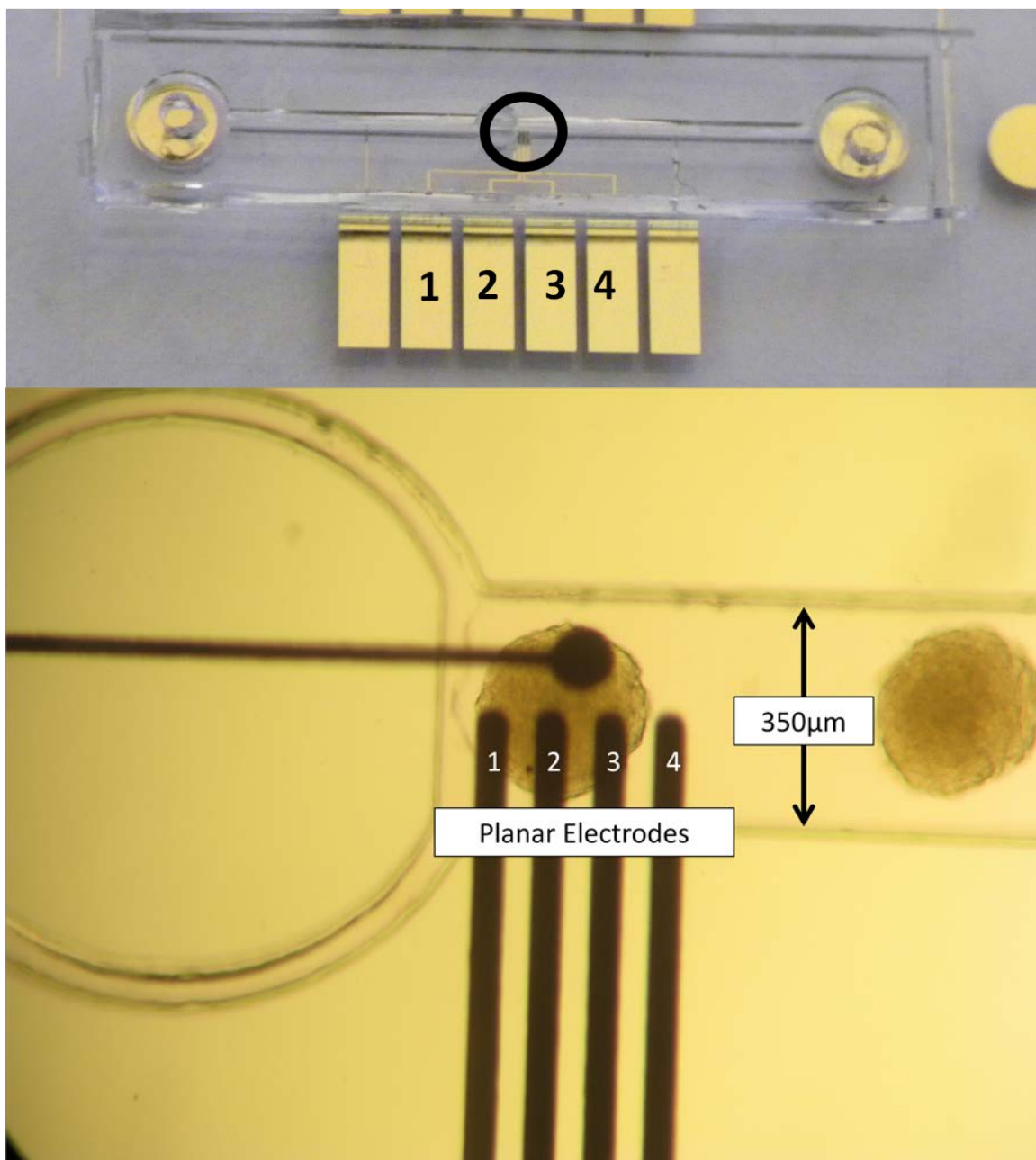
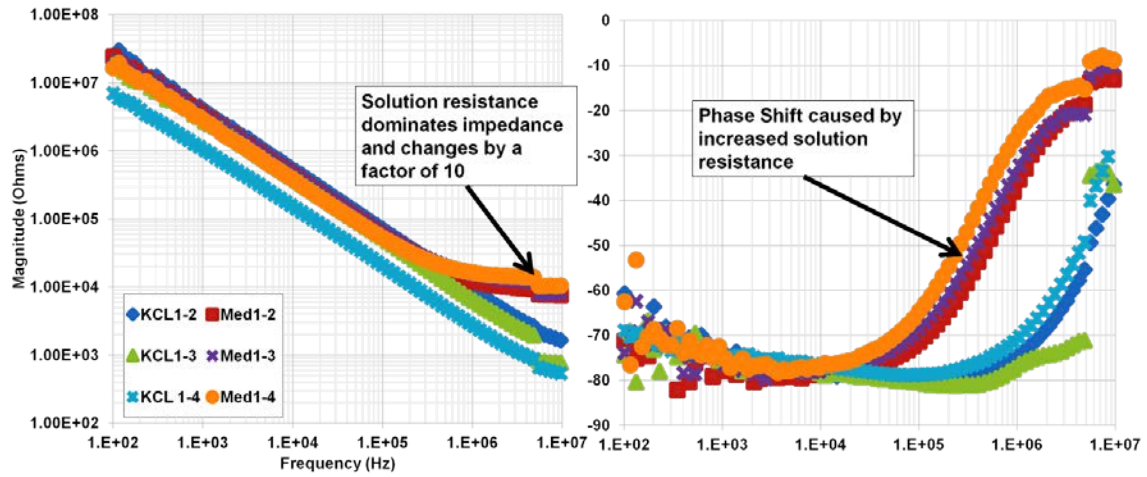Figure 5-14 Top view of electrodes with PDMS microfluidic channel attached.

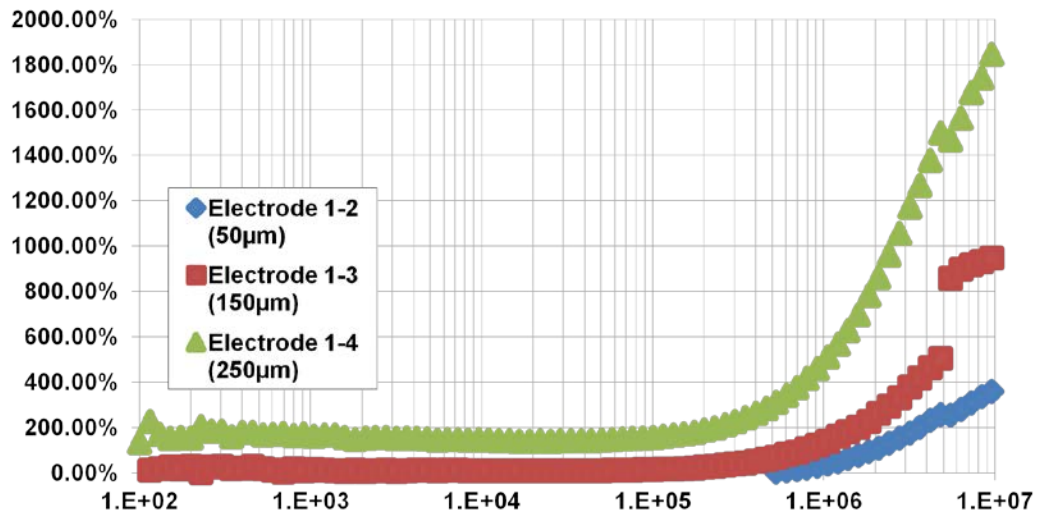Figure 5-15 Bode plots of measured impedance of KCl solution and DMEM.

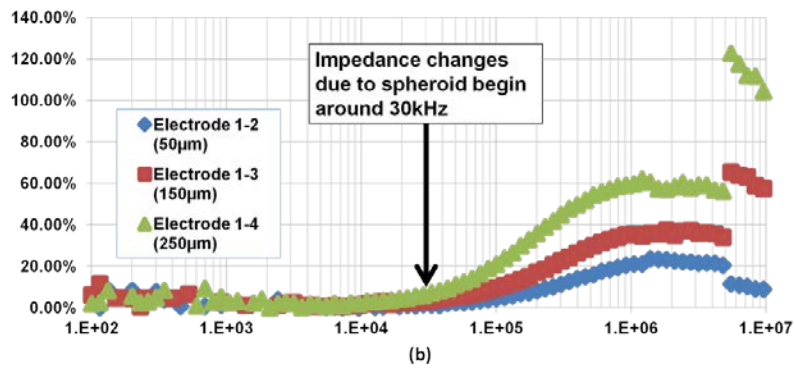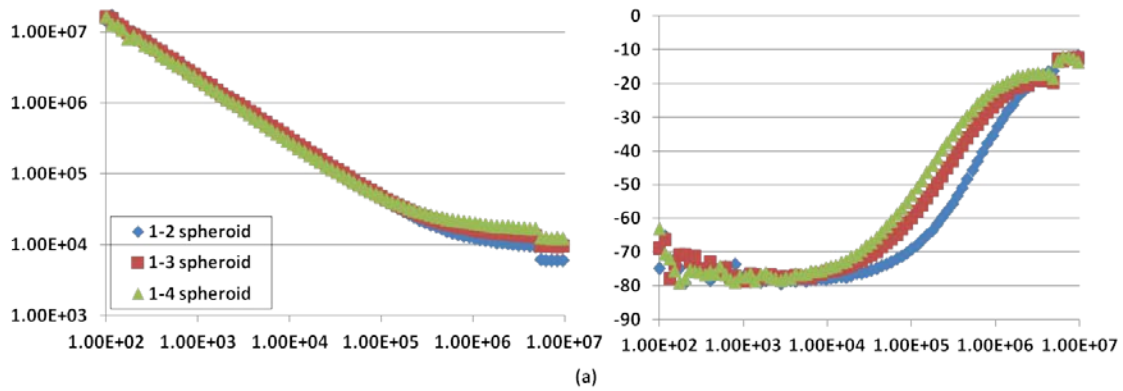Figure 5-16 Normalized impedance change (KCl/DMEM).

Figure 5-17 (a) Bode plot of impedance measurements of tumor spheroids. (b) Normalized impedance change of tumor spheroids compared to medium baselines (figure 5-15).

Chapter 6: Design and Characterization of Micro-pH Electrodes for Extracellular Environmental Monitoring

6.1   Introduction

Despite improvements in real-time impedance analysis for cellular cultures, to date, impedance measurements of tumor spheroids alone are inadequate for assessing the pathology associated with morphological changes in the models. In order to more accurately assess the underlying mechanisms causing cellular stressors/changes, other biosensors are a suitable method for monitor the extracellular environment of the tumoroid culture. Specifically, pH sensing can be utilized to assess metabolic changes in a cellular by monitoring the extracellular acidification rate (ECAR)[123]. Monitoring these changes in metabolic activity can yield useful information about the underlying pathology. Combining impedance-based sensors with optical [124] and semiconductor [125] pH detectors have been explored by several authors [126-128] and have even been corporate into multi-well plate assays [129, 130]; however, they have failed to incorporate the increased accuracy of tumor spheroid models.

In the prior chapter, a microfluidic device was designed to trap tumor spheroidsf and continuously monitor their impedance changes. In this chapter, a micro-pH sensor has been designed for monitoring real-time changes in extracellular pH on the same microfluidic chip. The μ-scale pH electrode is located adjacent to the impedance measuring electrodes so that parallel measurements can be made in real-time (future work). First, a commercial glass pH electrode was used to compare the ECAR of planar

cellular cultures to the ECAR of tumor spheroids. Next, macroscale pH sensitive electrodes were fabricated and tested as a proof of concept. Calibration procedures were developed to establish the sensitivity curve of fabricated macro-pH electrodes. Finally, micro-pH electrodes were fabricated using standard lithography techniques and characterization was performed.

6.2   Theory

6.2.1 Extracellular pH Theory

Within an aqueous solution, the water molecules in the solution spontaneously decay and combine via the following reaction:

$$H_2O \leftrightarrow H^+ + OH^-.$$
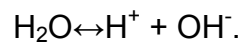
When the reactants and products are present in equal amounts, the solution is said to be in equilibrium or neutral. A solution in which there is an excess of H^+ ions is termed acidic, whereas a solution with excess OH^- ions is termed basic (alkaline). The level of acidity or alkalinity is called the pH. PH is a measure of the acidity of an aqueous solution and can be formally defined as the negative logarithm of the concentration of $[H^+]$ ions in the solution as shown below:

$$pH = -\log[H^+].$$

The pH scale is confined from 0 to 14, where a pH of 7 represents a neutral solution. In addition, the logarithmic scale of pH denotes that a pH change of 1 means a 100-fold increase/decrease in the acidity of the solution.

As cells live and consume nutrients, waste products are released into the outlying culture medium as a byproduct of cellular metabolism. Primarily, cellular respiration causes nutrients (glucose and O_2) absorbed by the cell to be broken down

via glycolysis. These nutrients are broken down into waste products (CO_2, water and energy in the form of ATP), which are the chief products of respiration. However, because hydrogen ions are not directly produced as a product of cellular respiration the pH of the solution relies on the production of CO_2.

Excess CO_2 in the atmosphere and the elevated temperature of the culture medium can cause the solution to be acidic:

$$H_2O + CO_2 \leftrightarrow H_2CO_3 \leftrightarrow H^+ + HCO_3.$$

For this reason and because mammalian cellular cultures proliferate most effectively in a small pH range (7.2–7.4) most culture medium contains additional sodium bicarbonate to lower the pH of the system by producing extra bicarbonate via:.

$$NaHCO_3 \leftrightarrow Na^+ + CO_3$$

The production of additional CO_2 by the cells being cultured causes a slow accumulation of CO_2 in the medium overtime. This accumulation of CO_2 in the culture medium drives down the extracellular pH overtime, acidifying the medium. Using extracellular pH sensors, one can monitor the rate of cellular respiration [131].

6.2.2 Extracellular pH Sensing

6.2.2.1 Traditional Approaches

Several methodologies have been used to monitor the pH of cellular cultures overtime. The most common method of monitoring it is via phenol red. In addition to nutrients and pH buffer, most commercial culture mediums include phenol red as a pH indicator. Phenol red crystals are dissolved into the medium solution and appear yellow as the medium becomes more acidic (pH less than 7.0) and pink as it becomes more basic (pH greater than 7.0). It is important to note that phenol red is a qualitative

measure of pH and is not useful when calculating the extracellular acidification rate (ECAR) or monitoring the pH quantitatively.

Another traditional means of recording the extracellular pH are glass pH electrodes. Commercial glass pH electrodes are typically constructed from 3 main components: a glass container filled with buffer solution (either liquid or gel) of a constant pH, a membrane that is semi-permeable to H^+ ions, and a conductive Ag/AgCl electrode (figure 6-1). pH is then calculated by measuring the open circuit potential (OCP) between the pH electrode and a reference electrode immersed in the measurement solution using a highly sensitive voltmeter. When the pH electrode comes into contact with the solution of interest, a "gel region" is formed on the surface of the membrane and only H^+ ions are allowed to diffuse across the gel layer and build up in the gel region without crossing into the glass fully and contaminating the buffer solution.

Because the AgCl wire is immersed in the buffer solution within the glass membrane, the wire-buffer system maintains a standard electrode potential E_0. A measurable potential difference then builds up in the gel region and the combined electrode potential can be defined by the Nernst equation:

$$E_{electrode} = E_0 - \frac{2.303 * R * T}{F * z} * \log a_{H^+}$$

where, E_0 is the standard electrode potential, R is the general gas count, T is the temperature in Kelvin, F is faraday's constant, z is the ionic charge, and a_{H^+} is the concentration of hydrogen ions. Scaling issues make the traditional glass pH electrode impractical for monitoring small areas surrounding tumor spheroids.

6.2.2.2 Light-Addressable Potentiometric Sensors (LAPS)

Other pH measuring techniques utilize the unique semiconductor properties of silicon. Light-Addressable Potentiometric sensors are a type of photochemical sensor that leverages the global or local changes induced in a silicon-insulator interface to detect pH. A schematic of a typical LAPS device is shown in figure 6-2. The sensor consists of a piece of doped silicon with an insulating pH sensitive thin film (silicon nitride in the example) deposited on the top side of the silicon. The topside of the sensor is enclosed so that cells can be cultured directly onto the top of the insulating layer. Conductive leads are connected to the doped Si and immersed into the cell culture medium and a bias voltage is then applied to the system. A laser or LED is then used to illuminate the backside of the silicon.

When the silicon is forward biased no charge transfer is developed in the silicon; however, when reverse biased, a depletion layer develops at the silicon-insulator interface. This results in the generation of photocurrents when the laser/led is used to excite the silicon surface. The resulting photocurrent is then measured between a reference electrode and the contact made with the silicon[132]. Because the magnitude of this photocurrent is a function of the combined interfacial potentials and the interfacial potential between the culture medium and the insulator is dependent on pH the induced photocurrent is proportional to the pH of the solution.

LAPS sensors are highly desired due to their simplicity of fabrication and functionality. One can also employ special coatings onto the insulator surface to monitor other metabolically relevant analytes such as O_2 [133] and glucose [134]. In addition, scanning a laser beam over the surface of LAPS sensors produces resolution

down to the microscale, allowing the resolution of extracellular pH of a single cell as well as pH gradients. However, due to the planar composition of the LAPS sensor, resolving the pH in 3D tissues is not practical.

6.2.2.3 Ion-Selective Field Effect Transistors (ISFETs)

Another methodology used to monitor extracellular pH is the ion-selective field effect transistor (ISFET). Based on the metallic-oxide-semiconductor FET (MOSFET) device, the ISFET was one of the first silicon-based pH sensors [135]. Operation of the ISFET is similar to that of a traditional MOSFET [29] where a small voltage is applied to the gate and the current flowing from source to drain is determined by the potential flowing through the gate (figure 6-3). The key difference between the MOSFET and the ISFET is at the gate. Within a typical MOSFET, ohmic contacts are connected to the doped silicon of the source and drain regions and an insulating silicon oxide layer is deposited between them to form the gate. When a bias voltage is applied between the gate oxide and the source that satisfies a known threshold, a depletion layer is formed between the source and drain and current is allowed to pass.

In the ISFET, the gate oxide is replaced with an ion-sensitive material and a reference electrode immersed in a solution of interest. It is important to note that contact between the measured solution and the source and drain contacts will cause electrical shorting. For this reason the rest of the surfaces are kept from making contact with the analyte. To make an ISFET for pH detection, a pH sensitive metal oxide or nitride sensing layer is commonly used at the gate. The performance of the pH sensor is dependent on the characteristics of the gate material.

The Nernstian sensitivity (mV/pH), drift (mV/time), sensing area, and range of pH sensitivity all contribute to the performance of the sensor. Characteristics of several tested gate materials are listed in [136, 137]. pH-sensitive ISFETs have been used successfully to monitor the pH of monolayer cell cultures [13]. However, the need for a large reference electrode makes the ISFET difficult to implement seamlessly into microfluidic systems. Small-scale reference FETs (REFET) have been utilized to address this shortcoming, but shrinking the size of ISFET packages for the measurement of nanoliter volumes remains a challenge due to an increase in signal to noise ratio typical of FET devices[138].

6.2.2.4 Thin Film pH-sensitive Electrodes

The increasing application of microfluidics for cellular analysis and chemical sensing demands new requirements for chemical sensors. Microfluidic designs that can manipulate single cells require handling of volumes on the nanoliter scale. Another pH sensor useful for this application is the thin film pH-sensitive electrode. Comprised of a simple pH sensitive insulator deposited onto a conductive electrode, thin film pH electrodes are useful due to their easy incorporation into on-chip microfluidic designs. Because they are simply planar films deposited onto silicon or glass substrates, attaching PDMS- based microfluidics composed or other materials becomes as simple as aligning the channels to the electrodes and bonding the material to the substrate.

A typical thin film pH electrode sensing system is composed of a conducting metal, a metal oxide, and a reference electrode (figure 6-4). Electrical contacts are made between the metal oxide and the reference and the open circuit potential (OCP) is measured once the electrodes are immersed in solution. Many metal oxides display

sensitivity to H+ ions when immersed in solution, obeying the following general redox reaction

$$M_x + 2yH^+ + 2ye^- \leftrightarrow xM + yH_2O$$
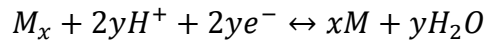
as indicated by [139]. Equilibrium of these reactions are dependent on the concentration of H+ ions in the solution hence, it is pH dependent. The measured OCP is then proportional to the nernstian electrode potential.

Extensive work has been done to characterize the pH sensitivity and drift of various metal oxides, thanks to their extensive use in ISFET devices [137]. One drawback of thin film pH electrodes is the need for an external reference electrode to provide a stable measurement of the OCP. Conventional reference electrodes are much larger than the microfluidic environment. However, alternative have been developed to minimize the size of the reference electrodes. World Precision Instruments has fabricated "Dri-Ref" AgCl reference electrode with diameters as small as 450 microns (WPI), but are still difficult to implement into closed microfluidic systems. Planar thin film reference electrodes made of Ag/AgCl have also been developed but suffer from a short lifetime due to the consumption of the finite supply of chlorine ions in the AgCl layer. Alternative reference electrodes with longer lifespan have been devised using other materials and by encapsulating the AgCl layer [140].

One alternative to a traditional reference electrode is using a "quasi"-reference electrode (QRE) that maintains a stable potential when immersed in a reference solution of known pH. This is ideal for planar sensors that are attached to a microfluidic lab-on-a-chip due to the loss of the bulky external reference electrode. To this end, a functional "differential" micro-electrode has been demonstrated by Ges et al. using

iridium oxide as a sensing layer with and without an external reference electrode[141]. For this reason, thin film metal oxide electrodes were chosen to fabricate a preliminary on chip pH sensor for monitoring the extracellular pH of tumor spheroids.

6.3   Fabrication of Macro-scale pH-sensitive Electrodes

Two pH sensitive thin films were chosen to be evaluated for fabricating microscale pH electrodes on a microfluidic chip for evaluating extracellular pH of tumor spheroids. Zinc oxide and iridium oxide were chosen as candidate thin films for micro-pH electrode construction and testing.

Iridium oxide based sensors have been increasingly investigated for use as a pH sensing film, resulting in various methods of deposition being developed including: electrochemical deposition, sputtering, sol-gel, and thermal preparation of films [142]. Each of these preparation techniques generates films of varying quality and structure, which directly influences the pH sensitivity. Iridium oxide films generated using sol-gels and electrochemical deposition have shown particularly high pH sensitivity [143, 144]. This high sensitivity will be critical in assessing pH changes in the small physiological pH range that cellular cultures maintain (7.0 pH - 8.0 pH).

Zinc oxide has become a material of interest for biosensing and semiconductor applications due to its biocompatibility, stability and band gap. Within the realm of biosensing, so-called nanowires and nanorods composed of zinc oxide have been investigated for monitoring the intracellular pH of single cells and used to measure the pH inside a human adipocyte [145, 146]. Depending on the fabrication technique, zinc oxide nanowires and nanorods have been shown to have varying pH sensitivity ranging from as little as 22 to as great as 51.8 mV/pH, however; to date the pH response of

sputtered zinc oxide thin films has yet to be investigated [147]. This work evaluates the pH sensitivity of zinc oxide and iridium oxide thin films for use in a micro-pH sensor.

6.3.1 Iridium Oxide and Zinc Oxide Electrode Fabrication

Centimeter scale electrodes were fabricated to test the pH response of iridium oxide and zinc oxide thin film coatings patterned on gold electrodes. To begin, a 4" glass wafer was coated with chrome and gold and diced into 1 cm x 3 cm electrodes. Diced electrodes were then separated into two separate batches for processing. The first half of gold electrodes were taken and partially covered with Kapton tape for zinc oxide deposition. These electrodes were then sputter coated with a 100 nm thick zinc oxide layer to form pH sensing electrodes. Thickness was verified using an Alphastep 200 surface profilometer. The Kapton tape was then removed exposing a gold contact for measuring the open circuit potential. Kapton tape was then used to insulate pH sensing layers leaving an approximately 1 cm^2 area. Electrodes were then rinsed with DI water, and dried with nitrogen gas before storage in 10 mL tubes. All fabricated zinc oxide pH electrodes were stored at room temperature.

6.3.2 Iridium Oxide Deposition

The second half of gold electrodes was coated with iridium oxide via anodic electrodeposition. Ges et al. described a solution for electrodepositing iridium oxide consisting of dissolved iridium tetrachloride, hydrogen peroxide, and oxalic acid first devised by Yamanaka in [148]. First, 150 mg of iridium tetrachloride was dissolved into 100 ml of DI water and stirred for 20 minutes with a magnetic stirrer. 1 ml of 30% hydrogen peroxide was added and the solution was stirred for an additional 15 minutes. Next, .5 g of oxalic acid was stirred into the solution for 5 minutes. Anhydrous

potassium carbonate was added to the solution until the pH reached 10.5. The solution was allowed to stabilize at room temperature for 24 hours and then transferred to a dark container and stored for an additional 24 hours in a refrigerator at 4ºC.

Several authors have described various plating procedures for depositing iridium oxide onto gold substrates including galvanostatic, potentiostatic, and voltage pulse techniques. Recently, Elsen et al. concluded that potentiostatic deposition provided the most stable, adhesive films when plating thicker films [143]. A standard 3-electrode cell (Figure 6-5) was used to carry out the electrodeposition. Gold coated electrodes served as the working electrode, a platinum wire was used as the counter electrode, and either a Micro Dri-Ref Ag/AgCl electrode from WPI Instruments or saturated calomel electrode from Gamry Instruments was connected as the reference electrode. Two pulse sequences were applied using a Gamry Ref600 Potentiostat for deposition of iridium oxide thin films.

1) Galvanostatic Technique – A constant current density of 1-1.5mA/cm^2 was applied for a period of 8-10 minutes.

2) Potentiostatic step Technique - A constant voltage of 500 mV was applied between the working and counter electrodes for 10 minutes followed by a constant voltage of 600 mV for 5 minutes.

After deposition wafers were rinsed in DI water and stored in 10 mL tubes prior to testing.

6.3.3 pH Sensitivity Measurements

To evaluate the pH response of fabricated pH electrodes, beaker experiments were performed against pH standards. Open circuit potentials were recorded for buffer

solutions with pH values of 4, 7, and 10 pH units (Fisher Scientific). Either ZnO or IrO electrodes were removed from storage and rinsed with DI water and subsequently dried with nitrogen gas. A simple 2 electrode cell, as seen in figure 6-4, was used to evaluate the pH response of electrodes. Open circuit potentials were recorded using the pH sensitive electrodes as the working electrode and a saturated calomel electrode as the counter electrode. OCP values were recorded for a minimum of 5 minutes until pH values stabilized.

6.4   Micro-pH Electrode

6.4.1 Design

A micro-pH electrode was designed for monitoring extracellular pH in conjunction with real-time impedance measurements made on the previously designed microfluidic chip. A schematic view of the electrode design is shown in figure 6-6. The pH sensor consists of 2 circular gold electrodes (working and reference) that are coated in a pH sensitive thin film (either zinc oxide or iridium oxide) and connected to contact pads similar to those for contacting the impedance sensors.

A working electrode is placed directly by the impedance electrodes in the cellular culture chamber while the reference electrode is located halfway between the inlet and the culture chamber. Local changes in pH can be detected within the culture chamber due to the acidification of the medium by the tumor spheroid while the reference electrode remains in the unaffected medium. The reference electrode (diameter = 50 μm) is slightly larger than the working electrode (diameter = 40 μm) to increase the sensitivity of the response at the working electrode.

6.4.2 Fabrication

Gold conducting electrodes for micro-pH sensors were fabricated according to the standard lift-off procedure described in section 5.x.x. After gold electrodes were patterned subsequent steps were taken to pattern the pH sensing film. First, electrodes were passivated with a 15 micron thick layer of SU-8 photoresist. Next, zinc oxide electrodes were fabricated by sputtering a 100nm thick layer of zinc oxide directly onto electrode devices and patterned via wet etching. A protective layer of 3000PY photoresist was spun over and patterned to define the sensor area and a 1:900 solution of DI water and HCl was used to etch the unnecessary zinc oxide, revealing the sensor seen in figure 6-7.

6.4.3 Testing

Experiments were performed to evaluate the stability of the fabricated zinc oxide micro-pH electrodes. A PDMS microfluidic chamber was attached to the chip and buffer solution of 7 and 7.2 pH units pippetted onto the electrodes. The working and reference electrodes were contacted via spring loaded pogo pins and open circuit potentials were recorded for each buffer solutions via a Gamry Ref 600 Potentiostat. The setup is shown in figure 6-8.

6.5   Results and Discussion

6.5.1 Centimeter-scale Zinc Oxide pH Electrodes

1 x 3 cm bar pH electrodes were fabricated to test the pH sensitivity of 100nm sputtered zinc oxide thin films. Zinc oxide electrodes were first immersed in a buffer solution with a pH of 7.0 followed by buffer solutions of 4.0 and 10.0 pH units for 10 minutes in each solution. Figure 6-9 shows the response of one of these electrodes.

When immersed into the buffer solutions reach a stable potential after approximately 300 seconds and undergo varied drift depending on the pH of the solution. Zinc oxide is an amphoteric metal oxide that undergoes both acidic and basic reactions when immersed in solution [146]. The following redox cycling, as described by Willander and Al-Hilli, summarizes what occurs when ZnO is immersed in the pH buffer solution:

$$ZnO + 2H^+ + 2e^- \leftrightarrow Zn + H_2O$$
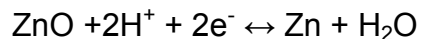
At a pH of 7.0, the calculated drift after 5 minutes is estimated to be 2.03 mV/min. It can be seen that the drift at pH values of 4.0 and 10.0 show a marked decrease in drift. This is likely due to a stabilization of the thin film achieved over longer incubation times. The longer incubation time in acidic solution may have caused loosely bound surface materials to dissolve resulting in a more stable thin film surface [149]. Plotting the stable potential recordings by the pH values gives the pH response of the sensor.

Figure 6-10 shows the pH response of the sputtered zinc oxide thin films is 26.971 mV/pH, which is well below the theoretical Nernst limit of 59.15 mV/pH [150]. It should be noted that dc sputtered zinc oxide films are primarily composed of highly crystalline ZnO films that exhibit a high anisotropy [151]. These structures are similar in morphology to the small, dense and highly clustered layers of zinc oxide nanorods grown by [149, 152]. Although, our pH sensitivity is much lower than the Nernstian response, it corresponds well with sensitivity values found by Fulati et al. for zinc oxide nanorod sensors fabricated via low temperature aqueous chemical growth.

6.5.2 Centimeter-scale Iridium Oxide pH Electrodes

pH electrodes were also constructed of iridium oxide to test their pH sensitivity as candidate films for monitoring extracellular pH of tumor spheroids. Open circuit

potentials were recorded for pH buffer solutions of 4, 7, and 10.   Iridium oxide bar electrodes were first immersed in 4.0 buffer solutions for ten minutes and allowed to stabilize. Electrodes were rinsed with DI water and dried then subsequently exposed to neutral and then acidic pH solutions immediately following baseline measurements in basic buffer. Measurements were repeated three times with three separate electrodes.

Figure 6-11 shows the pH response of iridium oxide electrode 1 immersed in acidic (4.0), neutral (7.0), and then basic (10.0) buffer solutions. It can be seen that the measured pH undergoes a large reduction in measured potential over the first 5 minutes of the acidic measurement and stabilizes at approximately 400mV with a drift of -5.17 mV/min after an additional 5 minutes. This drift reduces to -2.57 mV/min over the next 10 minutes.   When immersed into neutral pH buffer (7.0) the measured potential decreases to a value of 170 mV. This response can be attributed to the natural pH response of the electrode and is expected. However, the drift when exposed to neutral pH buffer solution is much smaller than the recorded drift in acidic buffer at .07 mV/min. Finally, when immersed in basic medium the potential reduces to -70mV and has a drift of .507 mV/min.

Figure 6-12 shows the average pH response of 3 pH electrodes immersed in acidic (4.0), neutral (7.0), and basic (10.0) pH buffer solutions along with plots of each individual electrode. The average measured potential at a pH of 4.0 is ~420 mV. The average pH sensitivity of all measured pH electrodes was -81.70 mV/pH.

6.5.3 Zinc Oxide Micro-pH Electrode Stability

Lastly, zinc oxide was deposited onto gold microelectrodes to form micro-pH electrodes on a microfluidic chip.   Due to damage to the micro dri-ref reference

electrode, pH sensitivity was not measured. However, the stability of the zinc oxide film was tested in pH buffer solutions of 7.0 and 7.2. A two-electrode cell was formed between the working and counter zinc oxide electrodes and the open circuit potential was measured 3 times for each solution in 2 minute intervals for a total of 6 minutes. Figure 6-13 shows the response of the electrode to each solution It is notable that for neutral (7.0) and nearly neutral (7.2) pH solutions the potential stabilizes after the first two minutes of exposure. For neutral pH buffer the -779 mV with a drift of ~4.5 mV/minute. For pH buffer at 7.2, the potential was measured to be -755 mV and a drift of ~3.5 mV/minute.

6.5.4 Conclusion

In comparison, electrodes fabricated from iridium oxide display a much higher pH response (81.70 mV/pH) than electrodes fabricated from zinc oxide thin films (~27.0 mV/pH) which displayed responses much lower than the theoretical Nernst limit of 59.15 mV/pH. Despite the low response of the zinc oxide thin films the values recorded were similar to those of previously developed nanorod sensors [ref 148,151]. Furthermore, sputtered zinc oxide thin films showed higher drift (1.07 mV/min) in the neutral buffer than the iridium oxide electrodes (.07 mV/min).

This lower drift around neutral pH will be essential when the electrodes are implemented in the micro-pH sensor. This is made more apparent when looking at stability tests of zinc oxide micro-pH electrodes. High drift values of 3.5 and 4.5 mV/minute are observed in buffer solutions of 7.2 and 7.0 pH values, respectively. In conclusion, iridium oxide electrodes are a suitable candidate for making micro-pH electrodes for monitoring the extracellular environment around tumor spheroids.
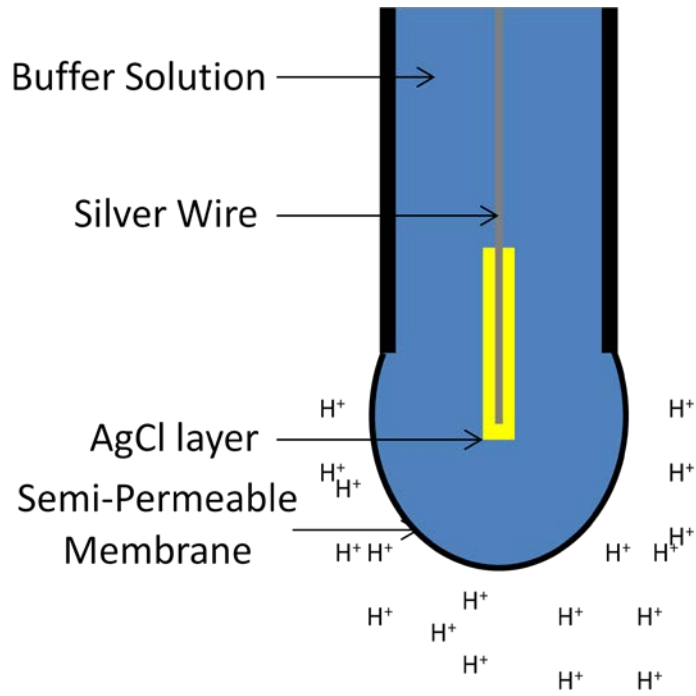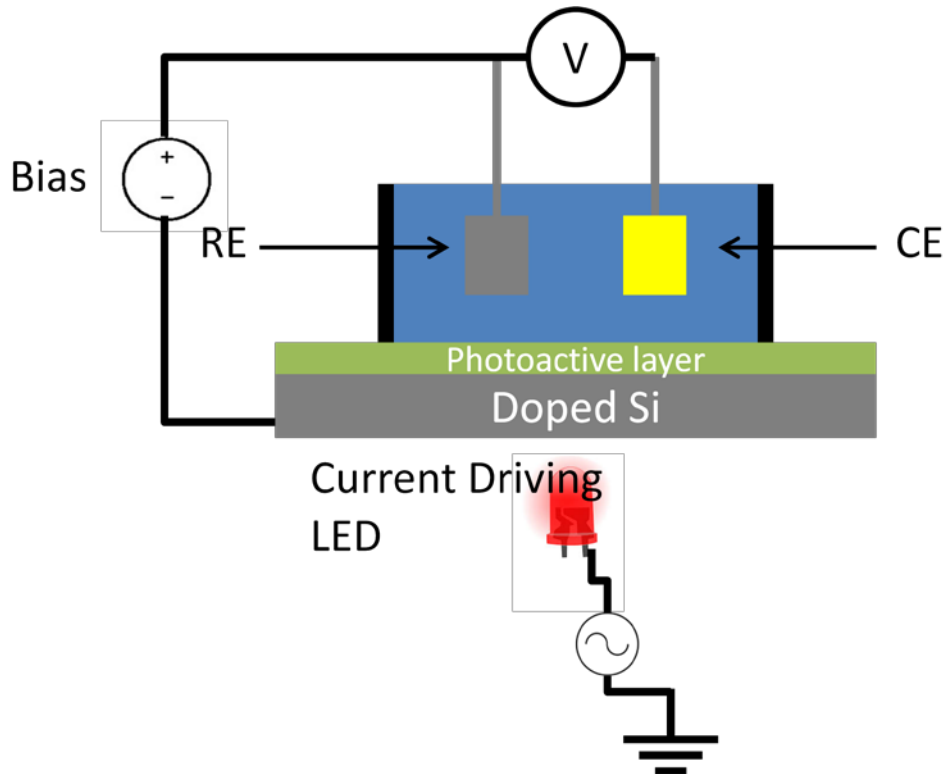
Figure 6-1 A simple pH electrode.
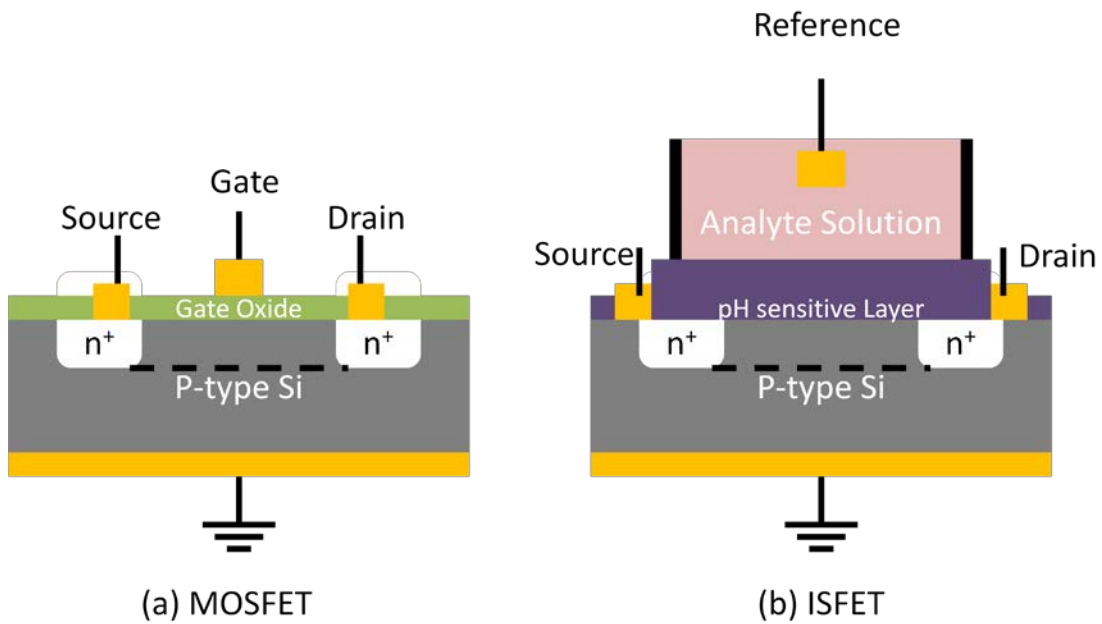

Figure 6-2 Example of a typical LAPS device.

Figure 6-3 Comparison of a (a) metallic-oxide-semiconductor FET (MOSFET) and (b) an ion-sensitivie FET (ISFET).
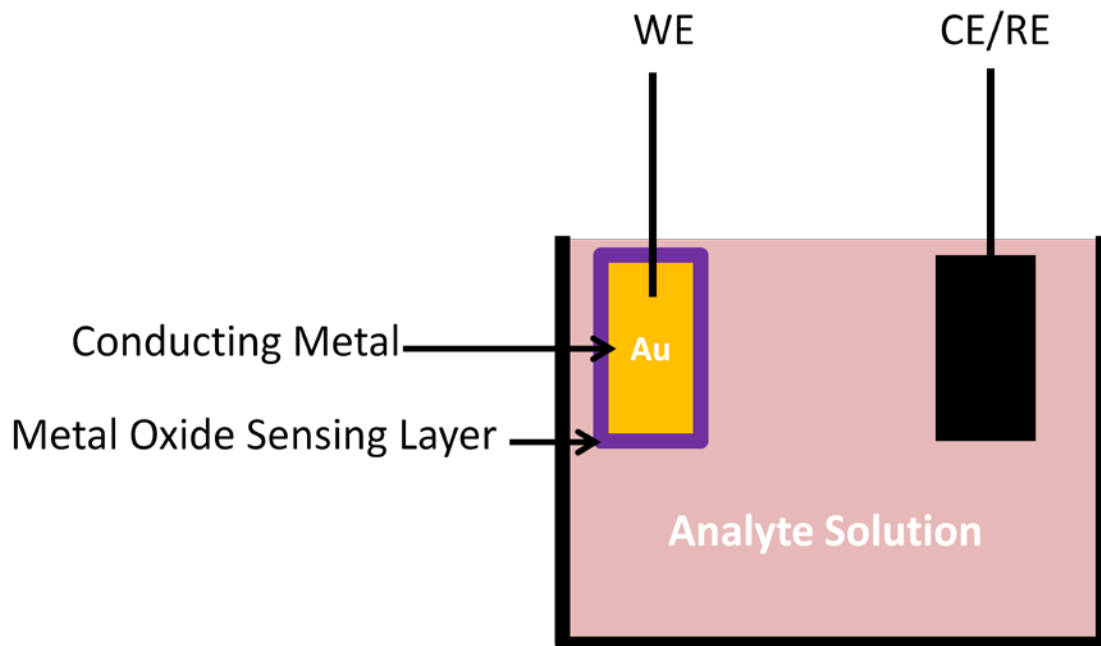

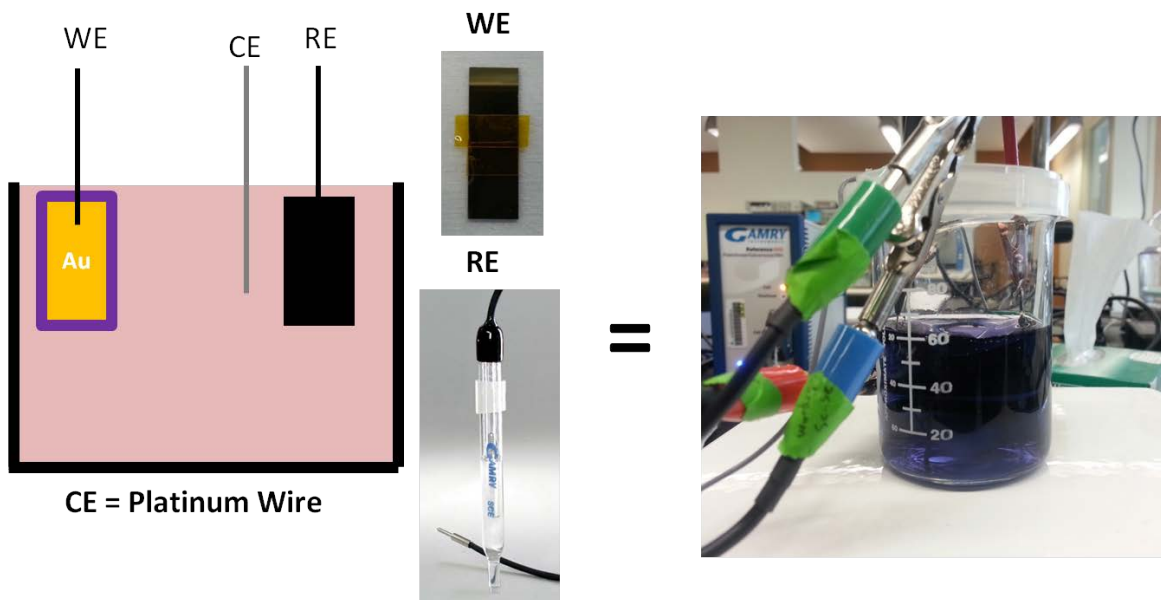Figure 6-4 Example of a thin film electrode sensor immersed in solution.

Figure 6-5 Experimental setup of 3-electrode cell for electrodeposition of iridium oxide.
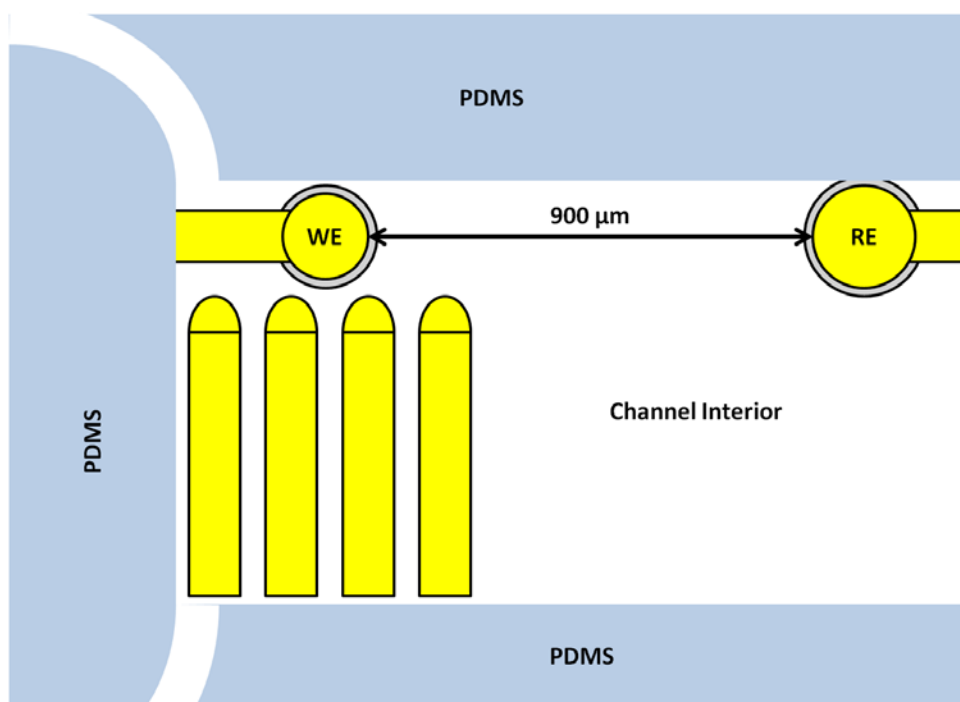

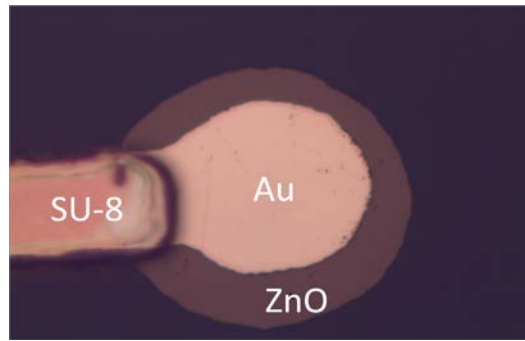Figure 6-6 Schematic view of electrode design for micro-pH electrodes.
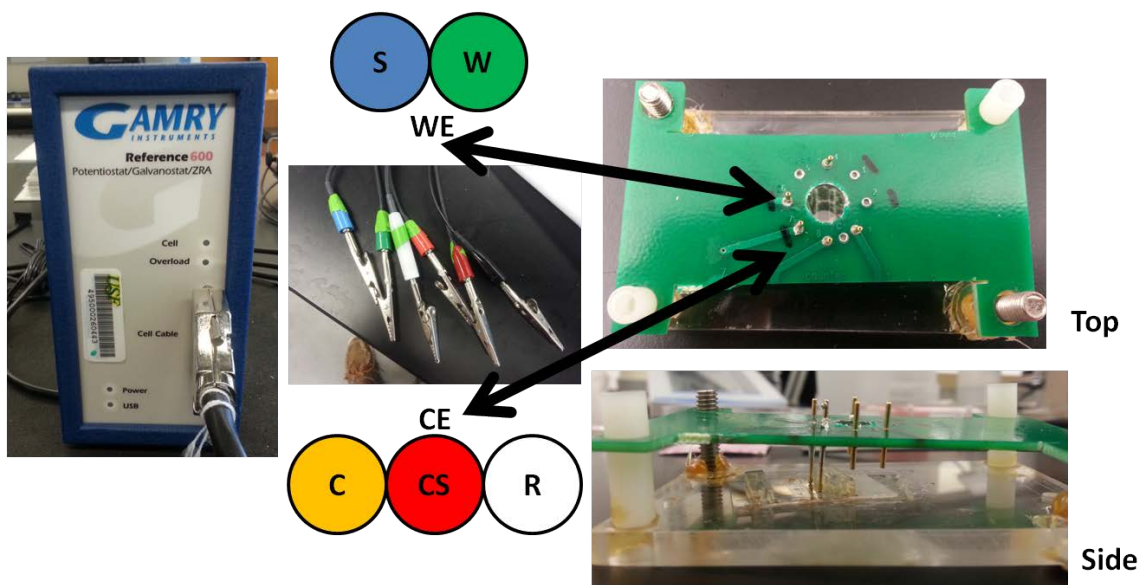
Figure 6-7 Etched zinc oxide micro-pH electrode.

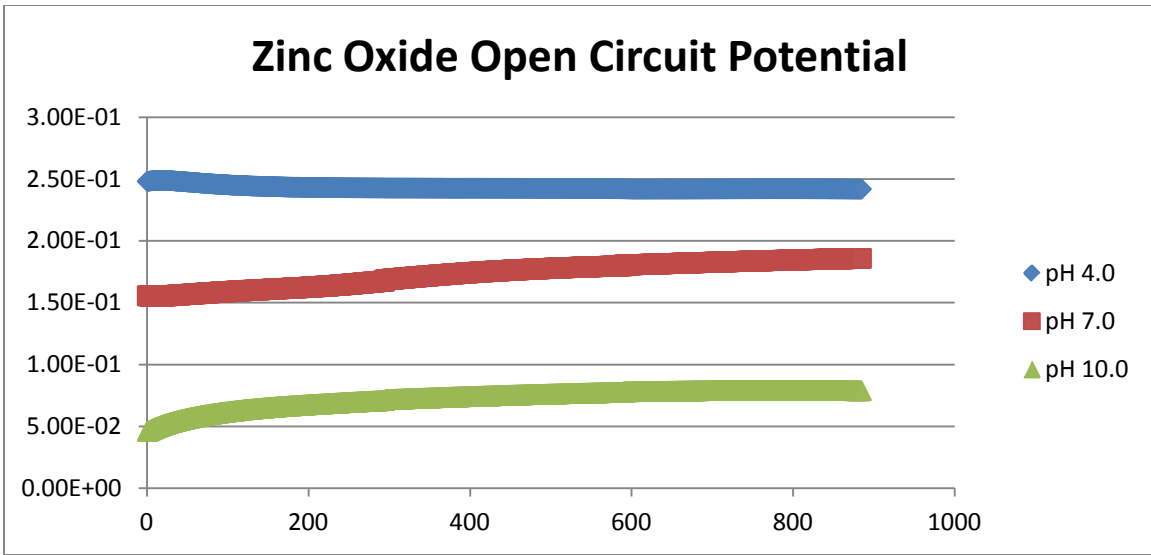Figure 6-8 Experimental setup for measuring micro-pH electrode response.

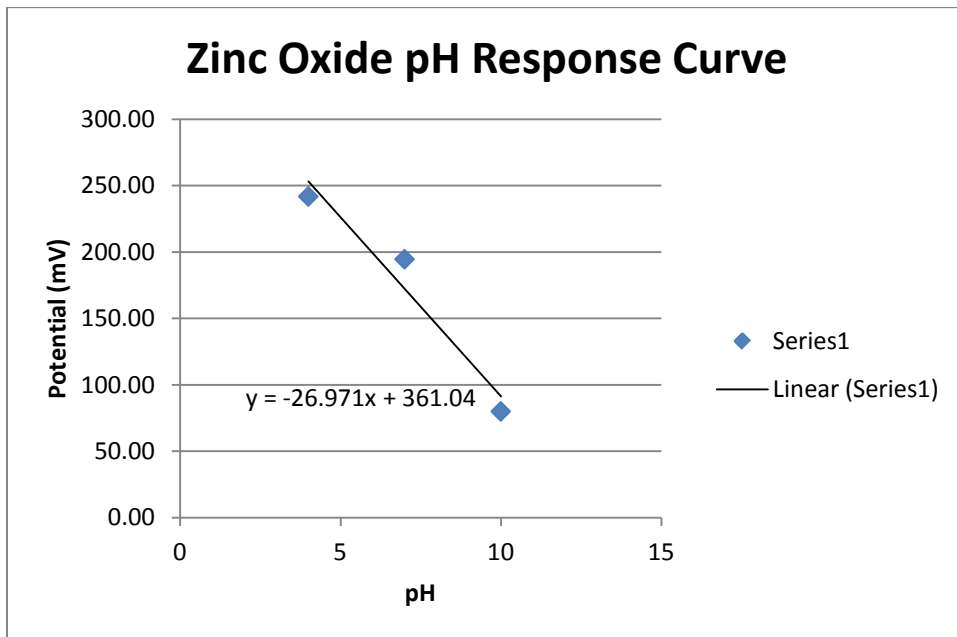Figure 6-9 Results of planar zinc oxide OCP measurements.

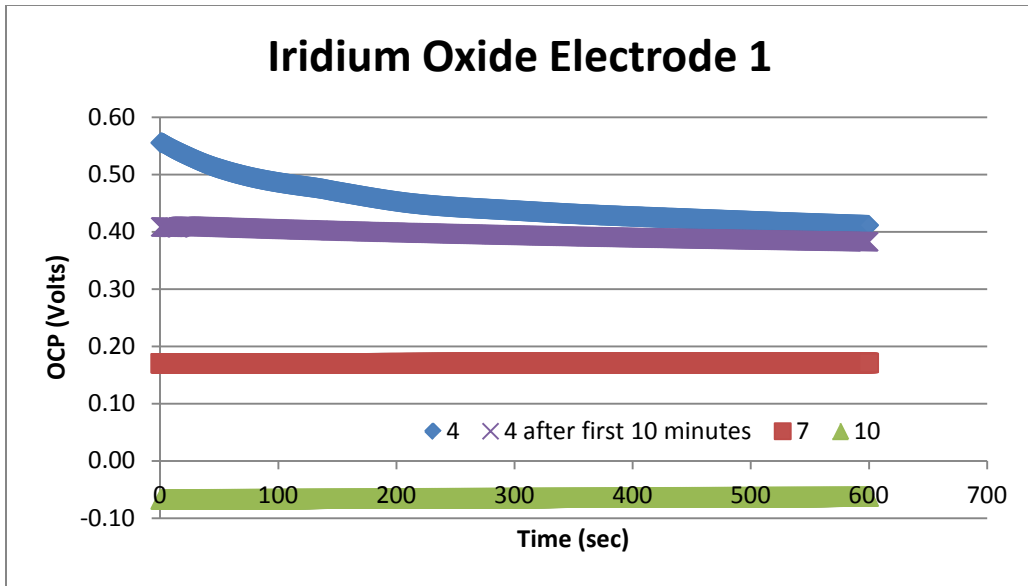Figure 6-10 pH response of planar zinc oxide pH electrodes.

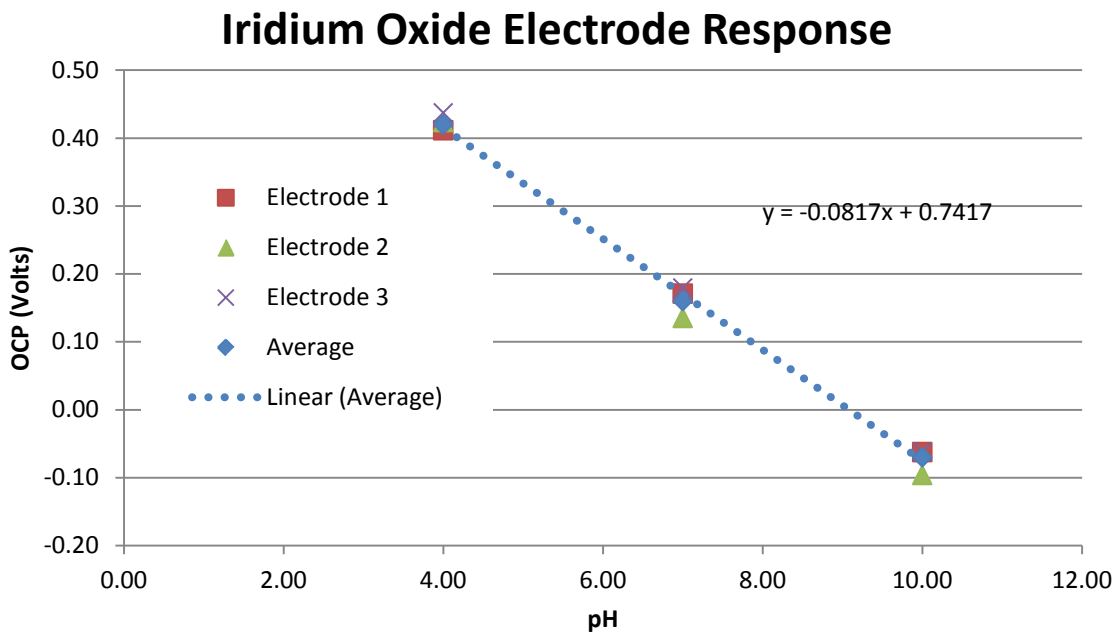Figure 6-11 Results of planar iridium oxide OCP measurements

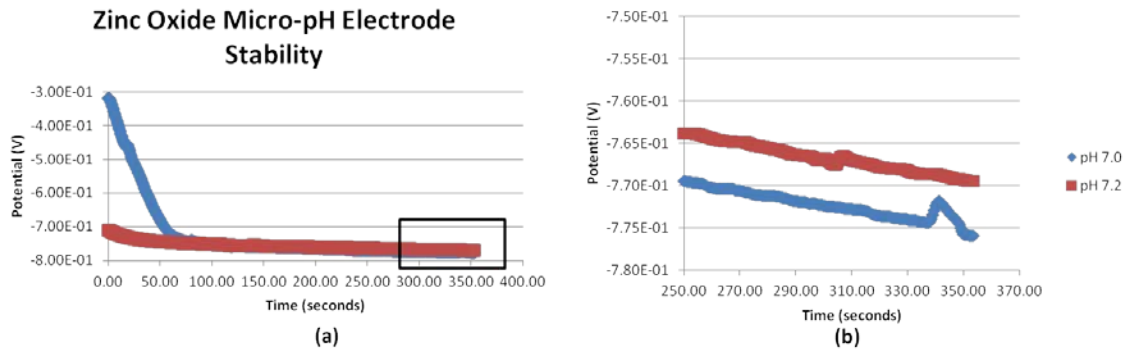Figure 6-12 pH response of planar iridium oxide electrodes.

106

Figure 6-13 Results of zinc oxide micro-pH electrode stability.

Chapter 7: Summary and Conclusion

7.1   Research Outcomes

This work has provided the basis for the development of a multiparametric microfluidic system for evaluating the response of tumor spheroids to nanoparticles and drug candidates in real-time. The full development of this system will provide a new tool for pharmaceutical companies to analyze the effects of new drug candidates in a fast and accurate manner.

The importance of increased spatial resolution was demonstrated by performing studies on the toxic interactions between silica nanowires and epithelial breast cancer cells. While not innately toxic, it was found that higher concentrations of SNW's can cause cell death through mechanical disturbances. The integration of a multi-electrode array established the mechanism of cell death by showing the pattern of cell death.

A microfluidic chip was designed to make impedance measurements of tumor spheroids with a maximum size of 350 microns. The functionality of this chip was demonstrated by measuring the change in impedance between KCl solution, DMEM, and Hs578T breast cancer spheroids. In addition, it was shown that the active area of the electrodes directly impact the magnitude of the impedance measured.   The presence of the tumor spheroid causes changes in the medium impedance at frequencies >30kHz, which corresponds to the beta region of the Schwan curve as expected.

Finally, preliminary work was done to design an online pH electrode capable of monitoring pH within the microfluidic channel. Proof of concept studies were performed to evaluate difference between pH changes of tumor cells in planar and 3D morphologies. In addition, metal oxide coatings were evaluated for pH sensitivity and calibrated at macro-scale. More work needs to be done to optimize and characterize pH electrode fabrication within the microfluidic chip.

7.2 Future Work

7.2.1 Real-time Analysis of Spheroidal Impedance

A second version of the switching circuit seen in Chapter 4 was designed in order to automate impedance monitoring of tumor spheroids (Figure 7-1). Preliminary testing has already been performed to verify functionality of the switching circuit (not reported). This new design will automate the impedance monitoring procedure while tumor spheroids are incubated and medium is continuously perfused over the cells.

This will allow extended time experiments capable of monitoring impedance as long as the structural integrity of the spheroid is maintained. Shear forces induced by medium flow may adversely affect the adherence of the cells to the spheroid. Future experiments will be performed to optimize the medium flow rate so that structural integrity is maintained for the duration of experiments. Future studies will investigate spheroidal response to known stimuli.

7.2.2 Spheroid Response to As$_2$O$_3$

In [153], impedance measurements verified in real-time that when exposed to arsenic trioxide, HEY ovarian cancer cell monolayers underwent apoptosis. As stated earlier, tumor cells grown in a spheroidal morphology have exhibited increased drug

resistance over cells cultured as monolayers. Experiments will be performed to evaluate changes (if any) in the dosage and/or time exposure required to induce apoptosis in HEY cell tumoroids. This work will serve two purposes. First, it will help establish a methodology for automated chemotherapy assays on tumor spheroids. Second, it will help provide information into the mechanisms behind drug resistance in 3D tumor models.

7.2.3 Optimization of Micro-pH Electrode and Automation

In chapter 6, a micro-pH electrode was designed and an attempt at fabrication was made. However, more work needs to be done to optimize the electro-deposition of the iridium oxide onto the metal conductor. In order to batch fabricate multiple pH electrodes a method must be established to deposit iridium oxide onto several electrodes simultaneously. In addition, the response of the micro-pH electrode must be characterized and compared to the macro fabricated iridium oxide electrodes. Finally, work must be done to automate and store the pH measurements so that pH can be recorded in concert with impedance measurements.

7.3   Future Applications for 3D Impedance Analysis

The primary advantage of using impedance-based systems to monitor 3D cellular models is the capability to detect morphological changes in a label-free, minimally invasive, manner in real-time. Table 3-2 highlighted advantages and disadvantages for using 3D spheroids in place of single cells and cellular monolayers. Single cells and traditional monolayer cultures are limited in physiological significance, resulting in models that are not capable of properly modeling the *in vivo* situation. By utilizing

impedance-based observation, a plethora of studies can be performed to further understand interactions on a multicellular level.

7.3.1 Fundamental Cellular Studies

Multi-electrode arrays are currently being used to monitor electrically active cells such as neurons [154-156]. Recording impedance changes of 3D neuronal spheroids can be used to expand fundamental knowledge of cell-cell and cell-matrix interactions [75, 84, 89]. Impedance measurements of monolayer cultures of neurological cells using planar electrode arrays differed from intact brain measurements, inferring that 2D cultures do not accurately mimic *in vivo* conditions. In addition to neuronal cellular spheroids, many other MCS have been developed for experimentation including hepatocyte spheroids for investigating liver function [157, 158], embryoid bodies for stem cell differentiation [159], and a variety of cancer cell models [2, 75, 84] .

An example where impedance-based assays can be used for fundamental studies of MCTS environmental interactions is in tumor cell invasion assays. Recently, Liu studied the potential for carcinoma-associated fibroblast (CAF) spheroids to promote invasive behavior of salivary gland adenoid cystic carcinoma (ACC-M) cellular spheroids while embedded in basement membrane [160]. Using a three chamber microfluidic device, it was found that when CAF were cultured adjacent to ACC-M, ACC-M cells invaded neighboring matrix and was reduced when MMP inhibitor was GM 6001 was introduced. Similar studies have proven EIS capable of monitoring growth rate of cells embedded inside of a 3D matrix [161]. Impedance based sensors integrated within culture chambers could actively sense changes in the density of cells trapped

within the matrix allowing for real-time cellular invasion assays, allowing for fully automated real-time monitoring of MCTS invasion.

7.3.2 High Throughput Drug Testing

Cancer drug development and drug discovery have been hampered by the poor predictability of current chemosensitivity and resistivity assays. Researchers are gradually recognizing the importance of new ex vivo assays encompassing both the tumor and its microenvironment. This recognition points towards using 3D culture systems due to their *in vivo* like behavior across many cell types. The primary barrier for use in high throughput assays is a lack of rapid and standardized assays specifically for 3D cultures. For this reason, real-time EIS monitoring of spheroidal cultures using microelectrodes provides a solid platform for high throughput drug testing. Standard microfabrication techniques provide a simple cost-effective way of fabricating large amounts of EIS monitoring systems small enough to integrate into the bottom of most standard multi-well plates. Similar assay systems have already been fabricated and are commercially available [162]. Massive parallel studies can be performed using EIS measurements to rapidly indicate the viability and response of MCTS to drug candidates.

Individual cell-based assays can be classified as: generic responses to stimulation, signal transduction monitoring, and transcription/translational responses. Recently reported impedance studies on MCS have assessed responses to generic chemical stimulation as well as transcription/translational responses. Signal transduction studies have yet to be reported using impedance-based methods. By correlating the impedance response of 3D tumor spheroids inoculated with potential

medicinal components with metabolic and environmental data taken from parallel sensors, physiologically relevant data can be recorded and used to assess the effects of a potential therapy. Significant challenges still exist in using these models reliably in the laboratory or clinical setting. In contrast with macro-scale laboratory approaches, microfluidic devices offer the potential for more controlled formation of 3D cell cultures and are also particularly suitable for high-throughput screening on small sample sizes, such as biopsies. Integrating microfluidic handling of cellular spheroids and implementing multiple parallel sensors for environmental and metabolic monitoring can revolutionize drug response predictability in pre-clinical settings, thereby accelerating drug development and enabling personalized treatment.

7.3.3 Stem Cell Differentiation

Available treatments for multiple traumatic and debilitating diseases including myochardial infarction, spinal cord injury, and brain trauma cannot reverse injuries sustained during trauma. Stem cell transplantation therapy from embryonic stem (ES), induced pluripotent (iPS) or adult stem cells (mesenchymal, hematopoietic or skeletal satellite myoblasts) offer a viable potential for new therapies that have little to no antigenic consequences. Unfortunately, teratoma formation (the development of a tumor resulting from the implantation of undifferentiated stem cells) as well as uncontrolled differentiation into other tissue types hampers efficient clinical usage of stem cells. For this reason resources and research have been dedicated to finding mechanisms to control differentiation of stem cells *in vitro*, prior to implantation *in vivo*.

For clinical applications, *in vitro* stem cell cultures should remain isolated without interaction with human or animal products to minimize contamination with pathogens.

Alternative synthetic serum and other chemicals have been developed for serum free expansion and proliferation of stem cell lines [163]. After expansion of a given stem cell line, in addition to these chemical constituents it is necessary to develop alternative methods for monitoring and stimulating various responses from stem cell populations. Bioreactors can be designed to utilize a multitude of methods to control stem cell fate and differentiation. Physical cues including electric fields [164-167] and mechanical forces [168-170] have been found have a major influence on cellular differentiation. Increasingly, these cues are being utilized to direct differentiation of stem cell lines. Due to the electrical capability to simultaneously monitor morphological changes (EIS) and stimulate cells (e.g. electroporation) EIS is well-suited as a method to monitor differentiation of EBs.

It has already been proven that differentiated osteogenic EBs have significantly higher impedances than necrotic and undifferentiated EBs [6]. Furthermore, mouse neural stem cells trapped in alginate beads and exposed to electrical gradients have significantly different neuron to astrocyte differentiation ratios than unstimulated cells. In addition, Yamada cultured R1 embryonic stem cells and stimulated them as both monolayers and embryoid bodies. It was found that cells stimulated as embryoid bodies increased differentiation into neuronal and muscle cell types [70]. Cells derived from stimulated EBs went on to incorporate into the central nervous system of recovered mouse embryos and successfully implanted into mice with injured spinal codes with a mortality rate of 1/5 with no immunoreactivity or tumorigenicity. Electrically stimulated cells differentiated faster and also remained pluripotent allowing them to differentiate further *in vivo* exploiting *in vivo* cellular conditioning for natural development. Devices

for stimulation of stem cell spheroids have been reported [154]. Using these concepts, bioreactors could direct differentiation patterns in EBs through dual-purpose bioelectrodes that stimulate and monitor cellular morphogenesis. This could foreseeably be used to mass produce cells with a defined lineage from pluripotent stem cells harvested from patients. Cells produced from this system could then be encapsulated into hydrogels [171, 172] for organ printing.

7.4   Conclusion

EIS has been utilized for assays of monolayer cultures including cytotoxicity, cell proliferation, and cellular kinetics/movement assays. Spheroid EIS systems have been used to monitor responses to chemotherapeutics, differentiation of osteogenic cells and Alzheimer's disease-like neurodegeneration of neuroblastoma spheroids. An inherent flaw in these systems is a lack of spatial resolution, inhibiting location specific analysis as well as investigation of drug penetration and diffusion. Furthermore, the mechanisms leading to cell death and morphology changes are difficult to discover based on impedance measurements alone. For this reason, it is necessary to develop electrodes capable of probing multiple areas of a single spheroid to increase spatial resolution and implement environmental pH, oxygen and CO_2 sensors to assign physiological significance to the measured impedances.
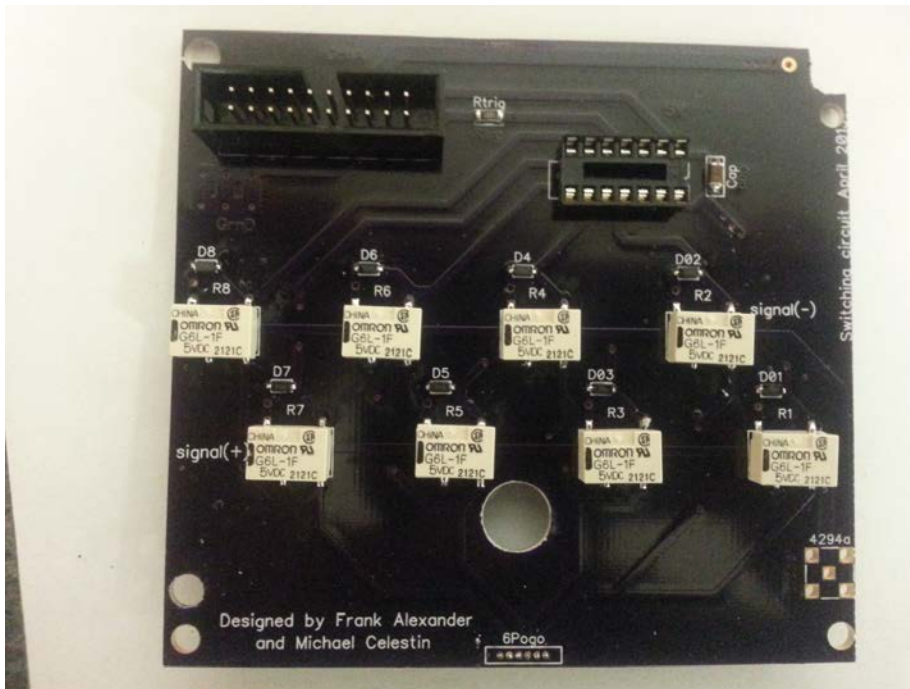
Figure 7-1 Completed switching circuit.

List of References

[1]   F. Hirschhaeuser, H. Menne, C. Dittfeld, J. West, W. Mueller-Klieser, and L. A. Kunz-Schughart, "Multicellular tumor spheroids: An underestimated tool is catching up again," *Journal of Biotechnology,* vol. 148, pp. 3-15, 2010.

[2]   F. Pampaloni, E. H. K. Stelzer, and A. Masotti, "Three-Dimensional Tissue Models for Drug Discovery and Toxicology," *Recent Patents on Biotechnology,* vol. 3, pp. 103-117, 2009.

[3]   K. Ueno, A. Miyashita, K. I. Endoh, T. Takezawa, M. Yamazaki, Y. Mori, and T. Satoh, "Formation of multicellular spheroids composed of rat hepatocytes," *Research communications in chemical pathology and pharmacology,* vol. 77, pp. 107-120, 1992.

[4]   P. Bartholomä, Impidjati, A. Reininger-Mack, Z. Zhang, H. Thielecke, and A. Robitzki, "A More Aggressive Breast Cancer Spheroid Model Coupled to an Electronic Capillary Sensor System for a High-Content Screening of Cytotoxic Agents in Cancer Therapy: 3-Dimensional In Vitro Tumor Spheroids as a Screening Model," *Journal of Biomolecular Screening,* vol. 10, pp. 705-714, October 1, 2005.

[5]   Q. Liu, J. Yu, L. Xiao, J. C. O. Tang, Y. Zhang, P. Wang, and M. Yang, "Impedance studies of bio-behavior and chemosensitivity of cancer cells by micro-electrode arrays," *Biosensors and Bioelectronics,* vol. 24, pp. 1305-1310, 2009.

[6]   C. Hildebrandt, H. Büth, S. Cho, Impidjati, and H. Thielecke, "Detection of the osteogenic differentiation of mesenchymal stem cells in 2D and 3D cultures by electrochemical impedance spectroscopy," *Journal of Biotechnology,* vol. 148, pp. 83-90, 2010.

[7]   D. Seidel, D. Krinke, H.-G. Jahnke, A. Hirche, D. Kloß, T. G. A. Mack, F. Striggow, and A. Robitzki, "Induced Tauopathy in a Novel 3D-Culture Model Mediates Neurodegenerative Processes: A Real-Time Study on Biochips," *PLoS ONE,* vol. 7, p. e49150, 2012.

[8]   R. Tonkens, "An overview of the drug development process," *Physician Exec,* vol. 31, pp. 48-52, May-Jun 2005.

117

[9]   H. Yu and A. Adedoyin, "ADME/Tox in drug discovery: integration of experimental and computational technologies," *Drug Discovery Today,* vol. 8, pp. 852-861, 2003.

[10]   L. A. Kunz-Schughart, J. P. Freyer, F. Hofstaedter, and R. Ebner, "The Use of 3-D Cultures for High-Throughput Screening: The Multicellular Spheroid Model," *Journal of Biomolecular Screening,* vol. 9, pp. 273-285, June 1, 2004.

[11]   K. Lin, S. Maeda, and T. Saito, "Long-term maintenance of liver-specific functions in three-dimensional culture of adult rat hepatocytes with a porous gelatin sponge support," *Biotechnology and Applied Biochemistry,* vol. 21, pp. 19-27, 1995.

[12]   K. Dunker, C. Brown, D. Lawson, L. Iakoucheva, and Z. Obradović, "Intrinsic Disorder and Protein Function," *Biochemistry,* vol. 41, pp. 6573-6582, 2002.

[13]   U. Resch-Genger, M. Grabolle, S. Cavaliere-Jaricot, R. Nitschke, and T. Nann, "Quantum dots versus organic dyes as fluorescent labels," *Nat Meth,* vol. 5, pp. 763-775, 2008.

[14]   J. S. Daniels and N. Pourmand, "Label-Free Impedance Biosensors: Opportunities and Challenges," *Electroanalysis,* vol. 19, pp. 1239-1257, 2007.

[15]   M. A. Cooper and V. T. Singleton, "A survey of the 2001 to 2005 quartz crystal microbalance biosensor literature: applications of acoustic physics to the analysis of biomolecular interactions," *Journal of Molecular Recognition,* vol. 20, pp. 154-184, 2007.

[16]   M. Yue, J. C. Stachowiak, H. Lin, R. Datar, R. Cote, and A. Majumdar, "Label-Free Protein Recognition Two-Dimensional Array Using Nanomechanical Sensors," *Nano Letters,* vol. 8, pp. 520-524, 2012/03/23 2008.

[17]   K. S. Hwang, S. M. Lee, S. K. Kim, J. H. Lee, and T. S. Kim, "Micro- and nanocantilever devices and systems for biomolecule detection," *Annual review of analytical chemistry (Palo Alto, Calif.),* vol. 2, pp. 77-98, 2009.

[18]   A. Star, E. Tu, J. Niemann, J.-C. P. Gabriel, C. S. Joiner, and C. Valcke, "Label-free detection of DNA hybridization using carbon nanotube network field-effect transistors," *Proceedings of the National Academy of Sciences of the United States of America,* vol. 103, pp. 921-926, January 24 2006.

[19]   E. Stern, J. F. Klemic, D. A. Routenberg, P. N. Wyrembak, D. B. Turner-Evans, A. D. Hamilton, D. A. LaVan, T. M. Fahmy, and M. A. Reed, "Label-free immunodetection with CMOS-compatible semiconducting nanowires," *Nature,* vol. 445, pp. 519-522, 2007.

[20] M. Tondra, M. Granger, R. Fuerst, M. Porter, C. Nordman, J. Taylor, and S. Akou, "Design of integrated microfluidic device for sorting magnetic beads in biological assays," *Magnetics, IEEE Transactions on,* vol. 37, pp. 2621-2623, 2001.

[21] R. Halai and M. A. Cooper, "Using label-free screening technology to improve efficiency in drug discovery," *Expert Opinion on Drug Discovery,* vol. 7, pp. 123-131, 2012/08/31 2012.

[22] P. Banerjee and A. K. Bhunia, "Mammalian cell-based biosensors for pathogens and toxins," *Trends in Biotechnology,* vol. 27, pp. 179-188, 2009.

[23] K. A. Marx, T. Zhou, A. Montrone, D. McIntosh, and S. J. Braunhut, "Quartz crystal microbalance biosensor study of endothelial cells and their extracellular matrix following cell removal: Evidence for transient cellular stress and viscoelastic changes during detachment and the elastic behavior of the pure matrix," *Analytical Biochemistry,* vol. 343, pp. 23-34, 2005.

[24] B. Xi, N. Yu, X. Wang, X. Xu, and Y. Abassi, "The application of cell-based label-free technology in drug discovery," *Biotechnology Journal,* vol. 3, pp. 484-495, 2008.

[25] A. R. A. Rahman, S. Bhat, and S. Bhansali, "Design, Fabrication, and Impedance Characterization of a Capacitance-Based Salinity Sensor for Marine Applications," *Journal of The Electrochemical Society,* vol. 155, pp. J355-J360, 2008.

[26] H. E. Endres, S. Drost, and F. Hutter, "Impedance spectroscopy on dielectric gas sensors," *Sensors and Actuators B: Chemical,* vol. 22, pp. 7-11, 1994.

[27] A. Han, L. Yang, and A. B. Frazier, "Quantification of the Heterogeneity in Breast Cancer Cell Lines Using Whole-Cell Impedance Spectroscopy," *Clinical Cancer Research,* vol. 13, pp. 139-143, January 1 2007.

[28] B.-Y. Chang and S.-M. Park, "Electrochemical Impedance Spectroscopy," *Annual Review of Analytical Chemistry,* vol. 3, pp. 207-229, 2010.

[29] D. D. Macdonald, "Reflections on the history of electrochemical impedance spectroscopy," *Electrochimica Acta,* vol. 51, pp. 1376-1388, 2006.

[30] A. A. Sagues and A. M. Zayed, "Low-Frequency Electrochemical Impedance for Measuring Corrosion of Epoxy-Coated Reinforcing Steel in Concrete," *Corrosion,* vol. 47, pp. 852-859, 2012/08/24 1991.

[31] V. Horvat-Radosevic and K. Kvastek, "Three-electrode cell set-up electrical equivalent circuit applied to impedance analysis of thin polyaniline film modified electrodes," *Journal of Electroanalytical Chemistry,* vol. 631, pp. 10-21, 2009.

[32] J.-G. Guan, Y.-Q. Miao, and Q.-J. Zhang, "Impedimetric biosensors," *Journal of Bioscience and Bioengineering,* vol. 97, pp. 219-226, 2004.

[33] C.-M. Lo, C. R. Keese, and I. Giaever, "Monitoring Motion of Confluent Cells in Tissue Culture," *Experimental Cell Research,* vol. 204, pp. 102-109, 1993.

[34] A. R. Rahman, J. Register, G. Vuppala, and S. Bhansali, "Cell culture monitoring by impedance mapping using a multielectrode scanning impedance spectroscopy system (CellMap)," *Physiological Measurement,* vol. 29, pp. S227-39, 2008.

[35] J. R. Macdonald and W. B. Johnson, "Fundamentals of Impedance Spectroscopy," in *Impedance Spectroscopy*, ed: John Wiley & Sons, Inc., 2005, pp. 1-26.

[36] C. M. Kurz, H. Büth, A. Sossalla, V. Vermeersch, V. Toncheva, P. Dubruel, E. Schacht, and H. Thielecke, "Chip-based impedance measurement on single cells for monitoring sub-toxic effects on cell membranes," *Biosensors and Bioelectronics,* vol. 26, pp. 3405-3412, 2011.

[37] E. Engel, V. Barcilon, and R. S. Eisenberg, "The Interpretation of Current-Voltage Relations Recorded from a Spherical Cell with a Single Microelectrode," *Biophysical Journal,* vol. 12, pp. 384-403, 1972.

[38] S. Gawad, T. Sun, N. G. Green, and H. Morgan, *Impedance spectroscopy using maximum length sequences: Application to single cell analysis* vol. 78: AIP, 2007.

[39] J. Gimsa, T. Müller, T. Schnelle, and G. Fuhr, "Dielectric spectroscopy of single human erythrocytes at physiological ionic strength: dispersion of the cytoplasm," *Biophysical Journal,* vol. 71, pp. 495-506, 1996.

[40] A. Han and A. B. Frazier, "Ion channel characterization using single cell impedance spectroscopy," *Lab on a Chip,* vol. 6, pp. 1412-1414, 2006.

[41] Y. Huang, N. S. Sekhon, J. Borninski, N. Chen, and B. Rubinsky, "Instantaneous, quantitative single-cell viability assessment by electrical evaluation of cell membrane integrity with microfabricated devices," *Sensors and Actuators A: Physical,* vol. 105, pp. 31-39, 2003.

[42] M. Hywel and et al., "Single cell dielectric spectroscopy," *Journal of Physics D: Applied Physics,* vol. 40, p. 61, 2007.

[43] C. M. Kurz, A. Maurer, K. Thees, S. Schillberg, T. Velten, and H. Thielecke, "Impedance-controlled cell entrapment using microhole-array chips allows the isolation and identification of single, highly productive cells," *Sensors and Actuators B: Chemical,* vol. 158, pp. 345-352, 2011.

[44] A. R. Wheeler, W. R. Throndset, R. J. Whelan, A. M. Leach, R. N. Zare, Y. H. Liao, K. Farrell, I. D. Manger, and A. Daridon, "Microfluidic Device for Single-Cell Analysis," *Analytical Chemistry,* vol. 75, pp. 3581-3586, 2003.

[45] K. Asami, "Characterization of biological cells by dielectric spectroscopy," *Journal of Non-Crystalline Solids,* vol. 305, pp. 268-277, 2002.

[46] S. Arndt, J. Seebach, K. Psathaki, H.-J. Galla, and J. Wegener, "Bioelectrical impedance assay to monitor changes in cell shape during apoptosis," *Biosensors and Bioelectronics,* vol. 19, pp. 583-594, 2004.

[47] R. Bragós, E. Sarró, A. Fontova, A. Soley, J. Cairó, A. Bayés-Genís, and J. Rosell, "Four Versus Two-Electrode Measurement Strategies for Cell Growing and Differentiation Monitoring Using Electrical Impedance Spectroscopy," presented at the 28th IEEE EMBS Annual International Conference, New York, 2006.

[48] I. Giaever and C. R. Keese, "Micromotion of Mammalian Cells Measured Electrically," *Proceedings of the National Academy of Sciences of the USA,* vol. 88, pp. 7896-7900, 1991.

[49] D. T. Price, A. R. Rahman, and S. Bhansali, "Design rule for optimization of microelectrodes used in electric cell-substrate impedance sensing (ECIS)," *Biosensors & bioelectronics,* vol. 24, pp. 2071-6, 2009.

[50] A. R. Rahman, C. M. Lo, and S. Bhansali, "A detailed model for high-frequency impedance characterization of ovarian cancer epithelial cell layer using ECIS electrodes," *IEEE transactions on bio-medical engineering,* vol. 56, pp. 485-92, 2009.

[51] S. Haas, H.-G. Jahnke, M. Glass, R. Azendorf, S. Schmidt, and A. A. Robitzki, "Real-time monitoring of relaxation and contractility of smooth muscle cells on a novel biohybrid chip," *Lab on a Chip,* vol. 10, 2010.

[52] C. R. Keese, K. Bhawe, J. Wegener, and I. Giaever, "Real-Time Impedance Assay to Follow the Invasive Activities of Metastatic Cells in Culture " *BioTechniques,* vol. 33, pp. 842-850, 2002.

[53] C. R. Keese and I. Giaever, "A biosensor that monitors cell morphology with electrical fields," *Engineering in Medicine and Biology Magazine, IEEE,* vol. 13, pp. 402-408, 1994.

[54]   J. H. T. Luong, M. Habibi-Rezaei, J. Meghrous, C. Xiao, K. B. Male, and A. Kamen, "Monitoring Motility, Spreading, and Mortality of Adherent Insect Cells Using an Impedance Sensor," *Analytical Chemistry,* vol. 73, pp. 1844-1848, 2001.

[55]   H. E. Park, D. Kim, H. S. Koh, S. Cho, J.-S. Sung, and J. Y. Kim, "Real-Time Monitoring of Neural Differentiation of Human Mesenchymal Stem Cells by Electric Cell-Substrate Impedance Sensing," *Journal of Biomedicine and Biotechnology,* vol. 2011, 2011.

[56]   H. R. Siddiquei, A. N. Nordin, M. I. Ibrahimy, M. A. Arifin, N. H. Sulong, M. Mel, and I. Voiculescu, "Electrical cell-substrate impedance sensing (ECIS) based biosensor for characterization of DF-1 cells," in *Computer and Communication Engineering (ICCCE), 2010 International Conference on*, 2010, pp. 1-4.

[57]   X. Cheng, Y.-s. Liu, D. Irimia, U. Demirci, L. Yang, L. Zamir, W. R. Rodriguez, M. Toner, and R. Bashir, "Cell detection and counting through cell lysate impedance spectroscopy in microfluidic devices," *Lab on a Chip,* vol. 7, pp. 746-755, 2007.

[58]   D. Kloß, M. Fischer, A. Rothermel, J. C. Simon, and A. A. Robitzki, "Drug testing on 3D in vitro tissues trapped on a microcavity chip," *Lab Chip,* vol. 8, pp. 879-884, 2008.

[59]   D. Kloß, R. Kurz, H.-G. Jahnke, M. Fischer, A. Rothermel, U. Anderegg, J. C. Simon, and A. A. Robitzki, "Microcavity array (MCA)-based biosensor chip for functional drug screening of 3D tissue models," *Biosensors and Bioelectronics,* vol. 23, pp. 1473-1480, 2008.

[60]   A. Robitzki, H. Thielecke, and A. Reininger-Mack, "Development of a novel microcapillary array: Characterization of in vitro 3D tissue models by bioimpedance spectroscopy," 2002.

[61]   H. Thielecke, A. Mack, and A. Robitzki, "Biohybrid microarrays – Impedimetric biosensors with 3D in vitro tissues for toxicological and biomedical screening," *Fresenius' Journal of Analytical Chemistry,* vol. 369, pp. 23-29, 2001.

[62]   P. Paterlini-Brechot and N. L. Benali, "Circulating tumor cells (CTC) detection: Clinical impact and future directions," *Cancer Letters,* vol. 253, pp. 180-204, 2007.

[63]   D. Holmes, D. Pettigrew, C. H. Reccius, J. D. Gwyer, C. van Berkel, J. Holloway, D. E. Davies, and H. Morgan, "Leukocyte analysis and differentiation using high speed microfluidic single cell impedance cytometry," *Lab on a Chip,* vol. 9, pp. 2881-2889, 2009.

[64] T. Sun and H. Morgan, "Single-cell microfluidic impedance cytometry: a review," *Microfluidics and Nanofluidics,* vol. 8, pp. 423-443, 2010.

[65] S. Tao, G. Shady, B. Catia, G. G. Nicolas, and M. Hywel, "Broadband single cell impedance spectroscopy using maximum length sequences: theoretical analysis and practical considerations," *Measurement Science and Technology,* vol. 18, p. 2859, 2007.

[66] T. Sun, C. van Berkel, N. Green, and H. Morgan, "Digital signal processing methods for impedance microfluidic cytometry," *Microfluidics and Nanofluidics,* vol. 6, pp. 179-187, 2009.

[67] M. W. Jackson and T. P. Gordon, "A novel impedance-based cellular assay for the detection of anti-calcium channel autoantibodies in type 1 diabetes," *Journal of Immunological Methods,* vol. 361, pp. 31-36, 2010.

[68] J. Wegener, M. Sieber, and H.-J. Galla, "Impedance analysis of epithelial and endothelial cell monolayers cultured on gold surfaces," *Journal of Biochemical and Biophysical Methods,* vol. 32, pp. 151-170, 1996.

[69] J. Carlsson and T. Nederman, "Tumour spheroid technology in cancer therapy research," *European journal of cancer & clinical oncology,* vol. 25, pp. 1127-33, 1989.

[70] K. M. Yamada and E. Cukierman, "Modeling Tissue Morphogenesis and Cancer in 3D," *Cell,* vol. 130, pp. 601-610, 2007.

[71] L. G. Griffith and M. A. Swartz, "Capturing complex 3D tissue physiology in vitro," *Nat Rev Mol Cell Biol,* vol. 7, pp. 211-224, 2006.

[72] R. Glicklis, J. C. Merchuk, and S. Cohen, "Modeling mass transfer in hepatocyte spheroids via cell viability, spheroid size, and hepatocellular functions," *Biotechnology and Bioengineering,* vol. 86, pp. 672-680, 2004.

[73] A. J. Franko and R. M. Sutherland, "Oxygen Diffusion Distance and Development of Necrosis in Multicell Spheroids," *Radiation Research,* vol. 79, pp. 439-453, 2012/03/18 1979.

[74] D. S. Cowan, K. O. Hicks, and W. R. Wilson, "Multicellular membranes as an in vitro model for extravascular diffusion in tumours," *The British journal of cancer. Supplement,* vol. 27, pp. S28-31, 1996.

[75] N. T. Elliott and F. Yuan, "A review of three-dimensional in vitro tissue models for drug discovery and transport studies," *Journal of Pharmaceutical Sciences,* vol. 100, pp. 59-74, 2011.

[76] E. Huey, S. K. Arya, S. Krishnan, D. K. Sood, A. Dey, E. Murphy-Perez, and S. Bhansali, "Study of Growth Kinetics of Pd Metal Catalyzed Silica Nanowires for Biosensor Applications," *Procedia Engineering,* vol. 25, pp. 1577-1580, 2011.

[77] F. Alexander Jr, E. Huey, D. T. Price, and S. Bhansali, "Quantitative impedance analysis of nanowires and cancer cells," *Procedia Engineering,* vol. 5, pp. 842-845, 2010.

[78] E. Huey, S. Krishnan, S. K. Arya, A. Dey, and S. Bhansali, "Optimized growth and integration of silica nanowires into interdigitated microelectrode structures for biosensing," *Sensors and Actuators B: Chemical,* 2012.

[79] B. Dubertret, P. Skourides, D. J. Norris, V. Noireaux, A. H. Brivanlou, and A. Libchaber, "In Vivo Imaging of Quantum Dots Encapsulated in Phospholipid Micelles," *Science,* vol. 298, pp. 1759-1762, November 29, 2002.

[80] X. Michalet, F. F. Pinaud, L. A. Bentolila, J. M. Tsay, S. Doose, J. J. Li, G. Sundaresan, A. M. Wu, S. S. Gambhir, and S. Weiss, "Quantum Dots for Live Cells, in Vivo Imaging, and Diagnostics," *Science,* vol. 307, pp. 538-544, January 28, 2005.

[81] W. Mueller-Klieser, "Multicellular spheroids," *Journal of Cancer Research and Clinical Oncology,* vol. 113, pp. 101-122, 1987.

[82] J. Friedrich, R. Ebner, and L. A. Kunz-Schughart, "Experimental anti-tumor therapy in 3-D: Spheroids -old hat or new challenge?," *International Journal of Radiation Biology,* vol. 83, pp. 849-871, 2007.

[83] R.-Z. Lin, L.-F. Chou, C.-C. Chien, and H.-Y. Chang, "Dynamic analysis of hepatoma spheroid formation: roles of E-cadherin and β1-integrin," *Cell and Tissue Research,* vol. 324, pp. 411-422, 2006.

[84] R.-Z. Lin and H.-Y. Chang, "Recent advances in three-dimensional multicellular spheroid culture for biomedical research," *Biotechnology Journal,* vol. 3, pp. 1172-1184, 2008.

[85] A. R. Kimmel and B. Oliver, *DNA Microarrays, Part B: Databases and Statistics*: Elsevier Science, 2006.

[86] T. G. Hammond and J. M. Hammond, "Optimized suspension culture: the rotating-wall vessel," *American Journal of Physiology - Renal Physiology,* vol. 281, pp. F12-F25, July 1, 2001.

[87] M. Ingram, G. Techy, R. Saroufeem, O. Yazan, K. Narayan, T. Goodwin, and G. Spaulding, "Three-dimensional growth patterns of various human tumor cell lines in simulated microgravity of a NASA bioreactor," *In Vitro Cellular & Developmental Biology - Animal,* vol. 33, pp. 459-466, 1997.

[88] E. S. Tzanakakis, L. K. Hansen, and W.-S. Hu, "The role of actin filaments and microtubules in hepatocyte spheroid self-assembly," *Cell Motility and the Cytoskeleton,* vol. 48, pp. 175-189, 2001.

[89] L. E. O'Brien, M. M. P. Zegers, and K. E. Mostov, "Building epithelial architecture: insights from three-dimensional culture models," *Nat Rev Mol Cell Biol,* vol. 3, pp. 531-537, 2002.

[90] A. Sebastian, A.-M. Buckle, and G. H. Markx, "Tissue engineering with electric fields: Immobilization of mammalian cells in multilayer aggregates using dielectrophoresis," *Biotechnology and Bioengineering,* vol. 98, pp. 694-700, 2007.

[91] M. D. Ungrin, C. Joshi, A. Nica, C. I. Bauwens, and P. W. Zandstra, "Reproducible, Ultra High-Throughput Formation of Multicellular Organization from Single Cell Suspension-Derived Human Embryonic Stem Cell Aggregates," *PLoS ONE,* vol. 3, p. e1565, 2008.

[92] M.-H. Wu, "Simple poly(dimethylsiloxane) surface modification to control cell adhesion," *Surface and Interface Analysis,* vol. 41, pp. 11-16, 2009.

[93] J. Friedrich, C. Seidel, R. Ebner, and L. A. Kunz-Schughart, "Spheroid-based drug screen: considerations and practical approach," *Nat. Protocols,* vol. 4, pp. 309-324, 2009.

[94] M. Lund-Johansen, R. Bjerkvig, P. A. Humphrey, S. H. Bigner, D. D. Bigner, and O.-D. Laerum, "Effect of Epidermal Growth Factor on Glioma Cell Growth, Migration, and Invasion in Vitro," *Cancer Research,* vol. 50, pp. 6039-6044, September 15, 1990 1990.

[95] C. Lorenzo, C. Frongia, R. Jorand, J. Fehrenbach, P. Weiss, A. Maandhui, G. Gay, B. Ducommun, and V. Lobjois, "Live cell division dynamics monitoring in 3D large spheroid tumor models using light sheet microscopy," *Cell Div,* vol. 6, p. 22, 2011.

[96] A. Schuessele, W. Eder, L. A. Kunz-Schughart, T. Blunk, J. Tessmar, and A. Goepferich, "Drug delivery to the bone-implant interface: Functional hydroxyapatite surfaces and particles Chapter 7: Confocal microscopy for monitoring uptake and distribution of nanoparticles in a three-dimensional cell culture model," Doctorate, Chemistry and Pharmacy, University of Regensburg, Bavaria, Germany, 2006.

[97]   L. O. Sillerud, J. P. Freyer, M. Neeman, and M. A. Mattingly, "Proton NMR microscopy of multicellular tumor spheroid morphology," *Magn Reson Med,* vol. 16, pp. 380-9, Dec 1990.

[98]   K. Kruttwig, C. Brueggemann, E. Kaijzel, S. Vorhagen, T. Hilger, C. Lowik, and M. Hoehn, "Development of a three-dimensional in vitro model for longitudinal observation of cell behavior: monitoring by magnetic resonance imaging and optical imaging," *Mol Imaging Biol,* vol. 12, pp. 367-76, Aug 2010.

[99]   J. Alvarez-Perez, P. Ballesteros, and S. Cerdan, "Microscopic images of intraspheroidal pH by 1H magnetic resonance chemical shift imaging of pH sensitive indicators," *MAGMA,* vol. 18, pp. 293-301, Dec 2005.

[100] K. Hattermann, J. Held-Feindt, and R. Mentlein, "Spheroid confrontation assay: a simple method to monitor the three-dimensional migration of different cell types in vitro," *Ann Anat,* vol. 193, pp. 181-4, May 2011.

[101] J. Friedrich, C. Seidel, R. Ebner, and L. A. Kunz-Schughart, "Spheroid-based drug screen: considerations and practical approach," *Nat Protoc,* vol. 4, pp. 309-24, 2009.

[102] G. Cheng, J. Tse, R. K. Jain, and L. L. Munn, "Micro-Environmental Mechanical Stress Controls Tumor Spheroid Size and Morphology by Suppressing Proliferation and Inducing Apoptosis in Cancer Cells," *PLoS ONE,* vol. 4, p. e4632, 2009.

[103] S. Khoshyomn, P. L. Penar, W. J. McBride, and D. J. Taatjes, "Four-dimensional analysis of human brain tumor spheroid invasion into fetal rat brain aggregates using confocal scanning laser microscopy," *Journal of Neuro-Oncology,* vol. 38, pp. 1-10, 1998.

[104] D. F. Williams, "On the mechanisms of biocompatibility," *Biomaterials,* vol. 29, pp. 2941-2953, 2008.

[105] W.-T. Liu, "Nanoparticles and their biological and environmental applications," *Journal of Bioscience and Bioengineering,* vol. 102, pp. 1-7, 2006.

[106] N. S. Ramgir, A. Zajac, P. K. Sekhar, L. Lee, T. A. Zhukov, and S. Bhansali, "Voltammetric Detection of Cancer Biomarkers Exemplified by Interleukin-10 and Osteopontin with Silica Nanowires," *The Journal of Physical Chemistry C,* vol. 111, pp. 13981-13987, 2007/09/01 2007.

[107] P. K. Sekhar, N. S. Ramgir, and S. Bhansali, "Metal-Decorated Silica Nanowires: An Active Surface-Enhanced Raman Substrate for Cancer Biomarker Detection," *The Journal of Physical Chemistry C,* vol. 112, pp. 1729-1734, 2008/02/01 2008.

[108] J. M. McIntyre and H. Q. Pham, "Electrochemical impedance spectroscopy; a tool for organic coatings optimizations," *Progress in Organic Coatings,* vol. 27, pp. 201-207, 1994.

[109] I. Mora-Sero, F. Fabregat-Santiago, B. Denier, J. Bisquert, R. Tena-Zaera, J. Elias, and C. Levy-Clement, "Determination of carrier density of ZnO nanowires by electrochemical techniques," *Applied Physics Letters,* vol. 89, p. 203117, 2006.

[110] R. S. Wagner and W. C. Ellis, Vapor-Liquid-Solid Mechanism of Single Crystal Growth vol. 4: *AIP*, 1964.

[111] Y. Wu and P. Yang, "Direct Observation of Vapor-Liquid-Solid Nanowire Growth," *Journal of American Chemical Society,* vol. 123, p. 2, 2001.

[112] H. Schwan, "Electrical properties of tissue and cell suspensions," *Advances in biological and medical physics,* vol. 5, pp. 147-209, 1957.

[113] H. P. Schwan, "Electrical Characteristics of Tissues," *Biophysik,* vol. 1, pp. 198-208, 1963.

[114] S. Qi, C. Yi, W. Chen, C.-C. Fong, S.-T. Lee, and M. Yang, "Effects of Silicon Nanowires on HepG2 Cell Adhesion and Spreading," *ChemBioChem,* vol. 8, pp. 1115-1118, 2007.

[115] D. C. Julien, C. C. Richardson, M. F. Beaux Ii, D. N. McIlroy, and R. A. Hill, "In vitro proliferating cell models to study cytotoxicity of silica nanowires," *Nanomedicine: Nanotechnology, Biology and Medicine,* vol. 6, pp. 84-92, 2009.

[116] T. Nair, J. T. Symanowski, and H. M. Gach, "Comparison of complex permittivities of isotonic colloids containing single-wall carbon nanotubes of varying chirality," *Bioelectromagnetics,* vol. 33, pp. 134-146, 2012.

[117] K. Puneet, L. Kevin, A. S. Joel, and B. Shekhar, "Sharpening of hollow silicon microneedles to reduce skin penetration force," *Journal of Micromechanics and Microengineering,* vol. 20, p. 045011, 2010.

[118] P. Khanna, "Optimization and characterization of lab-on-a-chip elements: Microfluidic chambers and microneedles," Ph.D. Dissertation, Electrical Engineering, University of South Florida, 2009.

[119] P. Sigmund, "Theory of Sputtering. I. Sputtering Yield of Amorphous and Polycrystalline Targets," *Physical Review,* vol. 184, pp. 383-416, 1969.

[120] D. T. Price, "Optimization of Bio-Impedance Sensor for Enhanced Detection and Characterization of Adherent Cells," Ph.D., Electrical Engineering, University of South Florida, 2012.

[121] S. E. Moulton, J. N. Barisci, A. Bath, R. Stella, and G. G. Wallace, "Studies of double layer capacitance and electron transfer at a gold electrode exposed to protein solutions," *Electrochimica Acta,* vol. 49, pp. 4223-4230, 2004.

[122] J. Newman, "Resistance for Flow of Current to a Disk," *Journal of The Electrochemical Society,* vol. 113, pp. 501-502, May 1, 1966 1966.

[123] J. C. Owicki and J. Wallace Parce, "Biosensors based on the energy metabolism of living cells: the physical chemistry and cell biology of extracellular acidification," *Biosensors and Bioelectronics,* vol. 7, pp. 255-272, 1992.

[124] D. Hafeman, J. Parce, and H. McConnell, "Light-addressable potentiometric sensor for biochemical systems," *Science,* vol. 240, pp. 1182-1185, May 27, 1988.

[125] P. Duroux, C. Emde, P. Bauerfeind, C. Francis, A. Grisel, L. Thybaud, D. Arstrong, C. Depeursinge, and A. L. Blum, "The ion sensitive field effect transistor (ISFET) pH electrode: a new sensor for long term ambulatory pH monitoring," *Gut,* vol. 32, pp. 240-245, March 1, 1991.

[126] W. H. Baumann, M. Lehmann, A. Schwinde, R. Ehret, M. Brischwein, and B. Wolf, "Microelectronic sensor system for microphysiological application on living cells," *Sensors and Actuators B: Chemical,* vol. 55, pp. 77-89, 1999.

[127] M. Brischwein, E. R. Motrescu, E. Cabala, A. M. Otto, H. Grothe, and B. Wolf, "Functional cellular assays with multiparametric silicon sensor chips," *Lab Chip,* vol. 3, pp. 234-40, Nov 2003.

[128] B. Wolf, M. Brischwein, W. Baumann, R. Ehret, and M. Kraus, "Monitoring of cellular signalling and metabolism with modular sensor-technique: The PhysioControl-Microsystem (PCM®)," *Biosensors and Bioelectronics,* vol. 13, pp. 501-509, 1998.

[129] T. Schwarzenberger, P. Wolf, M. Brischwein, R. Kleinhans, F. Demmel, A. Lechner, B. Becker, and B. Wolf, "Impedance sensor technology for cell-based assays in the framework of a high-content screening system," *Physiol Meas,* vol. 32, pp. 977-93, Jul 2011.

[130] R. Kleinhans, M. Brischwein, P. Wang, B. Becker, F. Demmel, T. Schwarzenberger, M. Zottmann, P. Wolf, A. Niendorf, and B. Wolf, "Sensor-based cell and tissue screening for personalized cancer chemotherapy," *Med Biol Eng Comput,* vol. 50, pp. 117-26, Feb 2012.

[131] L. T. Inc. (2013). *pH and CO2 Levels*. Available: http://www.lifetechnologies.com/us/en/home/references/gibco-cell-culture-basics/cell-culture-environment/ph-co2-levels.html

[132] J. C. Owicki, L. J. Bousse, D. G. Hafeman, G. L. Kirk, J. D. Olson, H. G. Wada, and J. W. Parce, "The light-addressable potentiometric sensor: principles and biological applications," *Annual review of biophysics and biomolecular structure,* vol. 23, pp. 87-114, 1994.

[133] Y. Ito, K. Morimoto, and Y. Tsunoda, "Light-addressable potentiometric (LAP) gas sensor," *Sensors and Actuators B: Chemical,* vol. 13, pp. 348-350, 1993.

[134] A. Seki, S.-i. Ikeda, I. Kubo, and I. Karube, "Biosensors based on light-addressable potentiometric sensors for urea, penicillin and glucose," *Analytica chimica acta,* vol. 373, pp. 9-13, 1998.

[135] P. Bergveld, "Development of an Ion-Sensitive Solid-State Device for Neurophysiological Measurements," *Biomedical Engineering, IEEE Transactions on,* vol. BME-17, pp. 70-71, 1970.

[136] J.-L. Chiang, J.-C. Chou, and Y.-C. Chen, "Study of the pH-ISFET and EnFET for Biosensor Application," *Journal of Medical and Biological Engineering,* vol. 21, pp. 135-146, 2001.

[137] K. G. Kreider, M. J. Tarlov, and J. P. Cline, "Sputtered thin-film pH electrodes of platinum, palladium, ruthenium, and iridium oxides," *Sensors and Actuators B: Chemical,* vol. 28, pp. 167-172, 1995.

[138] R. A. Yotter and D. M. Wilson, "Sensor technologies for monitoring metabolic activity in single cells-part II: nonoptical methods and applications," *Sensors Journal, IEEE,* vol. 4, pp. 412-429, 2004.

[139] S. Głab, A. Hulanicki, G. Edwall, and F. Ingman, "Metal-metal oxide and metal oxide electrodes as pH sensors," *Critical Reviews in Analytical Chemistry,* vol. 21, pp. 29-47, 1989.

[140] U. Guth, F. Gerlach, M. Decker, W. Oelßner, and W. Vonau, "Solid-state reference electrodes for potentiometric sensors," *Journal of Solid State Electrochemistry,* vol. 13, pp. 27-39, 2009.

[141] I. A. Ges, B. L. Ivanov, D. K. Schaffer, E. A. Lima, A. A. Werdich, and F. J. Baudenbacher, "Thin-film IrOx pH microelectrode for microfluidic-based microsystems," *Biosensors and Bioelectronics,* vol. 21, pp. 248-256, 2005.

[142] S. Yao, M. Wang, and M. Madou, "A pH Electrode Based on Melt-Oxidized Iridium Oxide," *Journal of The Electrochemical Society,* vol. 148, pp. H29-H36, April 1, 2001.

[143] H. A. Elsen, C. F. Monson, and M. Majda, "Effects of electrodeposition conditions and protocol on the properties of iridium oxide pH sensor electrodes," *Journal of The Electrochemical Society,* vol. 156, pp. F1-F6, 2009.

[144] W.-D. Huang, L.-C. Hsu, J. Wang, T. Ativanichayaphong, S. Deb, M. Chiao, and J. C. Chiao, "Investigation of repeatability of sol-gel iridium oxide pH sensor on flexible substrate," 2008, pp. 726916-726916-9.

[145] S. M. Al-Hilli, M. Willander, A. Ost, and P. Stralfors, "ZnO nanorods as an intracellular sensor for pH measurements," *Journal of Applied Physics,* vol. 102, p. 084304, 2007.

[146] M. Willander and S. Al-Hilli, "ZnO nanorods as an intracellular sensor for pH measurements," *Methods Mol Biol,* vol. 544, pp. 187-200, 2009.

[147] P. D. Batista and M. Mulato, "ZnO extended-gate field-effect transistors as pH sensors," *Applied Physics Letters,* vol. 87, p. 143508, 2005.

[148] K. Yamanaka, "Anodically Electrodeposited Iridium Oxide Films(AEIROF) from Alkaline Solutions for Electrochromic Display Devices," *Japanese journal of applied physics,* vol. 28, pp. 632-637, 1989.

[149] A. Fulati, S. M. Usman Ali, M. Riaz, G. Amin, O. Nur, and M. Willander, "Miniaturized pH sensors based on zinc oxide nanotubes/nanorods," *Sensors,* vol. 9, pp. 8911-8923, 2009.

[150] M. Willander and S. Al-Hilli, "ZnO Nanorods as an Intracellular Sensor for pH Measurements," in *Micro and Nano Technologies in Bioanalysis*, ed: Springer, 2009, pp. 187-200.

[151] M. Sabino, D. Oliveira, V. Falcao, A. Bernardes-Silva, and J. Branco, "Structural analysis of ZnO thin films obtained by dc sputtering and electron beam evaporation," *Powder Diffraction,* vol. 23, pp. S91-S93, 2008.

[152] Q. Li, V. Kumar, Y. Li, H. Zhang, T. J. Marks, and R. P. Chang, "Fabrication of ZnO nanorods and nanotubes in aqueous solutions," *Chemistry of Materials,* vol. 17, pp. 1001-1006, 2005.

[153] F. A. Alexander, M. Celestin, D. T. Price, M. Nanjundan, and S. Bhansali, "Design and validation of a multi-electrode bioimpedance system for enhancing spatial resolution of cellular impedance studies," *Analyst,* 2013.

[154] Y. Takayama, H. Moriguchi, A. Saito, K. Kotani, and Y. Jimbo, "Ensemble stimulation of embryoid bodies using microfabricated ITO substrates," in *Engineering in Medicine and Biology Society, 2009. EMBC 2009. Annual International Conference of the IEEE*, 2009, pp. 5993-5996.

[155] K. Musick, D. Khatami, and B. C. Wheeler, "Three-dimensional micro-electrode array for recording dissociated neuronal cultures," *Lab on a Chip,* vol. 9, pp. 2036-2042, 2009.

[156] T. Valero, G. Moschopoulou, S. Kintzios, P. Hauptmann, M. Naumann, and T. Jacobs, "Studies on neuronal differentiation and signalling processes with a novel impedimetric biosensor," *Biosensors and Bioelectronics,* vol. 26, pp. 1407-1413, 2010.

[157] J. Z. Tong, P. De Lagausie, V. Furlan, T. Cresteil, O. Bernard, and F. Alvarez, "Long-term culture of adult rat hepatocyte spheroids," *Experimental Cell Research,* vol. 200, pp. 326-332, 1992.

[158] R. Glicklis, L. Shapiro, R. Agbaria, J. C. Merchuk, and S. Cohen, "Hepatocyte behavior within three-dimensional porous alginate scaffolds," *Biotechnology and Bioengineering,* vol. 67, pp. 344-353, 2000.

[159] G. R. Martin and M. J. Evans, "Differentiation of clonal lines of teratocarcinoma cells: formation of embryoid bodies in vitro," *Proceedings of the National Academy of Sciences,* vol. 72, pp. 1441-1445, April 1, 1975.

[160] T. Liu, B. Lin, and J. Qin, "Carcinoma-associated fibroblasts promoted tumor spheroid invasion on a microfluidic 3D co-culture device," *Lab on a Chip,* vol. 10, pp. 1671-1677, 2010.

[161] S.-P. Lin, T. R. Kyriakides, and J.-J. J. Chen, "On-line observation of cell growth in a three-dimensional matrix on surface-modified microelectrode arrays," *Biomaterials,* vol. 30, pp. 3110-3117, 2009.

[162] N. Ke, X. Wang, X. Xu, and Y. A. Abassi, "The xCELLigence system for real-time and label-free monitoring of cell viability," *Methods Mol Biol,* vol. 740, pp. 33-43, 2011.

[163] B. C. Heng, H. K. Haider, E. K.-W. Sim, T. Cao, and S. C. Ng, "Strategies for directing the differentiation of stem cells into the cardiomyogenic lineage in vitro," *Cardiovascular Research,* vol. 62, pp. 34-42, April 1, 2004.

[164] M. A. Matos and M. T. Cicerone, "Alternating current electric field effects on neural stem cell viability and differentiation," *Biotechnology Progress,* vol. 26, pp. 664-670, 2010.

[165] H. Sauer, G. Rahimi, J. Hescheler, and M. Wartenberg, "Effects of electrical fields on cardiomyocyte differentiation of embryonic stem cells," *Journal of Cellular Biochemistry,* vol. 75, pp. 710-723, 1999.

[166] E. Serena, E. Figallo, N. Tandon, C. Cannizzaro, S. Gerecht, N. Elvassore, and G. Vunjak-Novakovic, "Electrical stimulation of human embryonic stem cells: Cardiac differentiation and the generation of reactive oxygen species," *Experimental Cell Research,* vol. 315, pp. 3611-3619, 2009.

[167] M. Yamada, K. Tanemura, S. Okada, A. Iwanami, M. Nakamura, H. Mizuno, M. Ozawa, R. Ohyama-Goto, N. Kitamura, M. Kawano, K. Tan-Takeuchi, C. Ohtsuka, A. Miyawaki, A. Takashima, M. Ogawa, Y. Toyama, H. Okano, and T. Kondo, "Electrical Stimulation Modulates Fate Determination of Differentiating Embryonic Stem Cells," *STEM CELLS,* vol. 25, pp. 562-570, 2007.

[168] G. Altman, R. Horan, I. Martin, J. Farhadi, P. Stark, V. Volloch, G. Vunjak-Novakovic, J. Richmond, and D. L. Kaplan, "Cell differentiation by mechanical stress," *The FASEB Journal,* vol. 16, pp. 270-272, February 1, 2002.

[169] C. Y. C. Huang, K. L. Hagar, L. E. Frost, Y. Sun, and H. S. Cheung, "Effects of Cyclic Compressive Loading on Chondrogenesis of Rabbit Bone-Marrow Derived Mesenchymal Stem Cells," *STEM CELLS,* vol. 22, pp. 313-323, 2004.

[170] H. L. Lim, J. C. Chuang, T. Tran, A. Aung, G. Arya, and S. Varghese, "Dynamic Electromechanical Hydrogel Matrices for Stem Cell Culture," *Advanced Functional Materials,* vol. 21, pp. 55-63, 2010.

[171] F. Xu, C.-a. M. Wu, V. Rengarajan, T. D. Finley, H. O. Keles, Y. Sung, B. Li, U. A. Gurkan, and U. Demirci, "Three-Dimensional Magnetic Assembly of Microscale Hydrogels," *Advanced Materials,* vol. 23, pp. 4254-4260, 2011.

[172] U. A. Gurkan, S. Tasoglu, D. Kavaz, M. C. Demirel, and U. Demirci, "Emerging Technologies for Assembly of Microscale Hydrogels," *Advanced Healthcare Materials,* vol. 1, pp. 149-158, 2012.

[173] © 2011 IEEE. Reprinted, with permission, from F. A. Alexander, D. T. Price, and S. Bhansali, "From cellular cultures to cellular spheroids: is impedance spectroscopy a viable tool for monitoring multicellular spheroid (MCS) drug models?," *Biomedical Engineering, IEEE Reviews in,* vol. 6, pp. 63-76, 2013.

[174] F. A. Alexander, M. Celestin, D. T. Price, M. Nanjundan, and S. Bhansali, "Design and validation of a multi-electrode bioimpedance system for enhancing spatial resolution of cellular impedance studies," *Analyst*, 2013.

Appendices

Appendix A: Copyright Permissions for Chapters 2 and 3

Appendix B: Copyright Permission for Chapter 4

Real-time impedance analysis of silica nanowire toxicity on epithelial breast cancer cells

If you are not the author of this article and you wish to reproduce material from it in a third party non-RSC publication you must formally request permission using RightsLink. Go to our Instructions for using RightsLink page for details.

Authors contributing to RSC publications (journal articles, books or book chapters) do not need to formally request permission to reproduce material contained in this article provided that the correct acknowledgement is given with the reproduced material.

Reproduced material should be attributed as follows:

- For reproduction of material from NJC:
  Reproduced from Ref. XX with permission from the Centre National de la Recherche Scientifique (CNRS) and The Royal Society of Chemistry.
- For reproduction of material from PCCP:
  Reproduced from Ref. XX with permission from the PCCP Owner Societies.
- For reproduction of material from PPS:
  Reproduced from Ref. XX with permission from the European Society for Photobiology, the European Photochemistry Association, and The Royal Society of Chemistry.
- For reproduction of material from all other RSC journals and books:
  Reproduced from Ref. XX with permission from The Royal Society of Chemistry.

If the material has been adapted instead of reproduced from the original RSC publication "Reproduced from" can be substituted with "Adapted from".

In all cases the Ref. XX is the XXth reference in the list of references.

If you are the author of this article you do not need to formally request permission to reproduce figures, diagrams etc. contained in this article in third party publications or in a thesis or dissertation provided that the correct acknowledgement is given with the reproduced material.

Reproduced material should be attributed as follows:

- For reproduction of material from NJC:
  [Original citation] - Reproduced by permission of The Royal Society of Chemistry (RSC) on behalf of the Centre National de la Recherche Scientifique (CNRS) and the RSC
- For reproduction of material from PCCP:
  [Original citation] - Reproduced by permission of the PCCP Owner Societies

- For reproduction of material from PPS:
  [Original citation] - Reproduced by permission of The Royal Society of Chemistry (RSC) on behalf of the European Society for Photobiology, the European Photochemistry Association, and RSC
- For reproduction of material from all other RSC journals:
  [Original citation] - Reproduced by permission of The Royal Society of Chemistry

If you are the author of this article you still need to obtain permission to reproduce the whole article in a third party publication with the exception of reproduction of the whole article in a thesis or dissertation.

Information about reproducing material from RSC articles with different licences is available on our Permission Requests page.

136

About the Author

Frank Alexander Jr. earned his B.S. in Electrical Engineering (Cum Laude) from Southern University and A&M College in Baton Rouge, LA in 2009 and his M. S. degree in Electrical Engineering from the University of South Florida in 2011. Frank is a recipient of the NSF Graduate Research Fellowship, NSF Bridge to the Doctorate Fellowship, GEM Fellowship, and NSF IREE Award. He has recently completed his doctoral degree in Electrical Engineering at the University of South Florida as the final graduate of the BioMEMS and Microsystems Group at USF.